

RM-308

PHOTOMETRIC MEASUREMENTS OF  
SIMULATED LUNAR SURFACES

January 1966

FACILITY FORM 802

N66-20989  
(ACCESSION NUMBER) (THRU)

104 1  
(PAGES) (CODE)

065263 06  
(NASA CR OR TMX OR AD NUMBER) (CATEGORY)

GPO PRICE \$ \_\_\_\_\_

CFSTI PRICE(S) \$ \_\_\_\_\_

Hard copy (HC) 4.00

Microfiche (MF) .75

ff 853 July 65

*Grumman*

**RESEARCH DEPARTMENT**

**GRUMMAN AIRCRAFT ENGINEERING CORPORATION**  
**BETHPAGE NEW YORK**

Grumman Research Department Memorandum RM-308

PHOTOMETRIC MEASUREMENTS OF SIMULATED  
LUNAR SURFACES

by

J.D. Halajian

and

F.A. Spagnolo

Geo-Astrophysics Section

January 1966

Quarterly Progress Report on NASA Contract No. NAS 9-3182

Approved by: *Charles E. Mack, Jr.*

Charles E. Mack, Jr.  
Director of Research

### ACKNOWLEDGMENTS

The authors are indebted to H. B. Hallock of Servo Engineering and his assistants J. Grusauskas, D. R. Lamberty, and D. Schlaijker for operating the photometric analyzer, building the "bead" models and making the measurements. We extend acknowledgment to Dr. G. McCoyd and J. Reichman for their helpful comments and general review of the contents of Phase III. We are also very grateful to K. Brand of the Computing Research Section for his invaluable aid in programming the analysis included in Phase III and the Appendix.

## SUMMARY

This report is in partial fulfillment of the reporting requirements on Contract No. NAS 9-3182. It is the second quarterly progress report on the extension of the work on "Photometric Measurements of Simulated Lunar Surfaces" and covers the work performed in the period from October 1, 1965 to December 31, 1965.

In Phase I, albedo and photometric measurements of all natural specimens at specified viewing angles and wavelengths were completed. Spectral responses of our photometric system and the sun-sensor systems used in lunar observations are discussed. A preliminary comparison of test results with available lunar data reveals certain similarities in albedo vs. color behavior, and in the "opposition" region of the brightness-phase angle curve. Unlike the moon, however, the test specimens, with the exception of the sea coral, do not exhibit clear evidence of reddening at large phase angles.

In Phase II, the photometric properties of "suspended particles" were measured at various particle spacing to diameter ratios. The results are preliminary but, as we predicted, they are in poor agreement with the lunar data.

In Phase III, a computer program designed to determine the closest photometric match of the lunar surface with four contrived geometries under a wide range of boundary conditions was completed. Results confirm previous qualitative analyses and promise to pave the way to a high precision fit with the lunar data and, possibly, to a quantitative estimate of the porosity of the uppermost optical layer of the lunar surface.

TABLE OF CONTENTS

<u>Item</u>	<u>Page</u>
Introduction .....	1
Work Accomplished .....	2
Phase I - Spectral Photometry	
Purpose .....	4
Spectral Response Studies .....	4
Discussion of Test Results .....	6
Phase II - Photometry of Suspended Particles	
Purpose .....	10
Analysis .....	10
Experimental Models .....	10
Discussion of Test Results .....	11
Phase III - Geometry of Backscattering Surfaces	
Purpose .....	13
Analytical Models .....	13
Discussion of Analytical Results .....	15
Conclusions and Recommendations .....	18
References .....	20
Appendix .....	21

## LIST OF ILLUSTRATIONS

<u>Figure</u>		<u>Page</u>
1	Spectral Response at Integrated Visible (V) Light .....	21
2	Spectral Responses with Blue (B) Filter .....	22
3	Spectral Response Curves with Red (R) Filter .....	23
4	Spectral Response Curves with Infrared (I) Filter .....	24
5	Albedo vs. Wavelength of Moon and Test Specimens .....	25
6	Photometry of Volcanic Cinder No. 4	
	a) E = 0° .....	26
	b) E = 30° .....	28
	c) E = 60° .....	30
7	Photometry of Furnace Slag No. 1	
	a) E = 0° .....	32
	b) E = 30° .....	34
	c) E = 60° .....	36
8	Photometry of Coral No. 2	
	a) E = 0° .....	38
	b) E = 30° .....	40
	c) E = 60° .....	42
9	Photometry of Scoria No. 2	
	a) E = 0° .....	44
	b) E = 30° .....	46
	c) E = 60° .....	48
10	Photometry of Copper Oxide Powder on Flat Board	
	a) E = 0° .....	50
	b) E = 30° .....	52
	c) E = 60° .....	54
11	Photometry of Copper Oxide Powder on Foam	
	a) E = 0° .....	56
	b) E = 30° .....	58
	c) E = 60° .....	60

<u>Figure</u>	<u>Page</u>
12 Volcanic Cinder No. 4 .....	62
13 Furnace Slag No. 1 .....	63
14 Coral No. 2 .....	64
15 Scoria No. 2 .....	64
16 Copper Oxide Powder (Magnified 25 x) .....	65
17 Copper Oxide Powder on Foam .....	66
18 Experimental Models of Suspended Particles .....	67
19 Photometry of Suspended Particles Model .....	68
20 Geometry of Four Contrived Photometric Models .....	70
21 Extent of Moon - Model Photometric Deviations	
a) Suspended Strip Model .....	71
b) Vertical Strip Model .....	72
c) Furrow Model .....	73
d) T-Model .....	74
22 Photometry of Vertical and Suspended Strip Models .....	75
23 Photometry of T and Furrow Models ( $b \leq a$ ) .....	76
24 Photometry of T and Furrow Models ( $b > a$ ) .....	77

## INTRODUCTION

In this second quarterly progress report we present the results of experiments and theoretical analyses touching upon all three phases of the program as originally outlined in Proposal B of Ref. 1.

Interpretation of the lunar photometric data (the major objective of this program) can be approached in various ways. One way is to search for natural specimens (i.e., dust, cinder, slag, etc.) that reproduce the photometric properties of the moon and try to find out from these experimental comparisons which physical properties of the lunar surface may or may not be inferred. Another way is to focus attention on the phenomenon that characterizes the reflection laws of the moon, namely backscattering, and to inquire which physical properties of reflecting surfaces in general determine their ability to backscatter light and what, in particular, these properties teach us about the nature of the lunar surface.

The first approach is more expedient and has been used extensively by workers in this field. We also used this technique with some success in Phase I of a previous contractual investigation (Ref. 2) under integrated (visible) lighting conditions. Phase I of the present investigation essentially pursues this technique under "spectral" lighting conditions. Similarly, in Phase II we measured the photometric properties of "suspended particles" under integrated lighting.

The second approach is theoretical in nature and could lead to greater insight and quantitative data on the physical properties of the moon or other reflecting celestial bodies of known photometric properties. This approach, used in Phase III, is an outgrowth of preliminary, qualitative analyses presented in Ref. 2. Essentially, the method consists of describing mathematically the photo-geometric relationship of various promising models and letting the computer search for the geometry that gives the closest photometric match with the lunar data. The models consist of idealized patterns of horizontal and/or vertical planes that, unlike the complex natural specimens or suspended particles investigated in earlier phases, lend themselves conveniently to analytical treatment.



WORK ACCOMPLISHED

During Phase I the albedo and brightness-phase curves at 0°, 30° and 60° viewing angles of all six natural specimens as originally proposed were measured with integrated visible light as well as at the following standard astronomical filters: Blue, Red and Infrared. The specimens that were investigated are as follows:

	<u>Figure Nos.</u>
1. Volcanic Cinder No. 4 .....	6 and 12
2. Furnace Slag No. 1 (original NASA sample) .....	7 and 13
3. Coral No. 2 .....	8 and 14
4. Scoria No. 2 .....	9 and 15
5. Copper Oxide Powder .....	10 and 16
6. CuO Powder on Foam .....	11 and 17

It was discovered in connection with the measurements made under this contract that results with silver chloride as originally proposed for specimens 5 and 6 are extremely dependent upon the accidental physical microstructure of the chemical as purchased. We procured this material as usual from Allied Chemical. It was discovered that the microstructure was changing in the sealed containers and that the material would no longer yield a good lutation signature. Purchase of new chemical was fruitless. The "fairy castle" microstructure could not be duplicated. No physical or chemical analysis has been made. The effect may be due to water or crystallization. However, other physical or chemical changes may have occurred. Consequently, silver chloride powder, as originally proposed for the last two specimens, was replaced by copper oxide because of the difficulties we experienced in maintaining its albedo and microstructure constant. Copper oxide powder (an equally good backscatterer) is more dependable in giving repeatable experimental results because, unlike silver chloride, it is not susceptible to darkening under exposure to sunlight.

The spectral responses of our photometric system with and without the filters have been analyzed and compared with those

of sun-photographic plate systems used in lunar observations as shown in Figs. 1 through 4. Albedo values at various viewing angles and wavelengths are listed in Table 1 and plotted in Fig. 5. A total of 72 photometric curves (12 for each specimen) at specified viewing angles and wavelengths are shown in Figs. 6 through 11. Photographs of the specimens are shown in Figs. 12 through 17. A discussion of the test results is also included in this report.

In Phase II, models of "suspended particles," made up of beads strung across vertically stacked horizontal frames, were constructed as shown in Fig. 19a. Brightness vs. phase angle measurements at 0°, 30°, and 60° viewing angles were taken for the various particle spacing to diameter ratios as shown in Fig. 18. The test results are shown in Figs. 19b to 19d.

In Phase III the photometric functions of four simple, basic geometries were derived. These geometries, shown in Fig. 20, are termed "suspended strips," "vertical strips," "furrow," and "T" models. An IBM 7094-II computer program was established to analyze these models and to compare the results with the lunar data under a wide range of boundary conditions. The results of the computer program are abstracted in Figs. 21 to 24 and are discussed with reference to their significance and future promise.

Table I  
ALBEDO - COLOR CHART

Color	Nominal Wave-length	Specimens																	
		Volcanic Cinder No. 4			Furnace Slag No. 1			Coral No. 2			Scoria No. 2			Copper Oxide on Flat Surface			Copper Oxide on Foam		
		0°*	30°	60°	0°	30°	60°	0°	30°	60°	0°	30°	60°	0°	30°	60°	0°	30°	60°
V	0.37-0.77	0.08	0.08	0.08	0.09	0.09	0.09	0.26	0.28	0.28	0.04	0.04	0.03	0.05	0.05	0.05	0.05	0.04	0.04
B	0.42	0.09	0.09	0.09	0.09	0.09	0.09	0.25	0.28	0.31	0.04	0.04	0.04	0.05	0.05	0.05	0.05	0.05	0.05
R	0.68	0.22	0.23	0.23	0.11	0.10	0.09	0.31	0.32	0.35	0.04	0.04	0.04	0.11	0.11	0.11	0.11	0.11	0.11
I	0.99	0.28	0.26	0.33	0.12	0.11	0.11	0.34	0.35	0.36	0.06	0.05	0.04	0.33	0.31	0.30	0.29	0.30	0.28

\*Angles refer to viewing angles

## PHASE I - SPECTRAL PHOTOMETRY

### Purpose

This phase was utilized to study, by means of laboratory measurements, the photometric behavior at all viewing and phase angles (including the "opposition" region) of natural specimens under integrated visible lighting and spectral lighting including the Blue, Red and Infrared regions.

### Spectral Response Studies

Throughout the photometric investigations conducted by Grumman to date, an assumption was made that the spectral response resulting from combining an artificial light source (tungsten-iodine lamp) and the sensor (S-4 or S-11 phototube) did not differ from the spectral response of photography on the sunlit moon to such an extent as to invalidate our measurements. The sensitivity of photometric functions of models to these spectral parameters was investigated under this contract. Figure 1 shows the approximate comparison of the integrated spectral response of our photometric analyzer with that of direct lunar photography. Much of the photographic data is rather old. Therefore, under the assumption that emulsions of different optical red sensitization have been used to acquire these data, a probable range of response is shown in Fig. 1. Film Emulsion IV represents the extreme red sensitization that might be incorporated into the direct lunar data, whereas Film Emulsion II represents the other extreme of an older blue-sensitive emulsion. The various spectral curves that have been multiplied together to achieve a response curve for the laboratory equipment include the following:

- 1) A 3200°K black body curve representing the output of a 3400°K tungsten-iodine lamp filtered through two diffuser disks. The exact amount of spectral reddening of the 3400°K source by the diffusers is unknown. However, the transmission of directional light through the diffusers is influenced by preferential scattering from the beam of blue over red.
- 2) The spectral transmission of two objective lens assemblies, one representing the collimating lens for the source, and the other the photometer objective.

- 3) The spectral reflectance curves for two rhodium mirrors.
- 4) The spectral response curve of a typical S-11 photoemissive surface (e.g., for the 6199 multiplier phototube).

The comparison of integrated response predicted for the photometric analyzer with the two sunlight-emulsion curves indicates that the analyzer is far too responsive in the red to represent photography with blue-sensitive emulsion, but is at least a possible compromise for photography with high red sensitization. In all probability, it is too red-responsive to represent most of the lunar photography.

More recent photometric data, including that reported by Gehrels et al., (Ref. 9), have been acquired with the use of phototubes rather than more indirectly through photography. With these data the comparison is between the product curves of the phototube spectral responses and the source curves, sunlight in one case and the tungsten-iodine lamp in the other. Of course, optics used somewhat modify both product curves. However, the major difference lies between sunlight (5700°K) and artificial light (3200°K), with the peak of the former occurring near 5000A and the latter near 9000A. Obviously again, the photometric analyzer weighs the data too heavily in favor of the red if the same photodetector surface is used in both direct lunar data and laboratory data. One can attempt to balance the integrated response by the use of filters, or by using different photo-detectors, or by some combination.

However, the emphasis in this report is not placed on making extremely close comparison with any given set of direct lunar observations, but on discovering general trends in the effect of spectral band pass on the photometric function. The integrated visual response photometric data have been taken with the RCA 6199 multiplier phototube. For the blue (B), the filter combination is the Schott GG-13 combined with the Corning 5-57. The (B) photometric functions were taken with the RCA 6199 phototube also. The integrated visual response curve is shown in Fig. 1. The integrated spectral (B) curve of the photometric analyzer with these filters is shown in Fig. 2.

For the red (R), the filters are Schott BG-38 and the Corning 2-64. For the infrared (I), the filter is the Corning 7-56

with the upper wavelength cutoff being furnished by the photo-detector. For these two band pass arrangements, the RCA 7102 multiplier phototube was used and the integrated response curves are derived and shown in Figs. 3 and 4.

It should be noted that the spectral curves submitted in this report are based upon typical S-11 and S-1 room temperature curves (for RCA 6199 and RCA 7102, respectively), and not upon calibration data for specific phototubes. For very narrow spectral bandpass, the spectral curves of all other components become insignificant compared to that of the filter since all photometric curves are normalized "relative value" curves. As the bandpass increases, additional significance may be attached to the other component spectral curves. However, an examination of the data on all models tested under this contract shows a lack of pronounced spectral effect, and therefore, small significance to exact spectral data.

#### Discussion of Test Results

The investigation of the six natural specimens presented in this report differs from the investigation of the same specimens in Ref. 2 in the following respects:

- 1) Albedo and photometric measurements were made at discrete wavebands including the blue, red, and infrared regions, in addition to those measured through the full visible spectrum.
- 2) More reliable measurements of the change in brightness near  $0^{\circ}$  phase angle (the "opposition" region) were made at all the specified wavelengths by means of the improved beam splitter previously described in the preceding progress report (Ref. 3).

#### Spectral Albedo Measurements

Albedo values at all of the measured viewing angles and colors are listed in Table 1. Most of the albedos are within lunar ranges and like the lunar surface are nearly independent of viewing angle and dependent upon wavelength. Volcanic Cinder No. 4 exhibits an unusually higher albedo in the red and infrared regions than in the blue and visible.

Plots of albedo vs. wavelength for the test specimens and the moon are shown in Fig. 5. Scoria No. 2 shows the least color

dependence whereas CuO powder shows the most. In the region of the spectrum shown in Fig. 2, Scoria No. 2 and Furnace Slag No. 1 show a better fit with the albedo-color curves of the moon than the other specimens we examined.

It is reasonable to attribute the viewing angle independence of albedo exhibited by the moon and our specimens to geometry effects or roughness of the surface, but it is not clear whether roughness also plays a role in the color dependence of albedo or whether this dependence is entirely a compositional effect. The moon appears to show considerable enhancement in brightness at longer wavelength. Recently reported lunar measurements at  $3.6\mu$  (not shown in Fig. 2) reveal albedo peaks of 0.25 for the maria and 0.55 for the highlands (Ref. 4). Similarly, brightness measurements of Mare Tranquillitatis from a balloon altitude of 83,500 feet reveal a uniform rise in albedo with wavelength to a peak of 0.20 at about  $2.5\mu$  (Ref. 7). These values are considerably higher than those in the optical region of the spectrum and could possibly account for the increased contrast between illuminated and shadowed areas of the lunar surface revealed by recently published near infrared (1 to  $2\mu$ ) photographs of the moon (Ref. 8).

Further discussion of this subject is not very meaningful at this time in view of the limited extent of albedo-color data on the moon and terrestrial specimens. One may note, however, that if the brightness contrast of the moon is much greater in the near infrared than it is in the optical region, as it appears to be according to data in Refs. 4 and 7, then additional albedo-color data on the moon and laboratory specimens would be very useful in compositional mapping of the moon and in interpreting photographs or data obtained at these relatively unexplored near infrared wavelengths. Within the range of lunar surface temperatures, it is safe to assume that at these wavelengths thermal emission is negligible and that the observed phenomena are predominantly due to scattering.

#### Spectral Photometric Measurements

Figures 6 through 11 show the visual and spectral photometric curves of six natural specimens. The photographs of these specimens are shown in Figures 12 to 17. Twelve measurements were made on each specimen at B, R, I, and V wavebands for each of the  $0^\circ$ ,  $30^\circ$ , and  $60^\circ$  viewing angles. Lunar photometric standards to which the test results are compared are taken from Ref. 2.

With the exception of the copper oxide powder and to a lesser extent sea coral, all the specimens show a more pronounced surge of brightness at zero phase angle than they did during the previous measurements reported in Ref. 2. Volcanic Cinder No. 4 is the most notable in this respect. The difference between the old and new results in the "opposition" region is due to the already reported modification of the beam splitter used during near zero phase angle measurement. The new results at these difficult to measure phase angles are, we believe, superior in quality to the old ones and are in better agreement with corresponding lunar data recently published by Gehrels et al (Ref. 9).

It is of interest to compare the spectral-photometric behavior of the test specimens at very small and very large phase angles. The four photometric curves at B, R, I, and V of each specimen at any one of the three viewing angles are shown on opposite pages so that this comparison can be readily made.

The wavelength dependence of brightness at zero phase angle (in the "opposition" region) is clearly noticeable in Volcanic Cinder (Fig. 6), Furnace Slag (Fig. 7), and Scoria (Fig. 9). This dependence is in the direction of increased brightness with wavelength and is consistent with the albedo vs. wavelength data discussed above, except for the coral specimen where we notice an opposite trend although at a much attenuated scale. Recalling the fact that the test curves are normalized at  $4^{\circ}$  phase angle, we notice that (with the exception of the coral) the opposition effect is the least pronounced in the blue and the most pronounced in the red or infrared depending upon the specimen. In most cases,  $0^{\circ}$  phase brightness at V is comparable to the brightness at R or I. It is also of interest to note that the opposition effect on the CuO powder sprinkled on a flat surface is barely noticeable (Fig. 10) but it is clearly visible when the same powder is sprinkled on the rough "picked out" foam (Fig. 11). This experiment indicates that the opposition effect is roughness dependent and suggests that the scale of roughness of the lunar surface is larger than the micron size CuO powder.

The large phase angle regions of the test curves are also of interest in view of Gehrels' recent observation of "reddening" of the moon at these angles. The test data, as presented in this report, enable one to look for such an effect by comparing visually the brightness of a specimen at various colors at a given large phase angle. We notice that the coral is the only

specimen that exhibits this effect. In this case, we may safely attribute the "bulge" in the lower part of the brightness-phase curve to actual "reddening" rather than to other causes that may produce the same result such as geometry effects (discussed in Phase III) or specularly of the surface. The latter effect may be ruled out on the basis of the fact that the "bulge" appears only under spectral light and is more pronounced in the red and infrared than in the blue. Moreover, the reddening exhibited by the coral at large phase angles is consistent with its anomalous spectral behavior in the opposition region as noted above.

As far as the six natural specimens indicate, their over-all photometric behavior under integrated light does not seem noticeably different under "spectral" conditions. This observation is particularly true for fine copper oxide powder on a flat surface which shows the least color dependence and opposition effect. The differences in the very small and very large phase angle regions exhibited by the other specimens, as discussed above, appear to be due primarily to color and albedo effects since the geometry of the specimens remains the same. It is not clear at this point whether the very fine powdery make up of copper oxide is responsible for its anomalous behavior. It is reasonable to conjecture that the spectro-photometric properties of the moon in the optical region, like those of our test specimens, are not significantly different from the photometric properties at integrated visible light. New lunar photometric measurements should preferably be made at wavelengths beyond the optical region. Additional backscattering data at longer wavelengths could be useful in inferring a more meaningful lower limit for the micro-roughness of the lunar surface. The study of the phase variation of the moon and laboratory models in the near infrared (up to  $3\mu$ ) would be of great value in this respect. Earth-based measurements of the photometric properties of the moon at these wavelengths are possible and would be very useful at this time in furthering our knowledge of the microstructure and other properties of the lunar surface.



## PHASE II - PHOTOMETRY OF SUSPENDED PARTICLES

### Purpose

This phase was used to study, by means of analysis and/or experiments, the reflection properties of "suspended particles" recently proposed in the literature (Ref. 9) as a lunar photometric model.

### Analysis

In addition to experiments discussed below, we are also attempting to develop an analytical approach to the study of the phase variation of the brightness of a model consisting of a "cloud" of discrete, shadow casting particles within which multiple scattering and diffraction effects are neglected.

The geometrical analysis of a multilayer model of known particle distribution appears to be extremely laborious and difficult. Reducing the number of layers to just a few could facilitate the solution but not without compromising its significance. We have not found at this point a convenient and meaningful theoretical approach to the photometry of highly porous, suspended, granular media that would either complement or verify Hapke's solution to this problem in terms of the density or porosity of the medium. However, it is too early to state that an independent solution to this problem cannot be worked out.

### Experimental Models

In addition to the analytical studies discussed above, we have constructed models simulating suspended particles to measure the brightness-phase angle dependence. The experimental models consist of opaque "macroscopic" spheres or beads of uniform albedo and diameter suspended on thin strings of negligible shadow casting capability. The beads are 3 mm diameter plastic spheres with a hole through the center. Four frames of plywood were made with an open "working" area of 5 x 12 inches and an adjoining open "storage" area of 2 x 12 inches as shown in Fig. 19a.

The beads are strung on fine nylon string, 22 beads per strand. Each frame has 10 equally spaced (30 mm apart) strands of beads. The beads were sprayed with Krylon Flat Black Paint

as a prime or base coat. The prime coat is necessary because the brown water paint desired for proper "Lambertian" reflection would not adhere to the smooth surface of the plastic beads.

The brown paint used was Series 600 Gothic non-toxic Tempera, made by Sargent Manufacturing Corporation of Hazelton, Pennsylvania. A similar surface treatment was given to a masonite flat board used as a backdrop to the beads during photometric measurement.

Five models have been investigated. These models, numbered from 1 to 5, are illustrated in Fig. 18 and are described as to the spacing-to-diameter ratios of the particles in the three orthogonal directions, the number of layers, and the number of particles per unit, 30 x 30 mm viewed area. The largest particle spacing used is 30 mm, giving a particle spacing-to-diameter ratio of 10 to 1 as used by Gehrels (Ref. 9) in his proposed lunar photometric model.

### Discussion of Test Results

The following comments may be made at this time based on the preliminary test results shown in Figs. 19b through d:

- All of the investigated "suspended particle" models show a very poor fit with the lunar curves, as we generally expected, particularly at large phase and viewing angles.
- The photometric behavior of Model No. 2, having a 10 to 1 particle spacing-to-diameter ratio, is barely distinguishable from that of a similarly treated flat surface having no particles (Model No. 1).
- The models having a denser population of particles show a noticeable increase of backscatter with increasing particle density.
- The general trend of the five investigated models, all having porosities higher than 99 percent, indicates that very high porosities of this order are not compatible with the lunar photometric data.

The most dense model, No. 5, exhibits local, secondary brightness peaks that are probably due to the presence of a sufficient number of particles whose shadows come into view at certain phase angles (low spots on the curve) but disappear at larger phase angles (high spots) when light reaches these areas through the interstices of the particles. This phenomenon, which is not observed on the moon, is also exhibited by the "suspended strip" models discussed in Phase III.

The bead models are, at best, a crude simulation of a cloud of suspended particles. It would be premature at this time to look for further meaning in the test results and to speculate about their lunar implications without further experimental refinements or analytical studies that are currently under consideration. The models that we have used have at least two major shortcomings imposed mainly by experimental difficulties: 1) they are not sufficiently deep to approximate the condition of a relatively thick cloud, and 2) their surface treatment leaves much to be desired. Although the paint we used has the proper albedo, it has sufficient gloss to obscure the test results at large phase and viewing angles. The deviation of the test curves from the lunar curve at  $30^\circ$  and  $60^\circ$  viewing angles in Figs. 19c and d are due to specularities in the paint. The results would be more meaningful if this effect is eliminated. We are currently looking for a paint that reflects light according to Lambert's Law.

## PHASE III - GEOMETRY OF BACKSCATTERING SURFACES

### Purpose

This phase was planned: 1) to investigate and develop empirical relationships, in terms of the physical and optical properties of surfaces, that obey the reflection laws of the moon for both uniform and "composite" albedo conditions, and 2) to estimate porosity factors from the photometric signatures of contrived models in an attempt to determine a range of porosities consistent with existing lunar photometric observations including recent data on "opposition effect," albedo, and "color-shift."

The general purpose of this analytic and/or experimental exercise is not necessarily to proliferate the number of lunar photometric models for their own sake or to replace the natural specimens investigated herein or elsewhere, but to explain why surfaces in general reproduce or fail to reproduce the lunation curves of the moon, and to enable one to identify and estimate those useful "engineering" properties of the lunar surface that are photometrically relevant.

### Analytical Models

In their quests to reproduce the lunation curves of the moon, several investigators have in the past constructed hypothetical surfaces comprised of elements of known geometry and albedo, and arranged in a variety of patterns thought to be analogous to either natural specimens or to the moon itself. Examples of such controlled theoretical models are those of Barabashev (grooves and clefts), Shoenberg (spherical domes), and Bennet and Van Diggelen (hemi-ellipsoidal cups). In conjunction with the above variety of geometrical shapes, these investigators made use of different forms of the optical scattering law including those proposed by Lambert, Lommel-Seeliger and Fessenkov. Though a moderate degree of success was achieved, the results in most cases were decisively negative with respect to lunar observations at large phase angles. Despite the limited success achieved thus far with these controlled models, the search still continues for a simplified lunar photometric model composed of elements that lend themselves to easy manipulation and analysis.

Based on the results of recent experiments (Ref. 2), there is strong likelihood that backscattering surfaces possess a

tri-dimensional structure comprised of shadowcasting opaque elements larger in size than wavelengths in the optical region. With reference to the lunar surface, it appears quite possible that the irregularities on the surface, whatever their particular form may be, may cast shadows that grow larger as the angle of incidence of the radiation from the sun increases. Because the shadow casting elements may not in fact be within the telescopic resolution of present day instruments, the peculiar photometric signature of the moon may be due in large part to the combined effects of a great number of superimposed shadows that behave additively and eventually become dominant.

Several of the "natural" and "artificial" specimens investigated experimentally at Grumman and elsewhere are known to possess a tridimensional structure, but any rigorous analysis based on the actual geometry of their surface is prohibitively difficult. To circumvent these theoretical difficulties, but at the same time accomplish something in the way of useful analysis in terms of relative geometry and ratio of solid elements to voids, we have in this phase continued the work with tridimensional contrived models that was initiated and reported in Ref. 2. The four "simple" models selected for detailed quantitative analysis are those shown in Fig. 20 and are comprised essentially of an orderly array of horizontally suspended and/or vertical elements of low albedo whose surfaces reflect light according to Lambert's Law. The elements themselves are oriented in such a way relative to the plane of vision that they cast shadows as the light source moves from left to right along the intensity equator. Though it is fully recognized that the assumption of "Lambertian" elements may not be the best, and that other forms of the scattering law may be more realistic from the point of view of reproducing the lunar photometric signature, we feel at this time that regardless of the scattering function selected, it will not be as important as the dominant effect of geometrical shadowing. The assumption of low albedo allows us to neglect multiple reflections that would, if anything, tend to wash out those dark areas in shadow. The absence of diffraction effects also facilitates the analysis and follows from the assumption that the relative sizes of the reflecting elements are chosen to be analogous to the lunar features only on a macrorough scale. Edge effects are also neglected.

Because of the periodic nature of each of the geometries selected and their assumed distance from the light source, the analyses (see Appendix) were performed in terms of the smallest possible unit structure of each of the configurations, utilizing

parallel ray optics. These "unit structures" consist essentially of a horizontal or overhanging member and a portion of the underlying base material that is both illuminated and observed by the photometer. This approach to the analyses generally led to satisfactory numerical results, but some numerical difficulties did appear in the computations for the suspended strip model at large viewing, hence, large phase angles. Since there are no vertical strips present in this model to block either the photometer's field of view or the direction of the incident light, extra portions of the base material had to be considered. (The characteristic second brightness peak for this model at the larger phase angles is a direct result of the latter). There is no question that the size of the "unit structure" and hence their number per unit area included in the field of view of the photometer, will affect the general character of the photometric signatures for all models considered under experimental conditions. Some preliminary experimental results (Ref. 2) using triangular prisms indicate that there is a general increased smoothing effect on the photometric curves as the size of the prisms is reduced and more are added to the field of view. At this point it is believed that the smoothing effect is due to the decrease in the size of the shadows cast relative to those surfaces that are illuminated and viewed. In future analyses attempts could be made to consider the relative sizes and number of the shadow casting elements.

### Discussion of Analytical Results

The results of the computer analysis described in the Appendix were abstracted and are presented graphically in Figs. 21 through 24. Figures 21a through 21d represent plots of the sum of the squares of the deviations ( $\Sigma\Delta^2$ ) as a function of  $b$ , for constant values of  $h$ . As can be observed, the general character of the curves is oscillatory with the deviations tending to reach minima with increasing values of  $b$ . In some cases the results for particular values of  $h$  were omitted, the reason being that these solutions were highly irregular. These omissions did not, however, lead to any loss in our ability to confirm some already existing notions as to what general set of configuration parameters and viewing angles would result in the minimum deviation from the known lunar observations. In all instances, it appears as though the best results are achieved for a viewing angle of  $0^\circ$  as is to be expected, because most of the difficulties, both theoretically and experimentally, seem to occur at the larger phase angles. In both the "T" and Furrow model cases, where the analyses were carried out for values of  $b$  greater than  $a$ ,

one can observe the "bottoming out" of the curves for the  $0^\circ$  viewing case. As this does not occur for the other viewing angles, we can only conclude that for these cases, sufficiently high values of  $b$  had not been achieved.

In Figs. 22 through 24 we have superimposed on the standard lunation curves the photometric signatures for all models and viewing angles that represented the closest match, in the sense that the sum of the squares of the deviations from the lunar data were minima. In the interest of brevity, the results for the Suspended Strip and the Vertical Strip models, and the "T" and Furrow models, were grouped together such that for each graph three curves, including the lunar standard, are presented for comparison.

The results for the Suspended Strip, Vertical Strip, and "T" models tend to corroborate in general most of the features previously predicted for these models in Ref. 2. The "cosine type" curve obtained at large phase angles is due to the cessation of shadow lengthening in the areas viewed by the photometer and to the diffuse reflection of light from the other areas. In the case of the suspended model, the characteristic second brightness peak predicted by Hapke and us occurs for all viewing angles and is due to the illumination of those portions of the base material between adjacent "unit structures" as described in the previous section on analytical models.

Turning now to the two configurations that we feel will eventually contribute more to our understanding of surface porosity, we can in summary make the following observations concerning the "T" and Furrow Models:

- 1) The generally closer matches for these models for values of  $b > a$  as opposed to those for  $b < a$ , suggest a higher estimate on the lunar surface porosity than had been suspected previously.
- 2) The  $E = 60^\circ$  viewing case is the most critical in the sense that the greatest deviations from the lunar standard occur here and decrease generally towards more favorable matches as we approach  $E = 0^\circ$ .
- 3) There is nothing unique about the  $E = 0^\circ$  viewing case since the results for both models in this instance are identical.

- 4) For the T-Model  $b > a$ , the optimum spacing is revealed at  $E = 60^\circ$ , whereas the optimum height is revealed at  $E = 30^\circ$ . At  $E = 60^\circ$  all the  $(\Sigma\Delta^2)'_s$  are alike for  $b = 2$  and  $h > 2$ , whereas for  $E = 30^\circ$  there is a unique  $h$  dimension. Hence the  $30^\circ$  and  $60^\circ$  viewing angle data complement one another in suggesting a model that is unique insofar as horizontal spacing and vertical dimensions are concerned.

In concluding this phase of the work with contrived models, we should emphasize that the results to date should not in any sense be considered final. As set up, the form of the equations in the analysis is quite flexible and readily lends itself to inclusion of other forms for the scattering law. In addition, the average reflectivity values could be varied in future computations to dramatize the effects of "composite albedo." As far as subsequent improvements concerning the models themselves are concerned, several suggestions can be made at this point, including the following:

- 1) "Lips" or secondary roughness elements should be added to the horizontal elements of the T-model to obtain better photometric matches at the smaller phase angles.
- 2) Secondary holes in the stem or vertical elements of the T-model should be included, the latter to improve the brightness results at the larger phase angles.

The two improvements cited above should contribute substantially towards a better and more instructive contrived model of the uppermost layer of the lunar crust, at least in the photometric sense.



## CONCLUSIONS AND RECOMMENDATIONS

In Phase I, where our major objective was to study experimentally the wavelength dependence of albedo and photometry, we found that the over-all photometric function of the six investigated specimens, unlike their albedo, is relatively insensitive to changes in wavelength within the investigated spectrum interval of about  $0.42\mu$  to  $0.99\mu$ , except at very small and very large phase angles where color effects appear to predominate.

At the very small phase angles (referred to in the literature as the "opposition" region) we were successful in reproducing, by means of instrumental refinements, the nonlinear surge of brightness recently observed on the moon shortly before and after an eclipse. The observed opposition affect is most pronounced on coarse volcanic cinders and least pronounced on fine copper oxide powder. It was also observed that the backscatter in the opposition region, unlike the regions beyond it, is wavelength dependent. The brightness in this region is more pronounced in the red end of the spectrum than in the blue end for all of the investigated specimens except for the sea coral which also differs from the other specimens in exhibiting a noticeable reddening at very large phase angles as recently observed on the moon.

No major significance can be attached to the above observations at this time other than the fact that the opposition phenomenon recently observed on the moon has been duplicated in the laboratory and that it appears to be largely due to a combination of roughness and color effects. It also appears that the backscatter exhibited by our test specimens and probably by the moon is nearly independent of wavelengths within the optical range and that more information can be gained by extending photometric measurements of the moon and of terrestrial analogs (in the laboratory or in the field) to longer wavelengths (such as in the near infrared) than by confining the studies to the shorter wavelengths used to date. It is known, for instance, that the moon is limb bright at optical wavelengths but limb dark at radar wavelengths. Closing the gap in our knowledge of the reflection properties of the moon between these two wavelength regions could conceivably lead to a better estimate of the microstructure of the lunar surface, and aid in the search of those lunar areas that are relatively free of "sub-telescopic" topographic roughnesses. Such an earth-based effort could precede or follow the mission of unmanned lunar probes and complement the finding of these high-resolution probes in identifying suitable lunar landing sites. We recommend that high-spatial resolution lunar photometric measurements at near infrared

wavelengths (1-3 $\mu$ ) be initiated as soon as possible and that the feasibility of scanning the moon with laser beams at longer wavelengths be looked into. The latter measurements would of necessity be confined to a study of limb darkening rather than of brightness variation with phase angle. The investigations of laboratory analogs at these wavelengths could precede the actual lunar measurements.

Appreciable progress has been made in Phases II and III of this contract, dealing respectively with the photometry of "dust clouds" and contrived models. Further results will be evaluated upon the completion of the work.

## REFERENCES

1. Photometric Measurements of Simulated Lunar Surfaces, Grumman Research Department Proposal RP-255, File No. 65-83NAS, June 1965.
2. Halajian, J. D., Photometric Measurements of Simulated Lunar Surfaces, Interim Report, Contract No. NAS 9-3182, Grumman Research Department Report RE-219, July 1965.
3. Halajian, J. D., and Spagnolo, F. A., Photometric Measurements of Simulated Lunar Surfaces, Quarterly Progress Report, Contract No. NAS 9-3182, Grumman Research Department Memorandum RM-297, October 1965.
4. Markov, M. N., and Khokhlova, V. L., "Coefficients of Emission in the Infrared of the Lunar Seas and Continents," Soviet Physics-Doklady, Vol. 9, No. 8, February 1965.
5. Harris, D. L., "Photometry and Colorimetry of Planets and Satellites," In Planets and Satellites, G. P. Kuiper and B. M. Middlehurst, Editors University Chicago Press, 1962.
6. Sharanov, V. V., "Some Results of Photometric and Colorimetric Comparison of Terrestrial Volcanic Crusts with the Lunar Surface," Annals of the N.Y. Academy of Sciences, F. 123, Art. 2, p. 741-750.
7. Wattson, R. B., and Danielson, R. E., "The Infrared Spectrum of the Moon," Astrophysical Journal, Vol. 143, No. 1, July 1965.
8. Kuprevitch, N. F., "New Data on the Structure of the Lunar Surface," Soviet Astronomy, Vol. 7, No. 5, March-April 1964.
9. Gehrels, T., Coffeen, T., and Owings, D., "Wavelength Dependence of Polarization of the Lunar Surface," Astronomical Journal, Vol. 69, No. 10, December 1964.

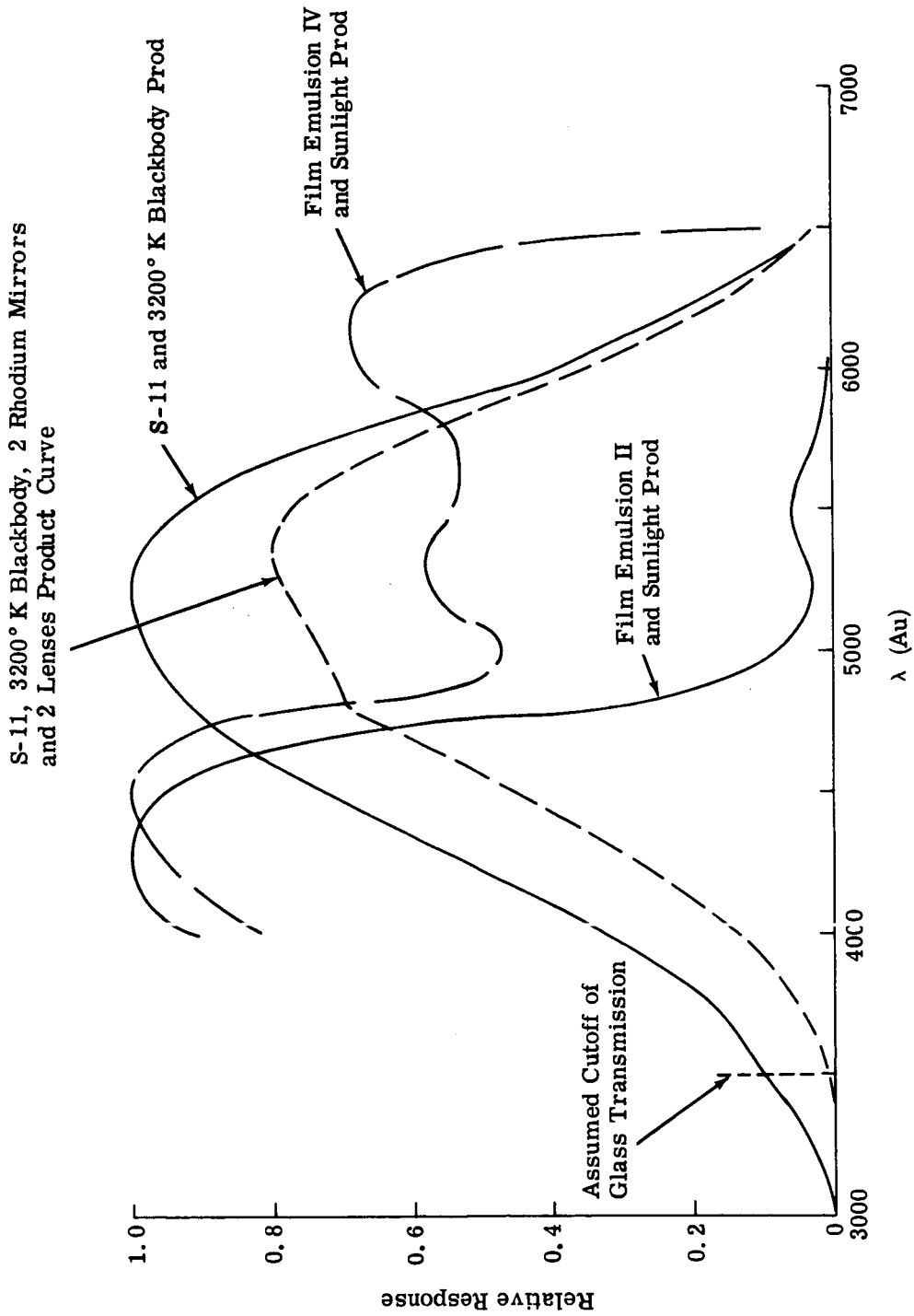


Fig. 1 Spectral Responses at Integrated Visible (V) Light

Code:

- ① ——— Tungsten - Iodine Lamp Thru Two Diffusers (3200° K Blackbody)
- ② ——— RCA #6199 Photomultiplier Tube Detector
- ③ ——— Filter (GG13 and 5-57 Product) Blue
- ④ ——— Lamp, Detector and Filter Product
- ⑤ ——— Lamp, Detector, Filter and System Lenses Product

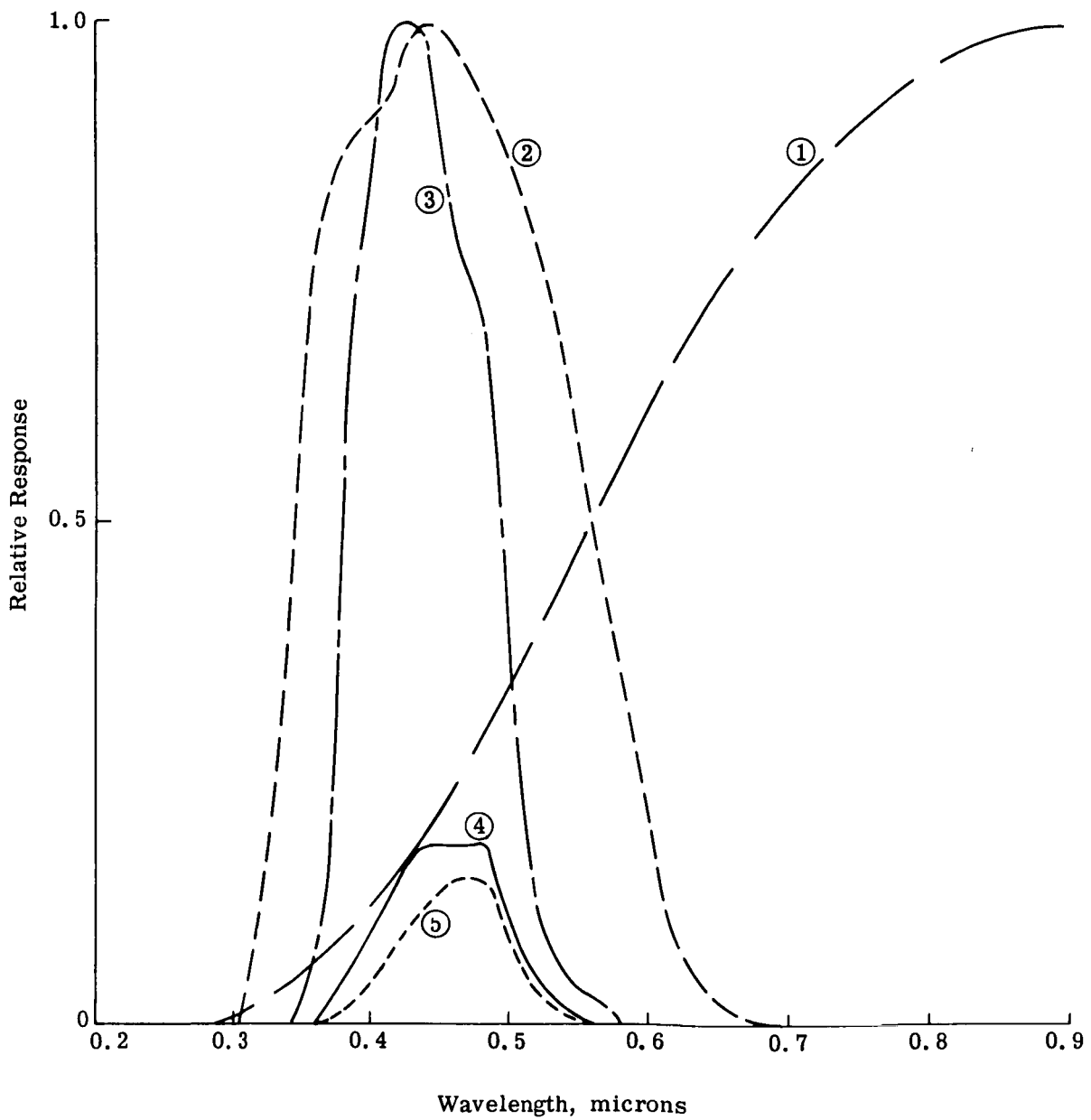


Fig. 2 Spectral Responses with Blue (B) Filter

Code:

- ① ——— Tungsten - Iodine Lamp Thru Two Diffusers (3200° K Blackbody)
- ② ——— RCA #7102 Photomultiplier Tube Detector
- ③ ——— Filter (BG 38 and 2-64 Product) Red
- ④ ——— Lamp, Detector and Filter Product
- ⑤ ——— Lamp, Detector, Filter and Two Rhodium Surface Mirror Product

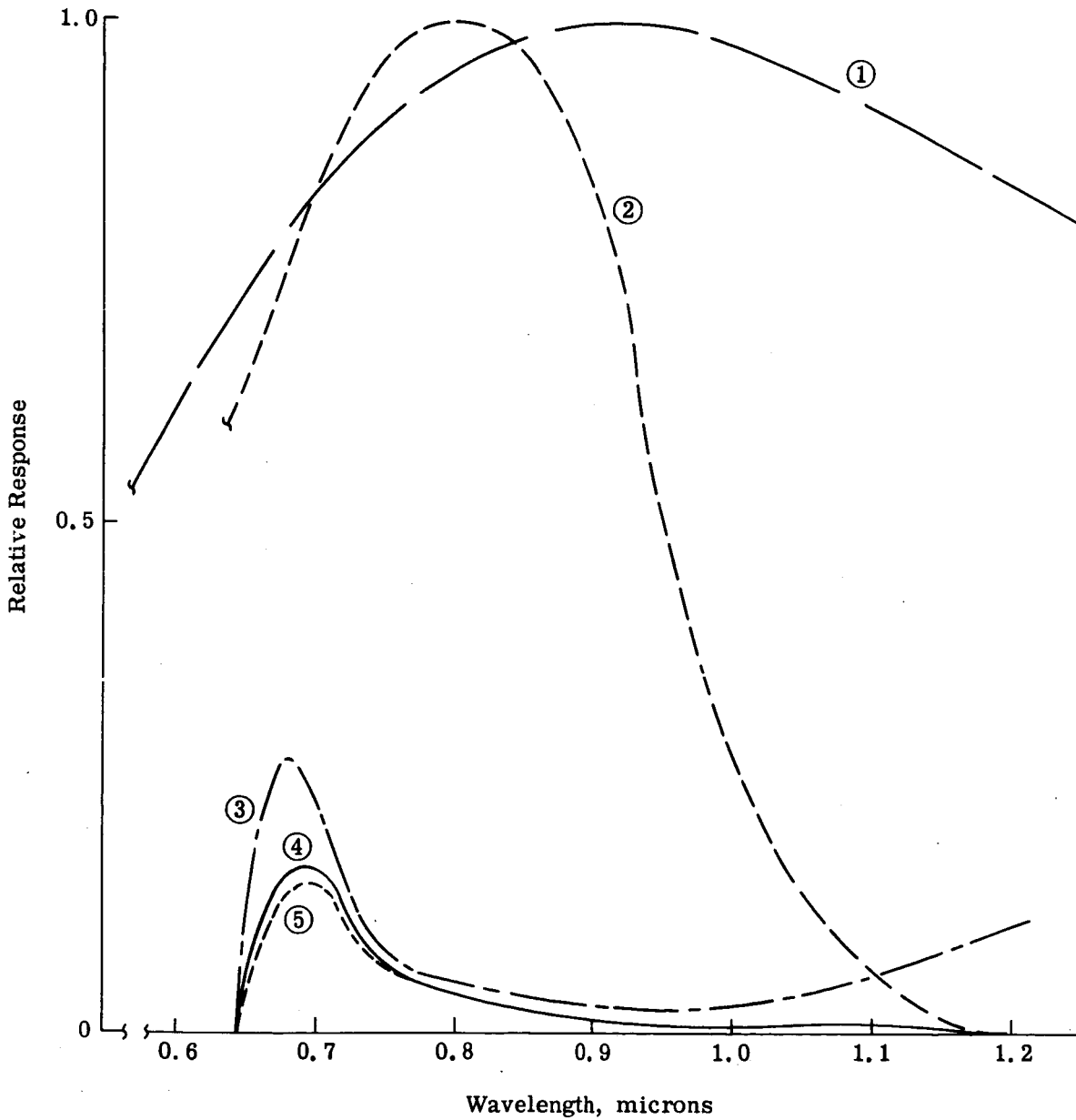


Fig. 3 Spectral Response Curves with Red (R) Filter

Code:

- ① ——— Tungsten - Iodine Lamp Thru Two Diffusers (3200° K Blackbody)
- ② - - - - RCA #7102 Photomultiplier Tube Detector
- ③ - - - - Filter (IR 7-56)
- ④ ——— Lamp, Detector and Filter Product
- ⑤ - - - - Lamp, Detector, Filter and Two Rhodium Surface Mirror Product

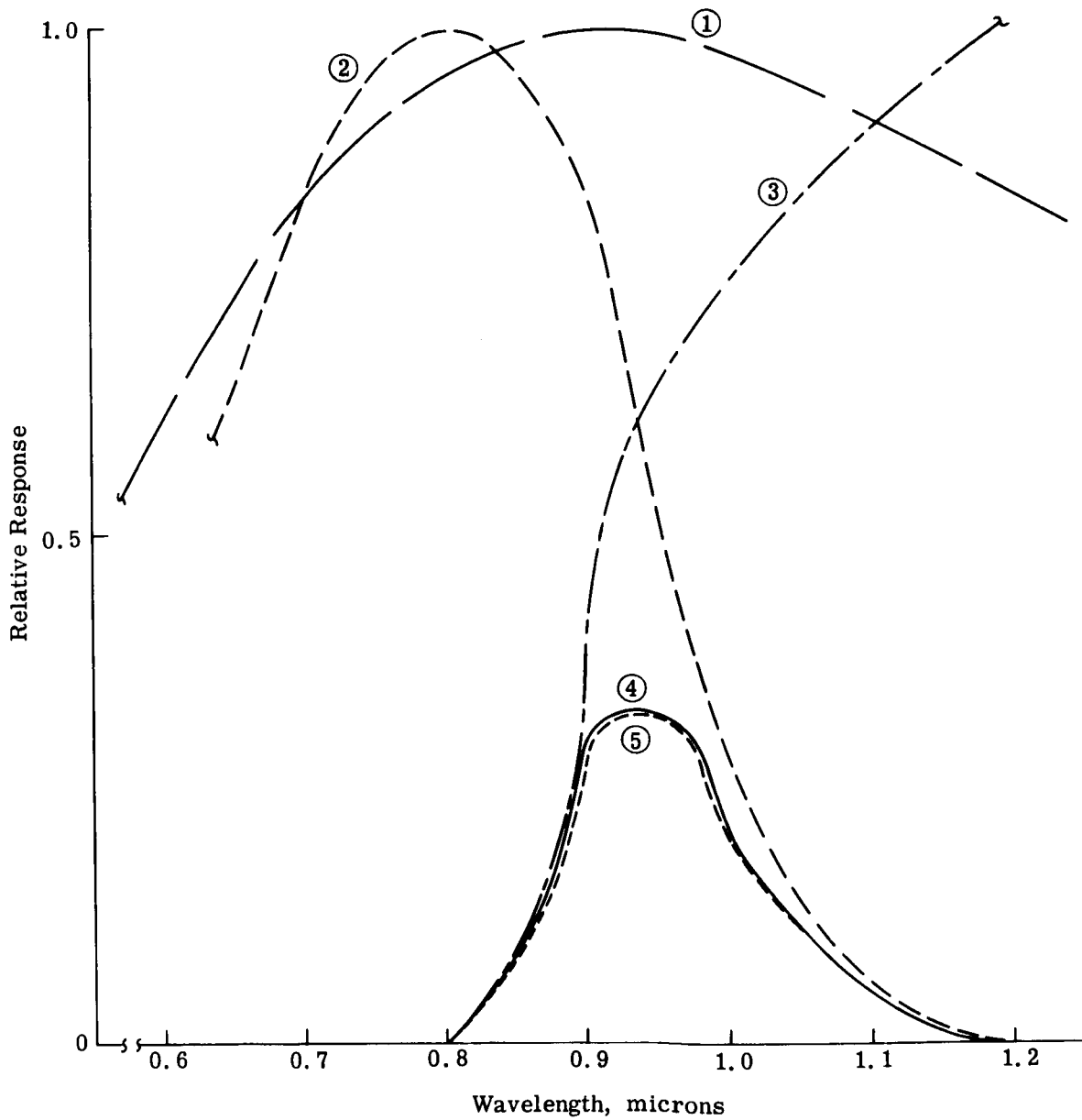


Fig. 4 Spectral Response Curves with Infrared (I) Filter

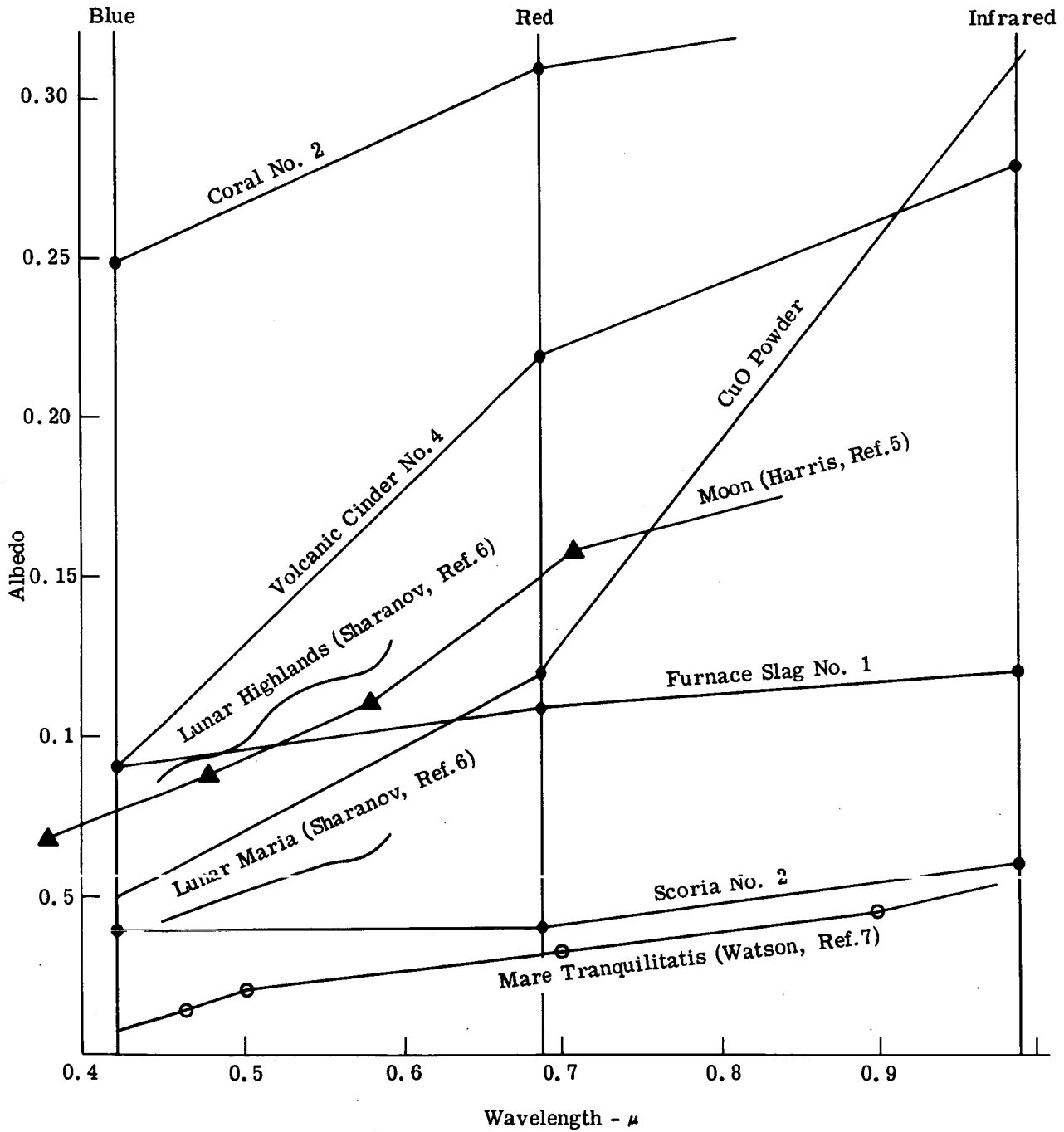
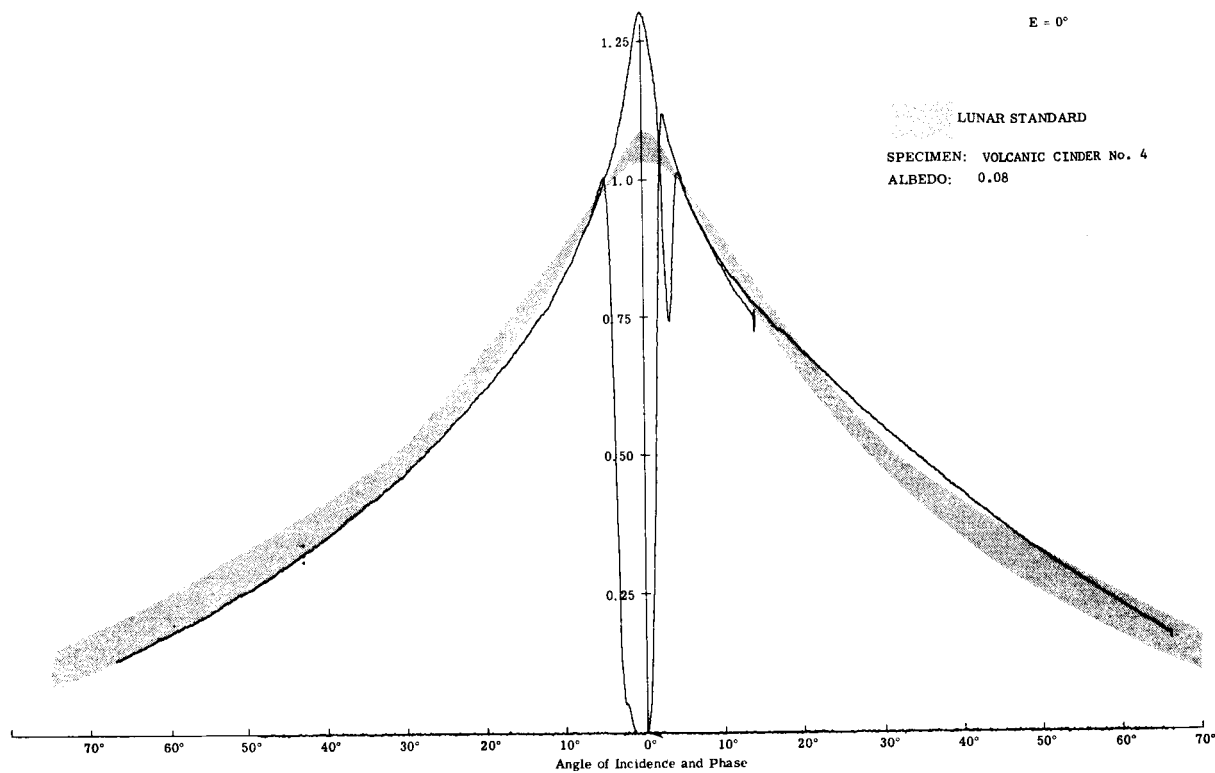
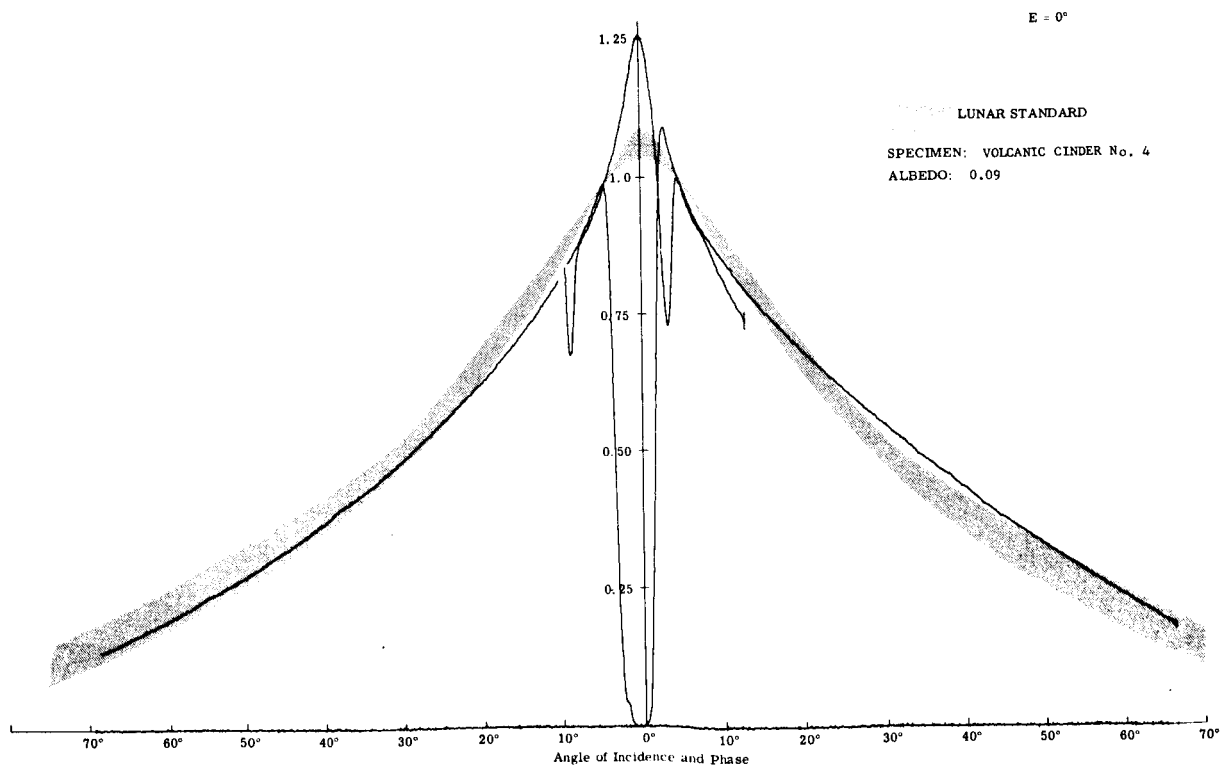


Fig. 5 Albedo vs. Wavelength of Moon and Test Specimens



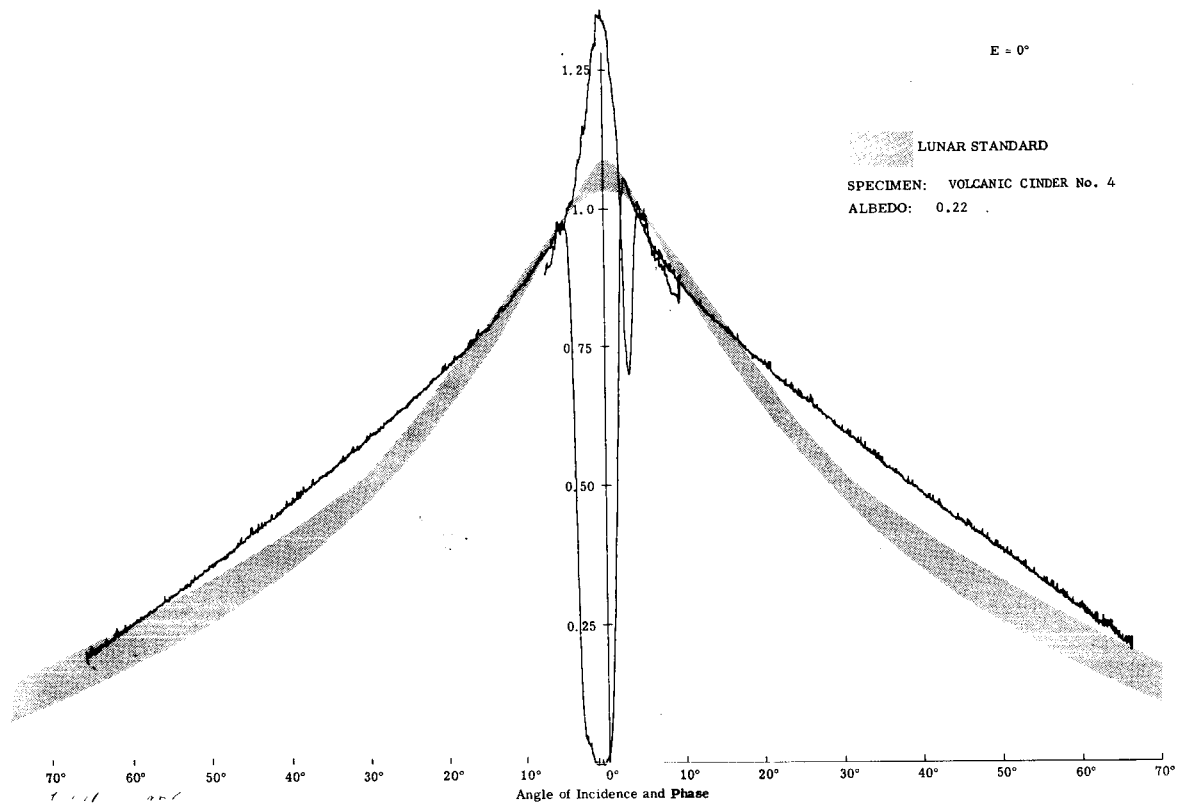


**Visible**

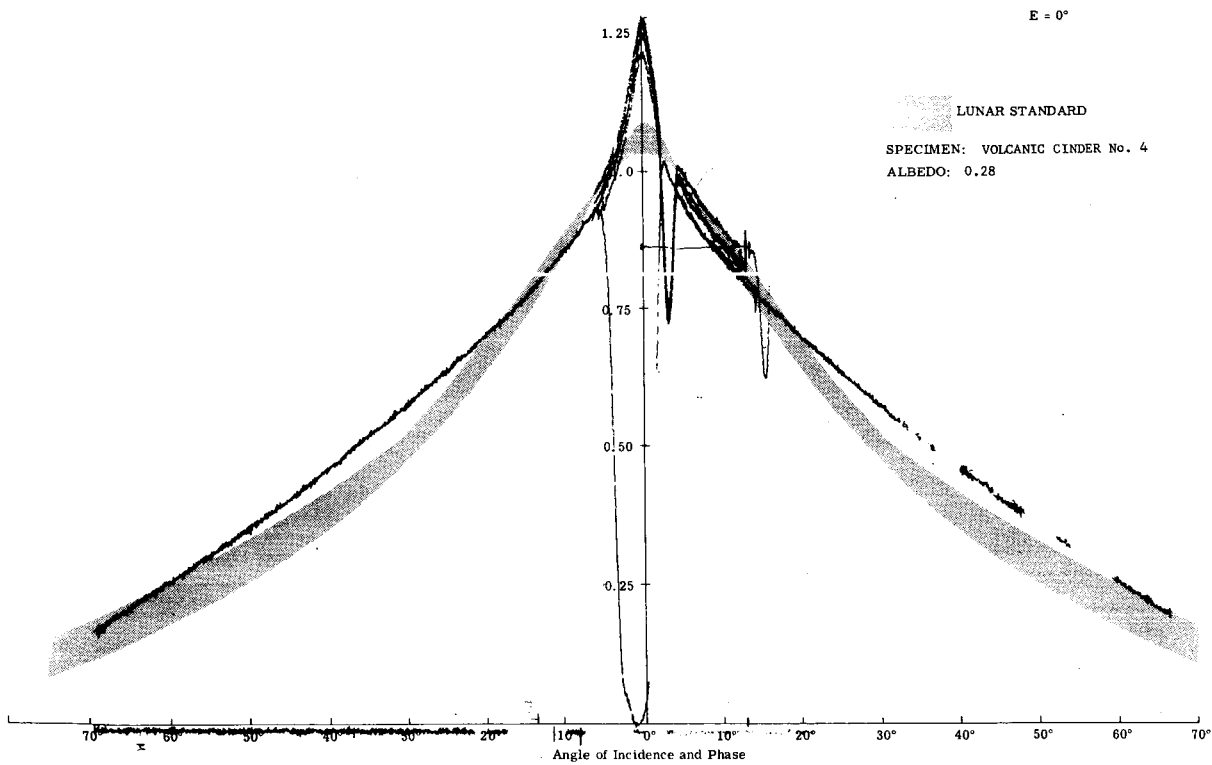


**Blue**

Fig. 6a Photometry of Volcanic Cinder No. 4 (E = 0°)



Red



Infrared

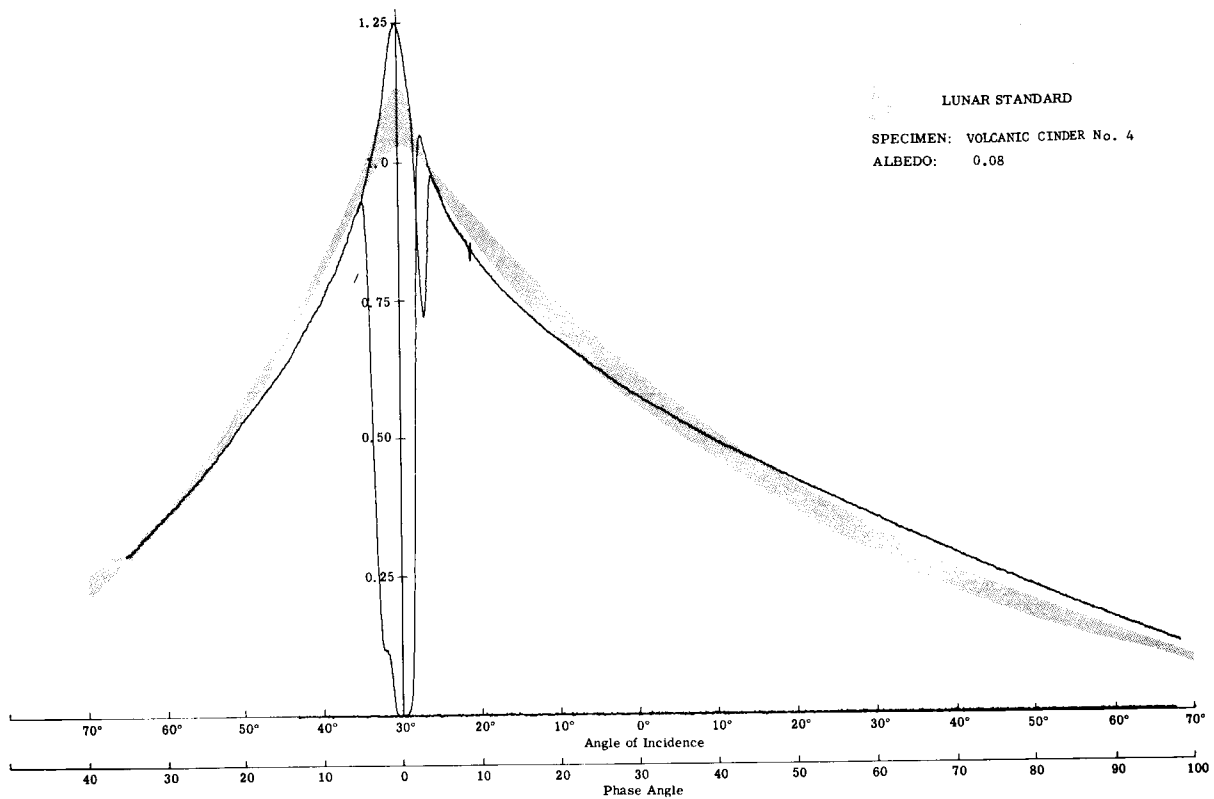
Fig. 6a (Cont) Photometry of Volcanic Cinder No. 4 (E = 0°)

Research Dept  
RM-308  
January 1966

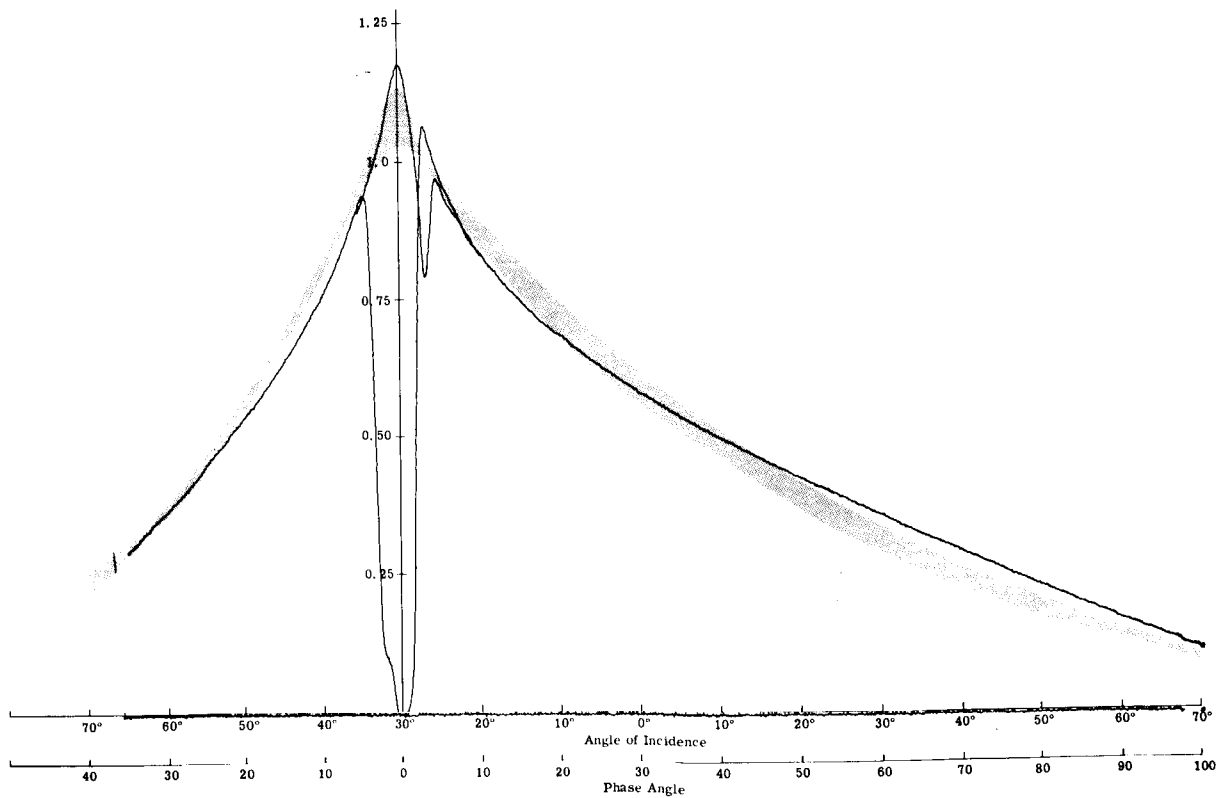
E = 30°

LUNAR STANDARD

SPECIMEN: VOLCANIC CINDER No. 4  
ALBEDO: 0.08



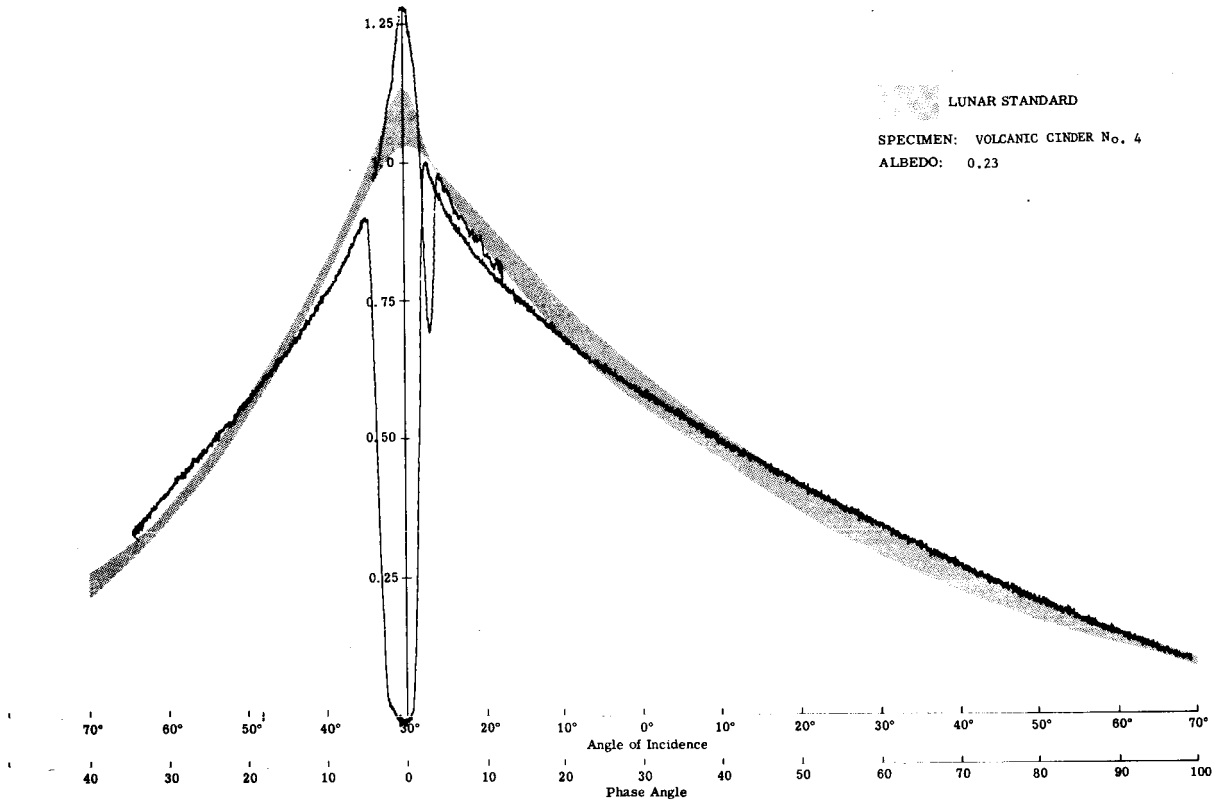
Visible



Blue

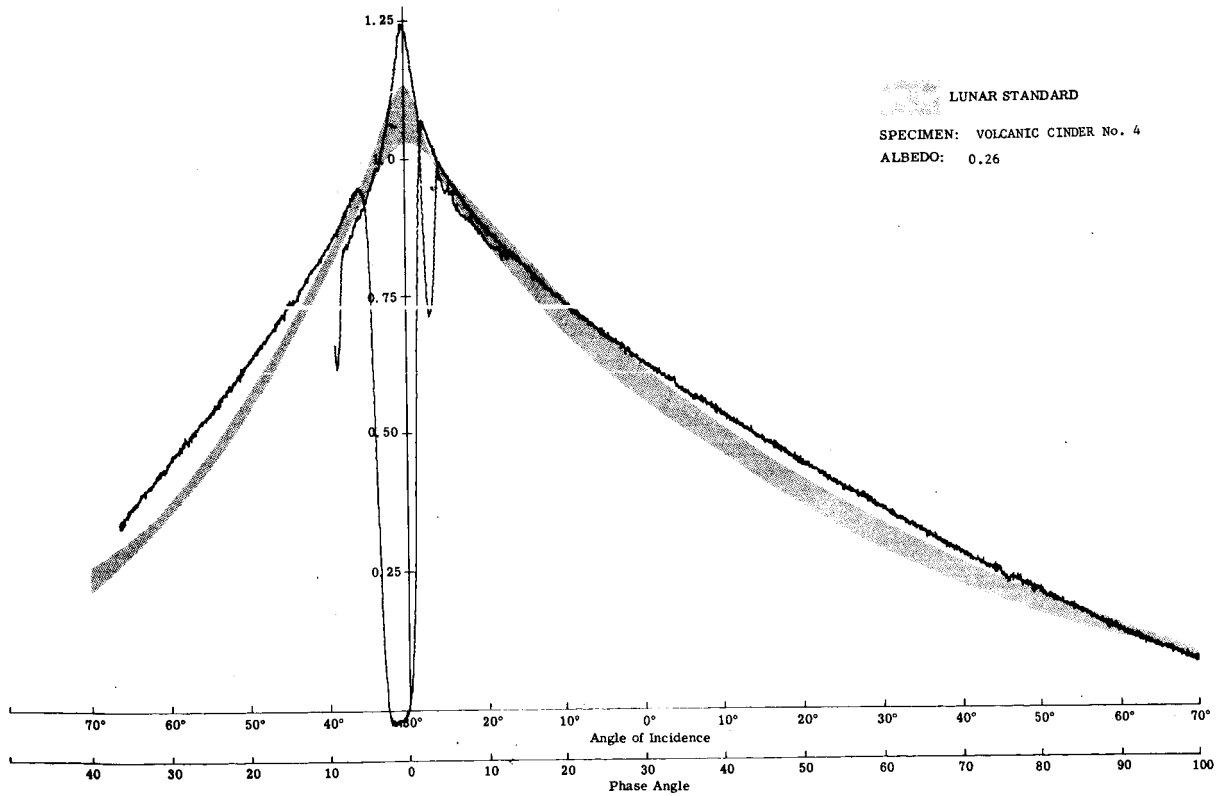
Fig. 6b Photometry of Volcanic Cinder No. 4 (E = 30°)

E = 30°



Red

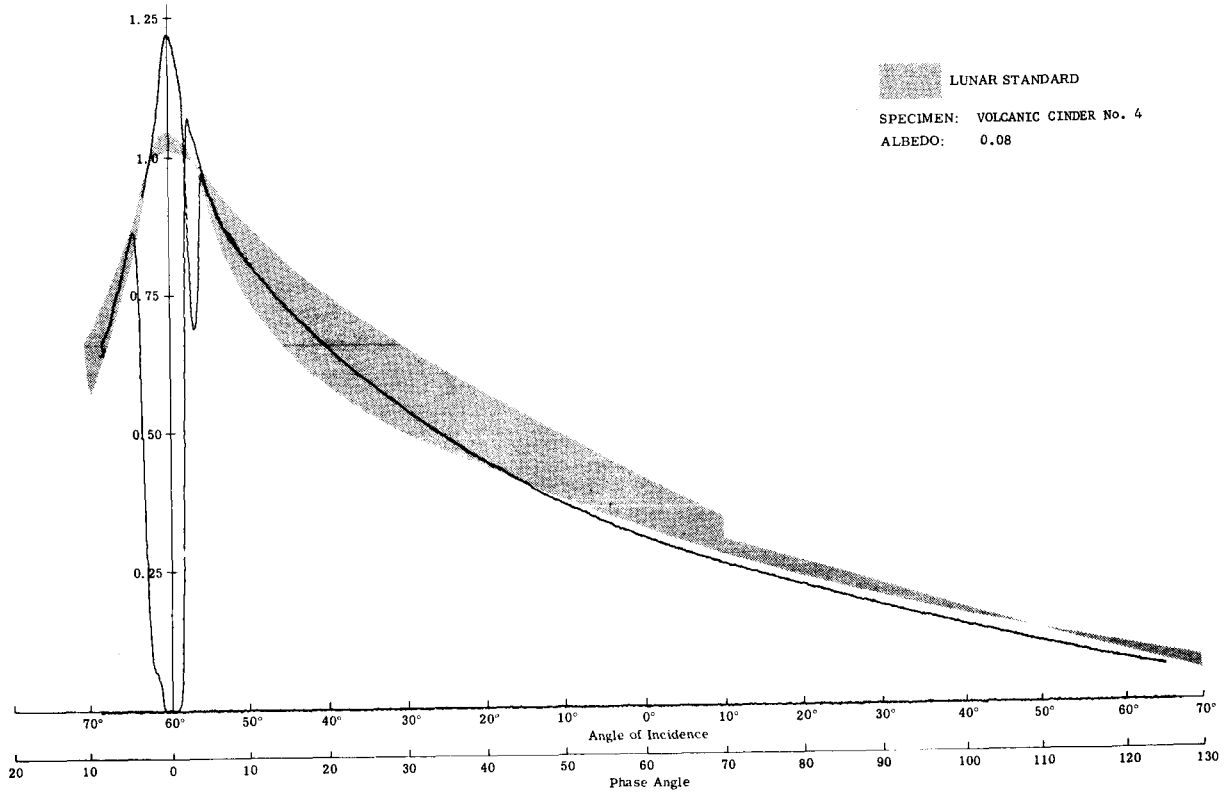
E = 30°



Infrared

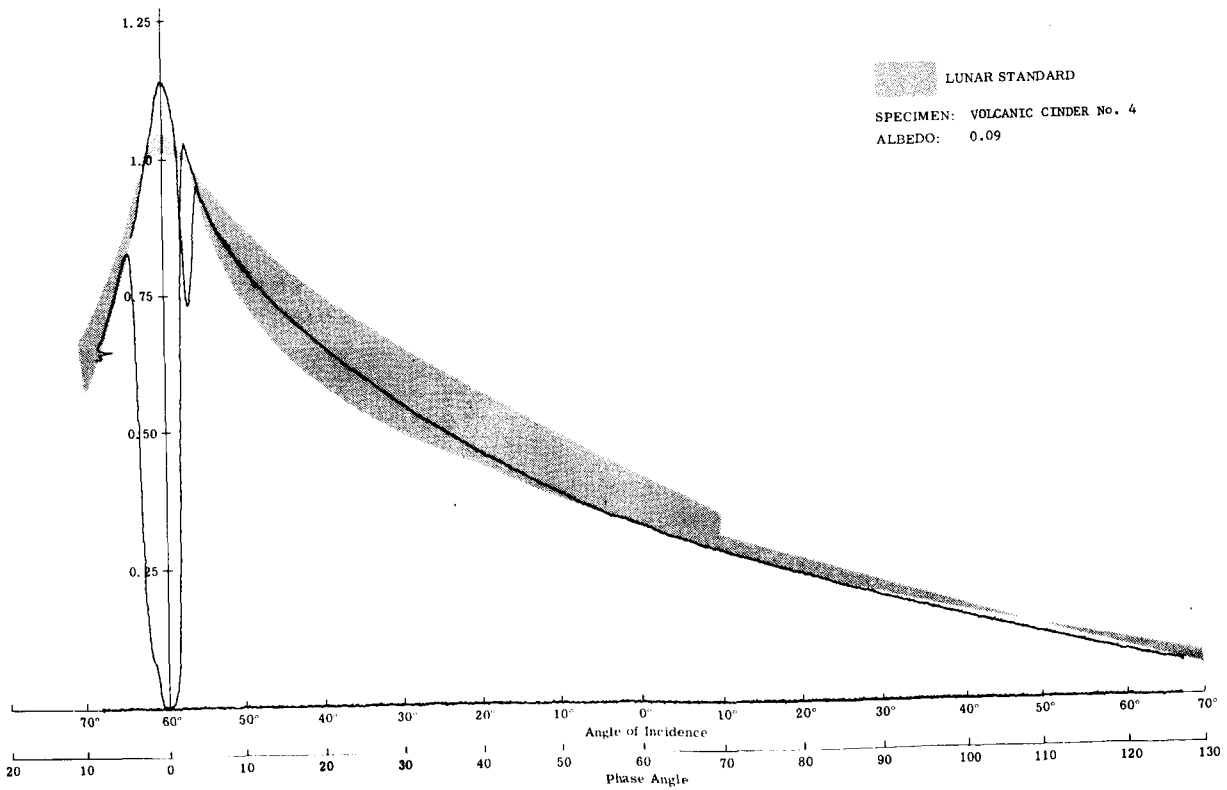
Fig. 6b (Cont) Photometry of Volcanic Cinder No. 4 (E = 30°)  
Research Dept  
RM-308  
January 1966

E = 60°



Visible

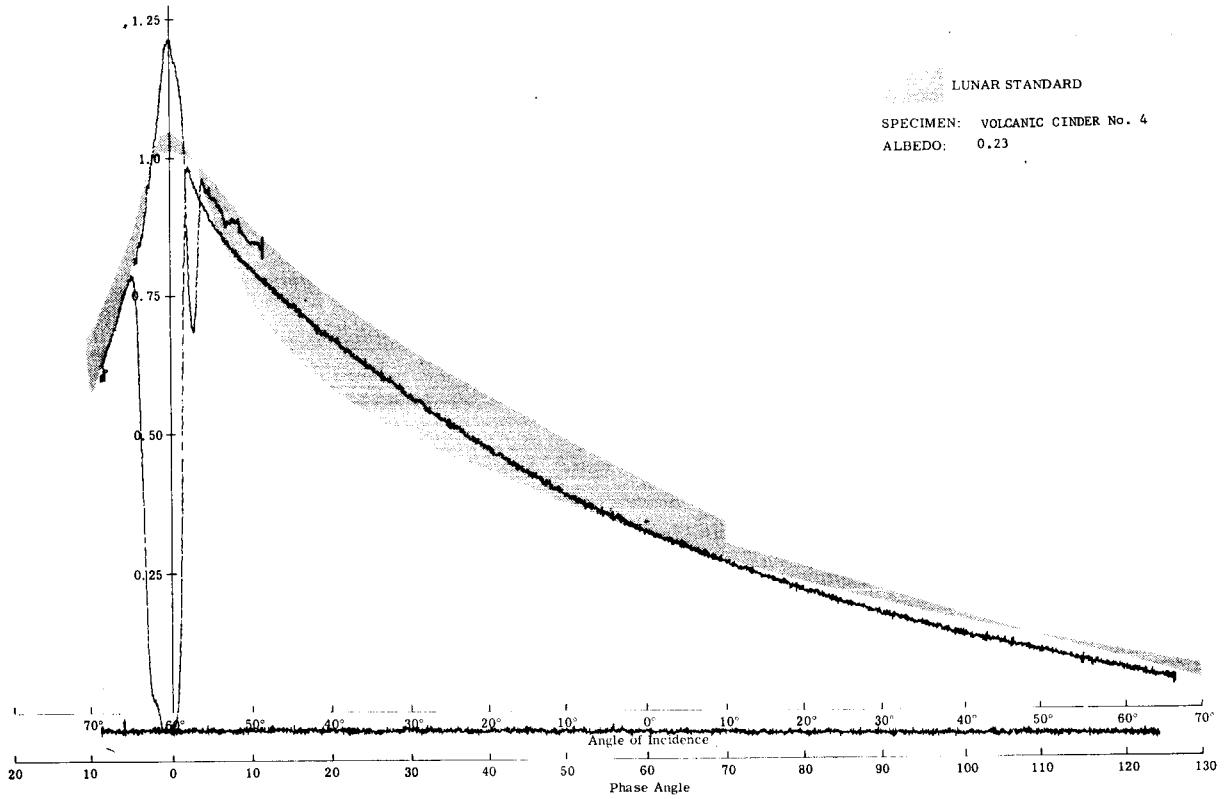
E = 60°



Blue

Fig. 6c Photometry of Volcanic Cinder No. 4 (E = 60°)

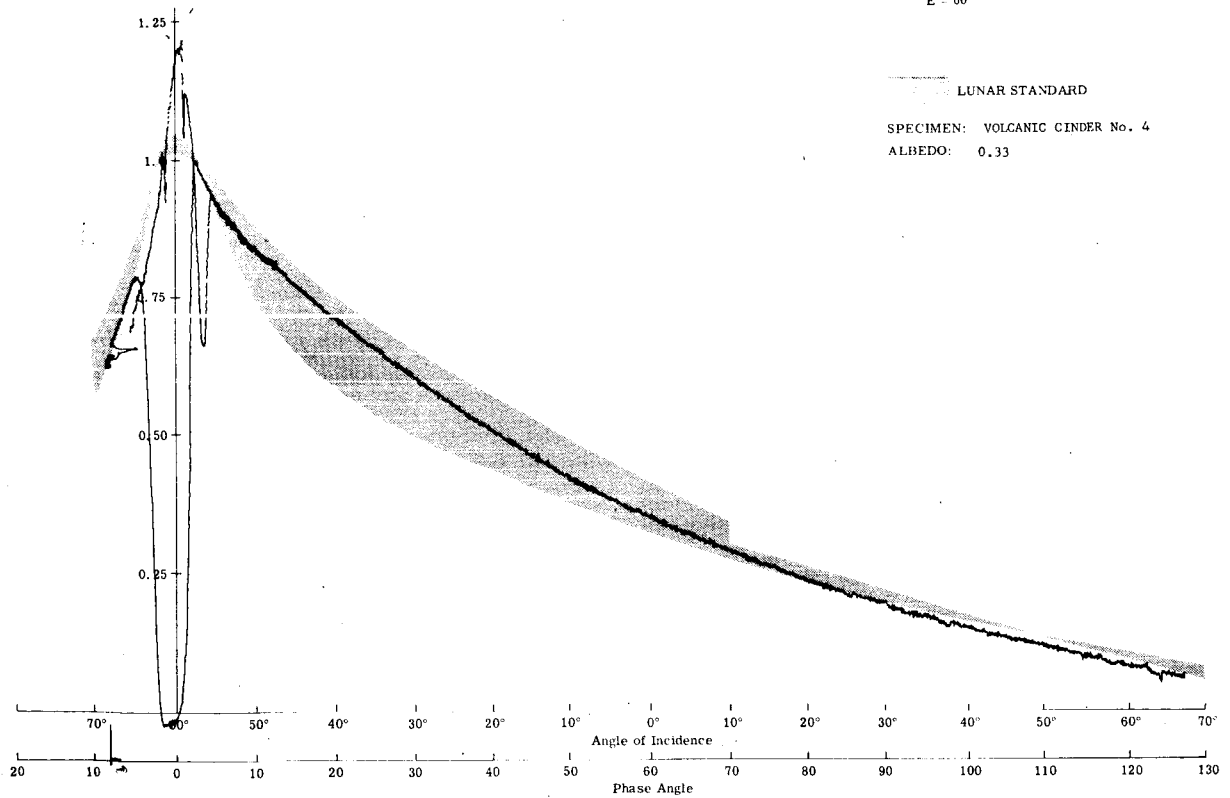
E 60°



LUNAR STANDARD  
SPECIMEN: VOLCANIC CINDER No. 4  
ALBEDO: 0.23

Red

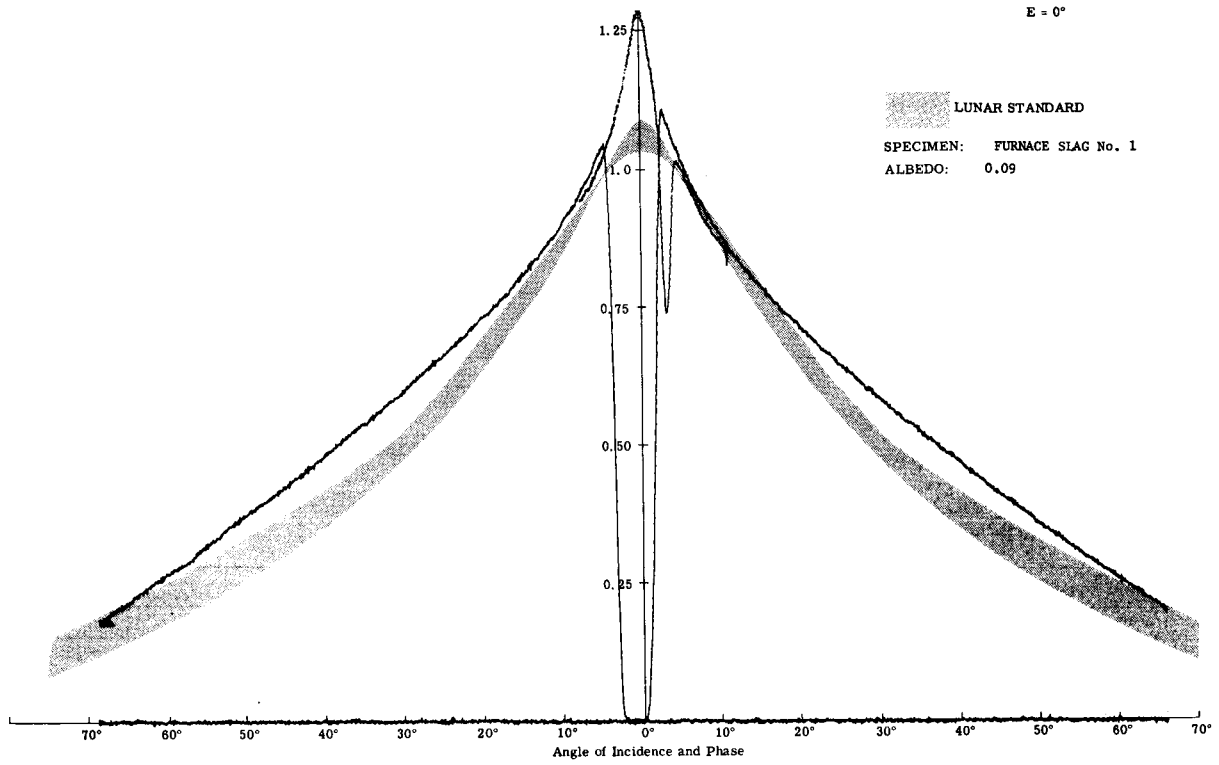
E = 60°



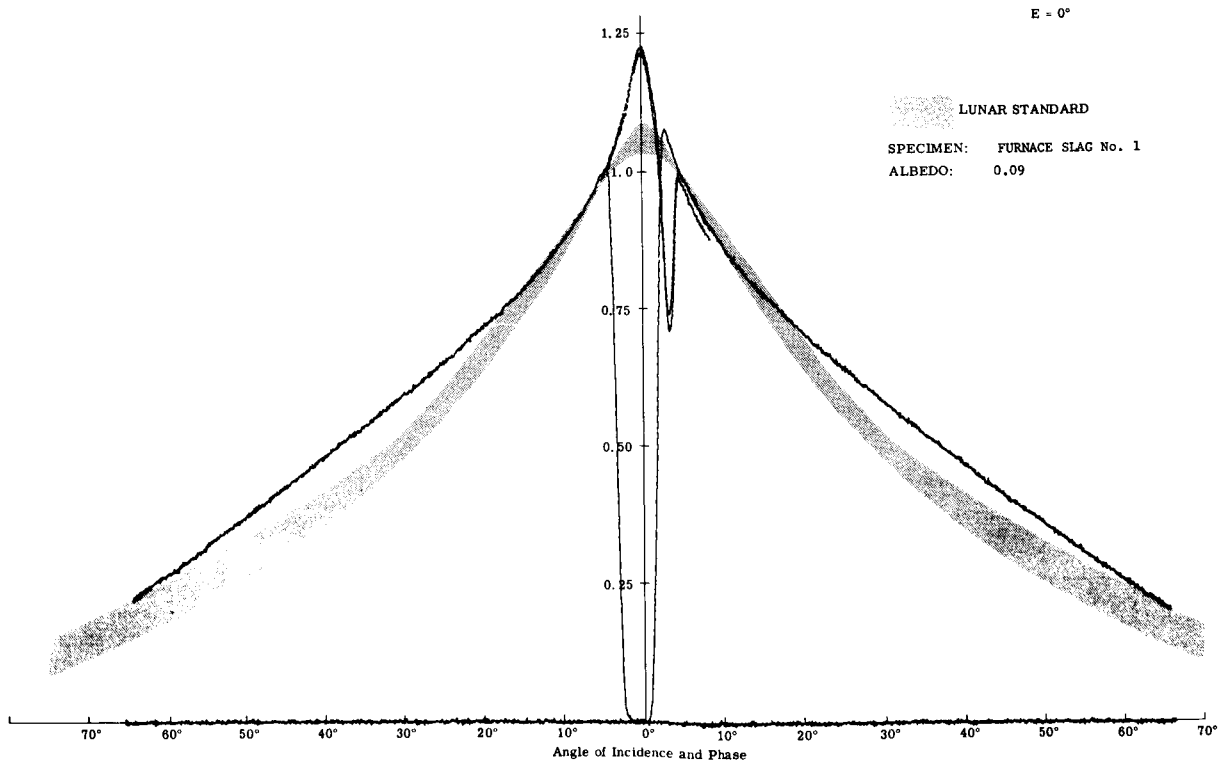
LUNAR STANDARD  
SPECIMEN: VOLCANIC CINDER No. 4  
ALBEDO: 0.33

Infrared

Fig. 6c (Cont) Photometry of Volcanic Cinder No. 4 (E = 60°)

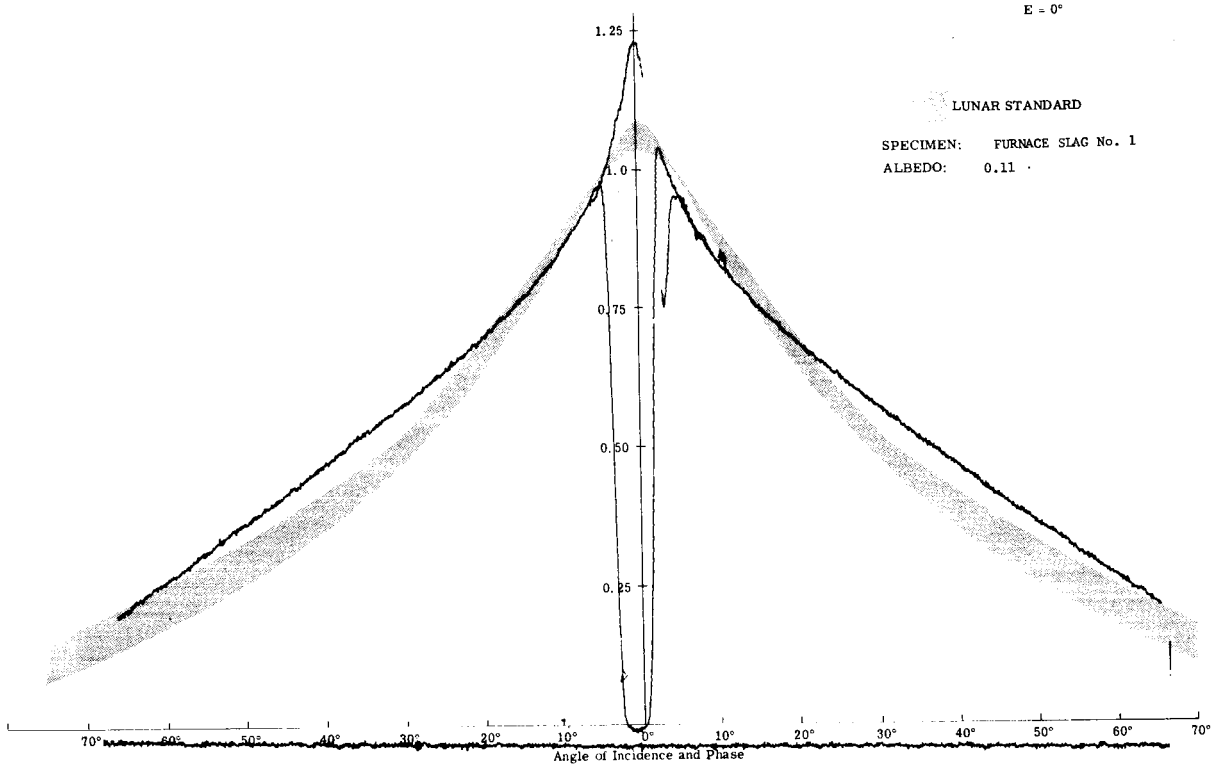


Visible

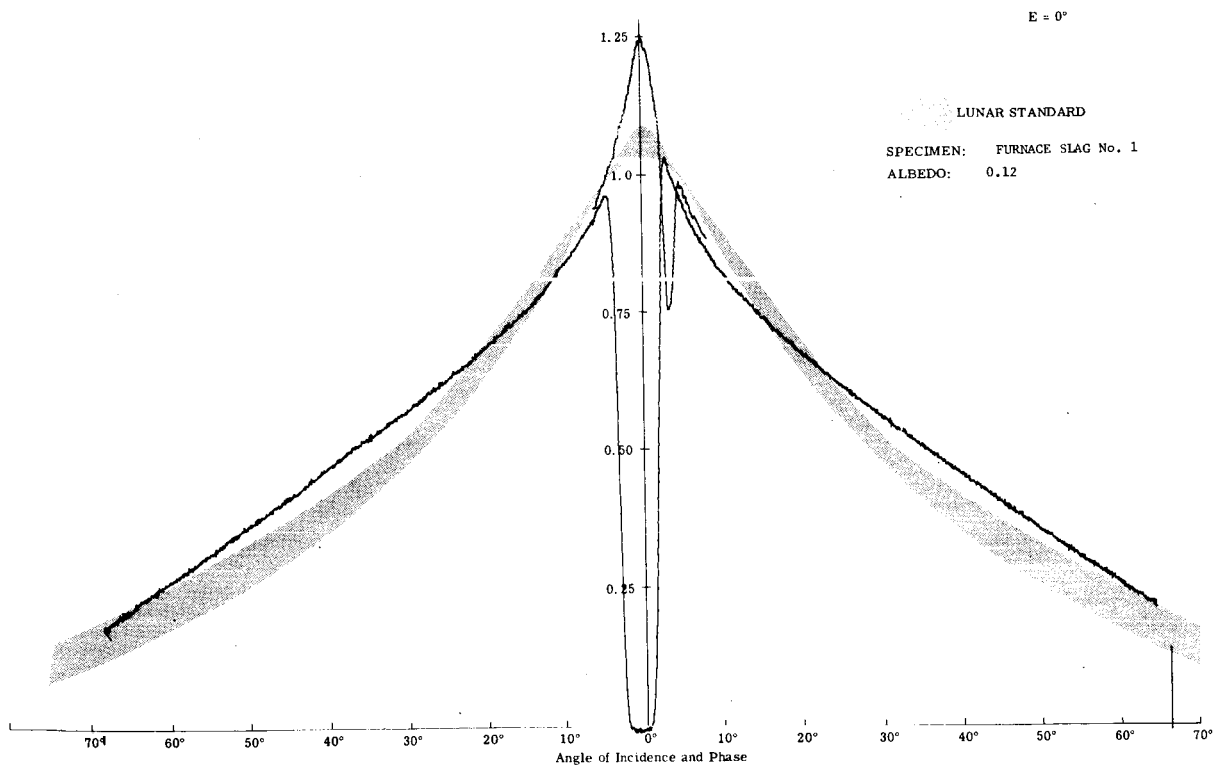


Blue

Fig. 7a Photometry of Furnace Slag No. 1 (E = 0°)



Red

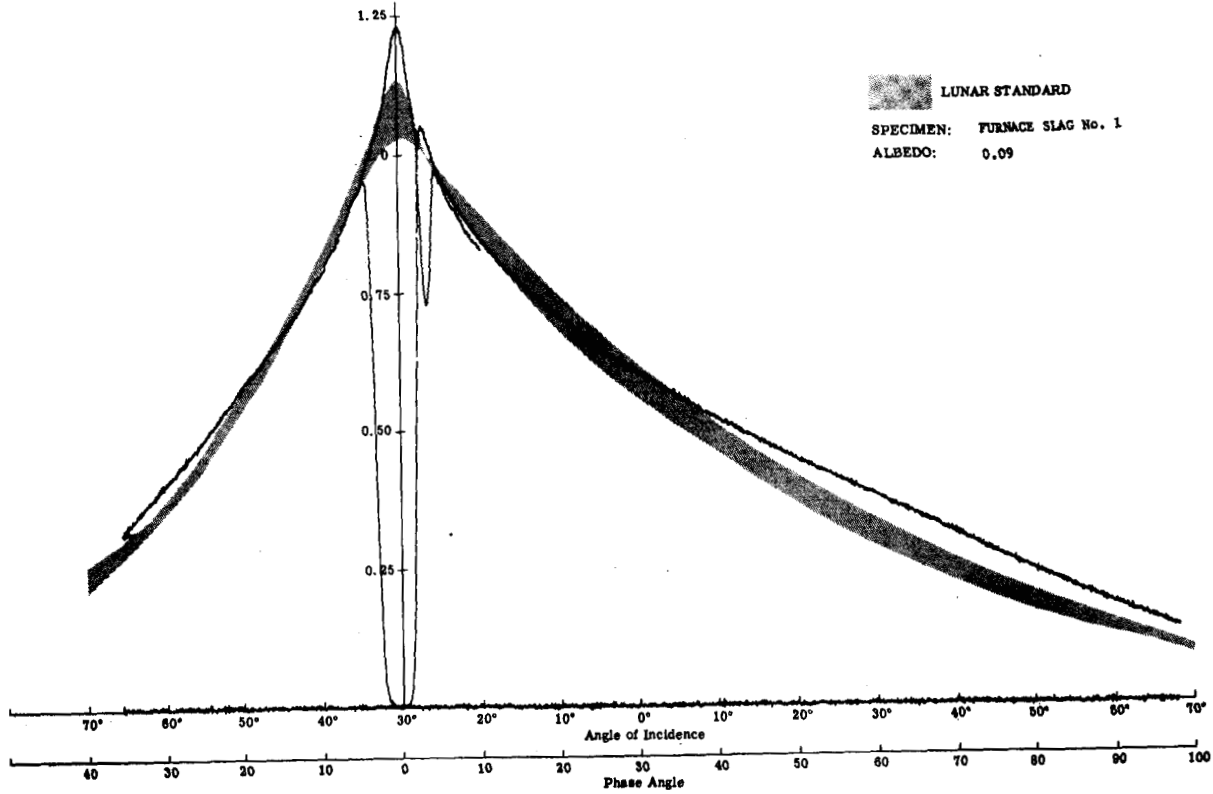


Infrared

Fig. 7a (Cont) Photometry of Furnace Slag No. 1 (E = 0°)  
 Research Dept  
 RM-308  
 January 1966

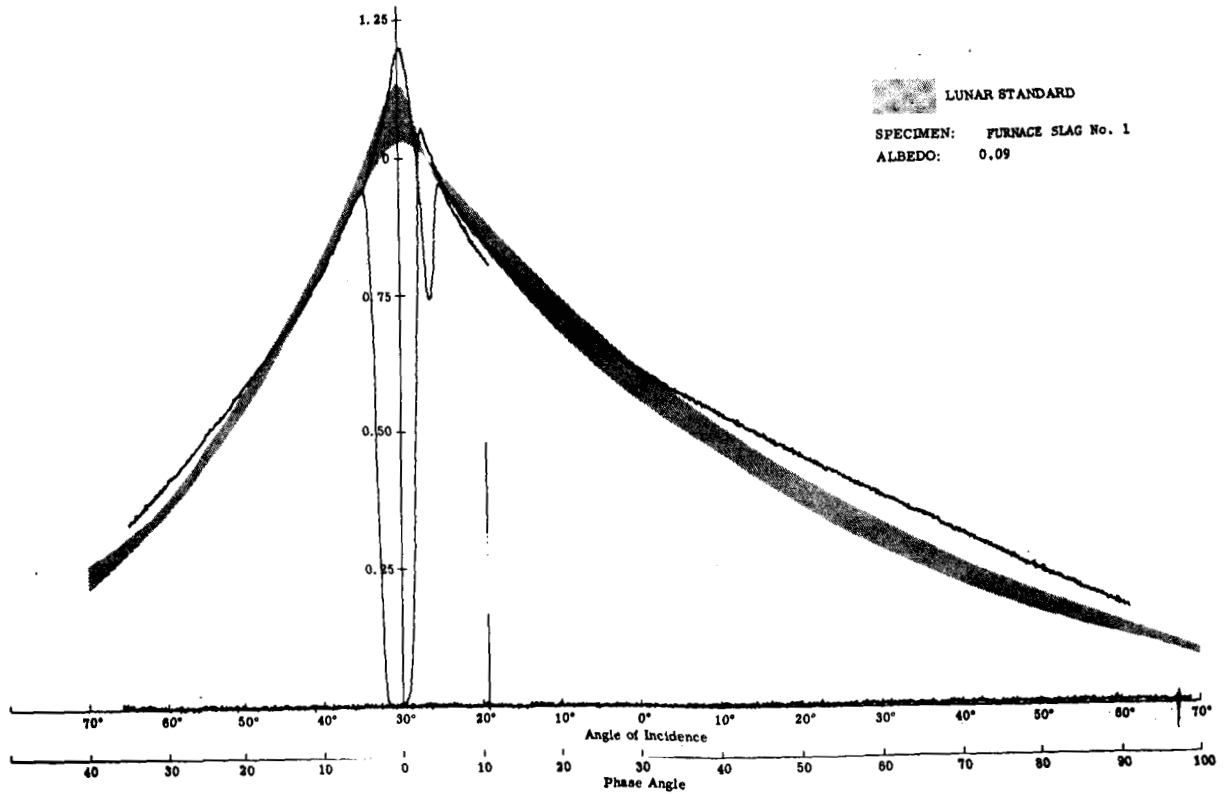


E = 30°



Visible

E = 30°



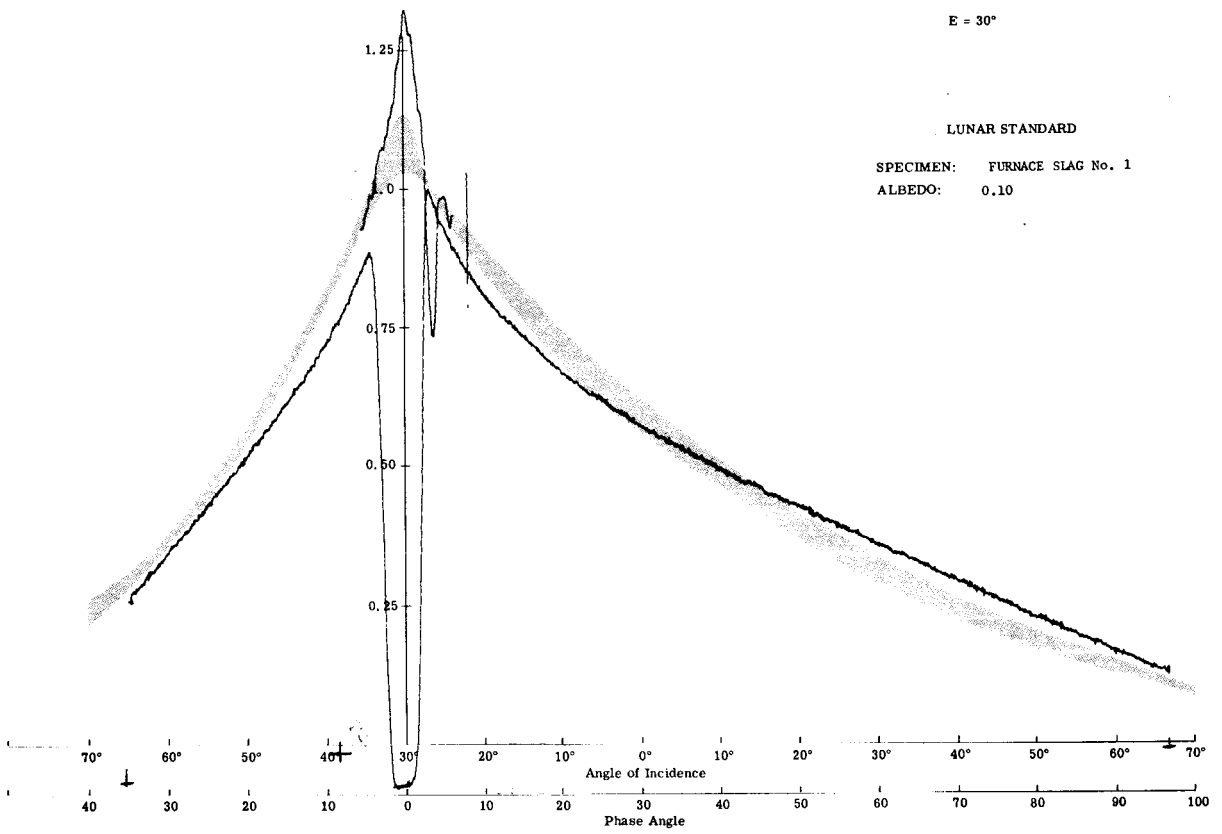
Blue

Fig. 7b Photometry of Furnace Slag No. 1 (E = 30°)

E = 30°

LUNAR STANDARD

SPECIMEN: FURNACE SLAG No. 1  
ALBEDO: 0.10

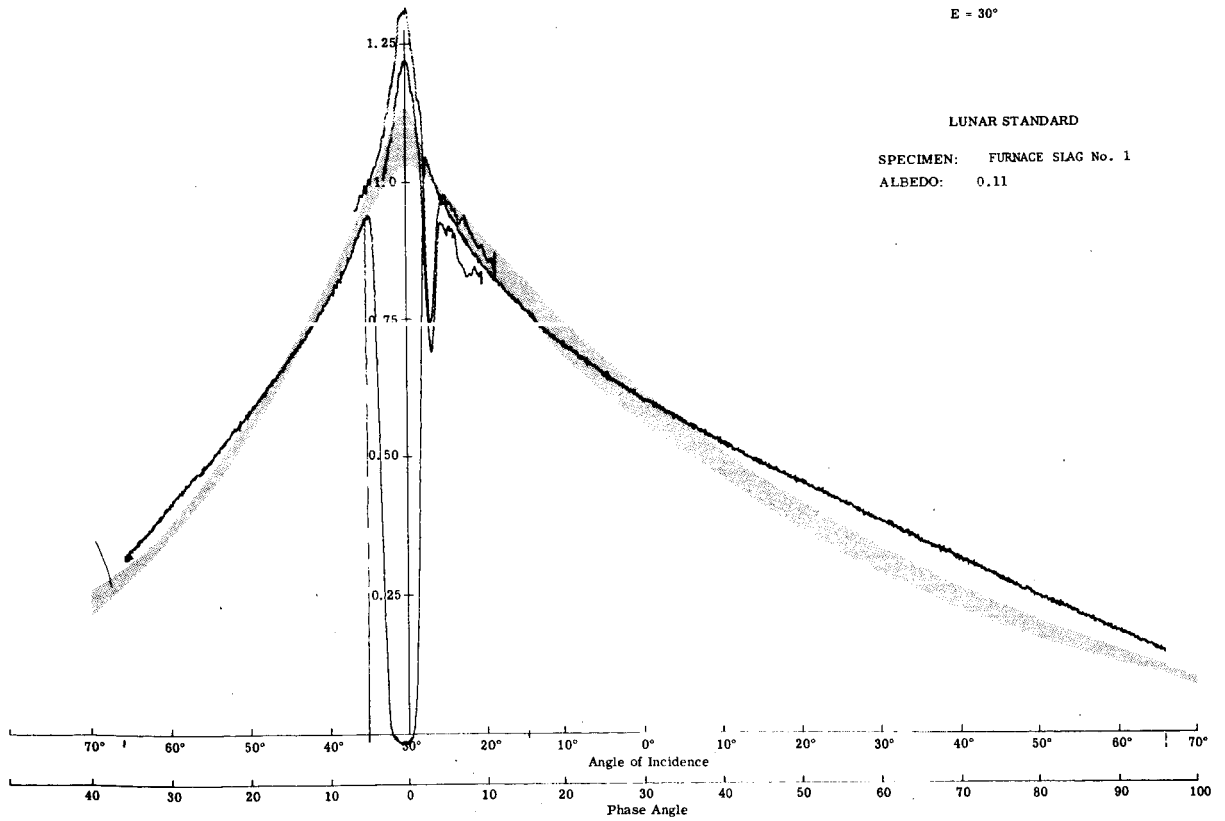


Red

E = 30°

LUNAR STANDARD

SPECIMEN: FURNACE SLAG No. 1  
ALBEDO: 0.11

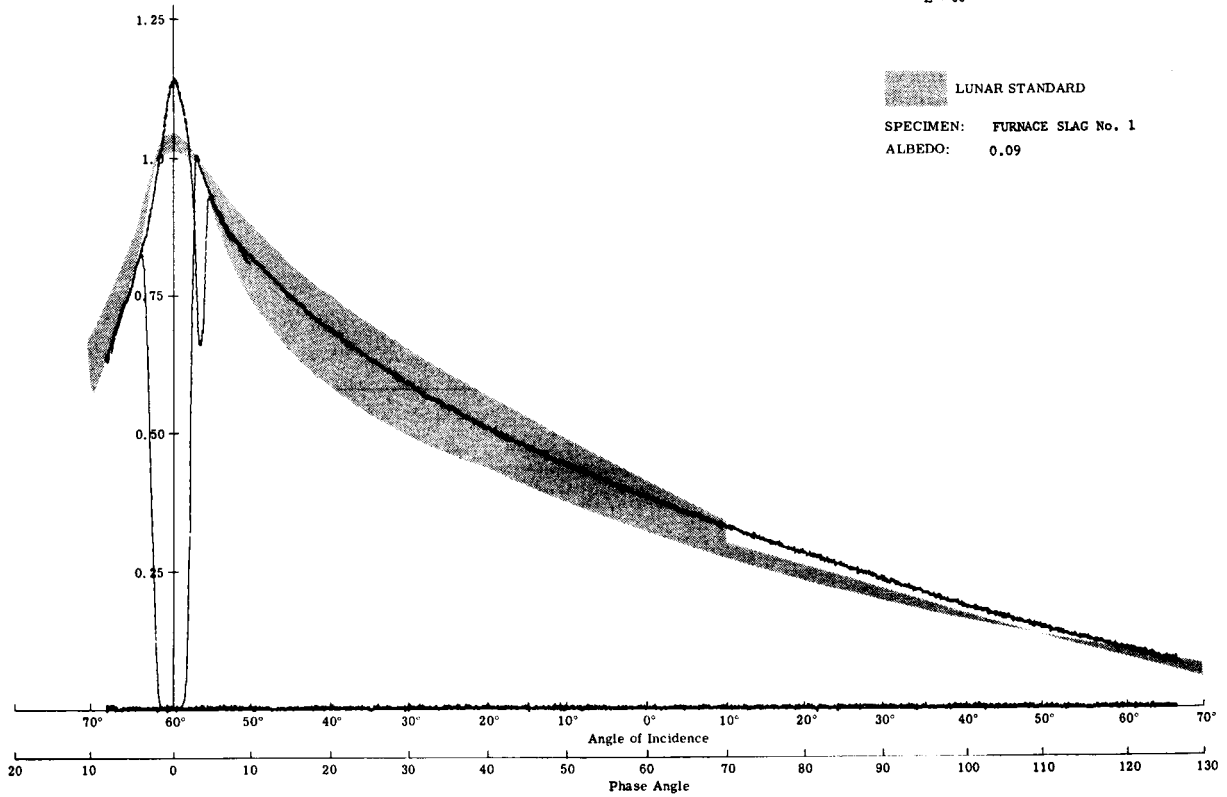


Infrared

Fig. 7b (Cont) Photometry of Furnace slag No. 1 (E = 30°)

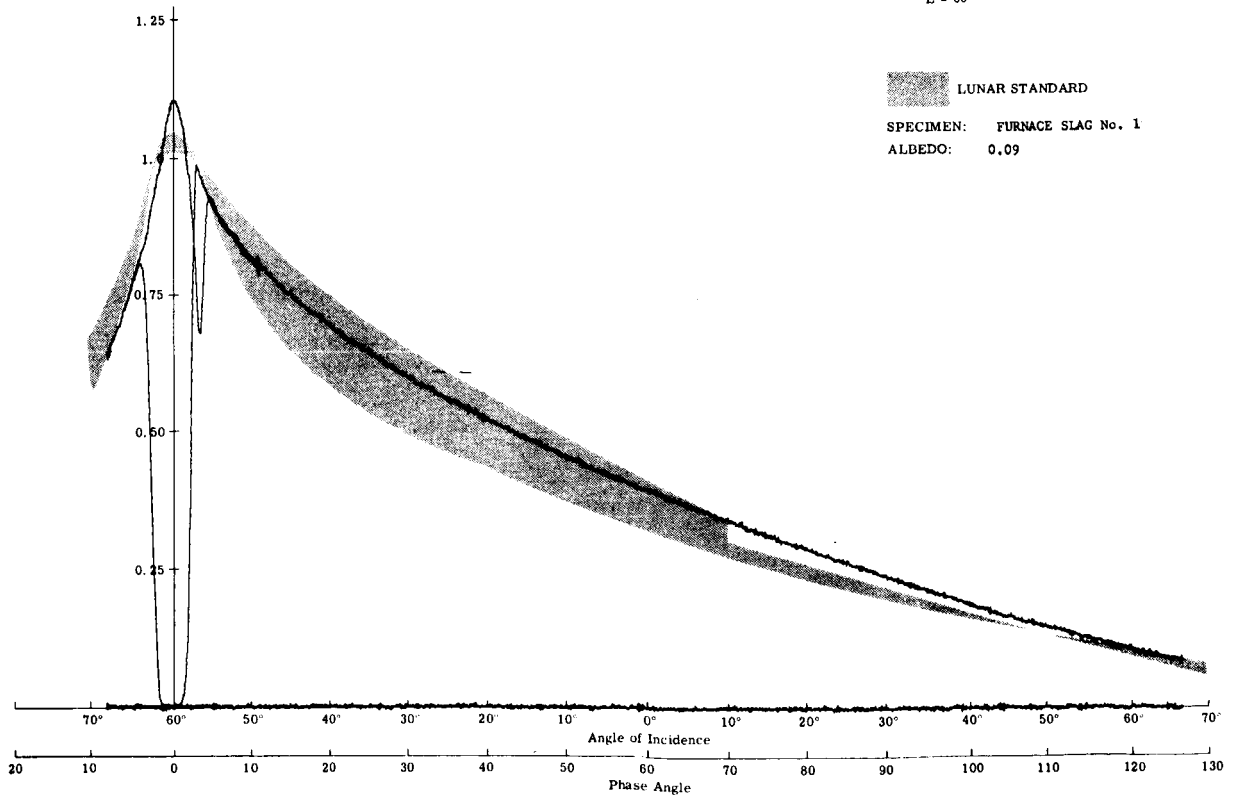
Research Dept  
RM-308  
January 1966

E = 60°



Visible

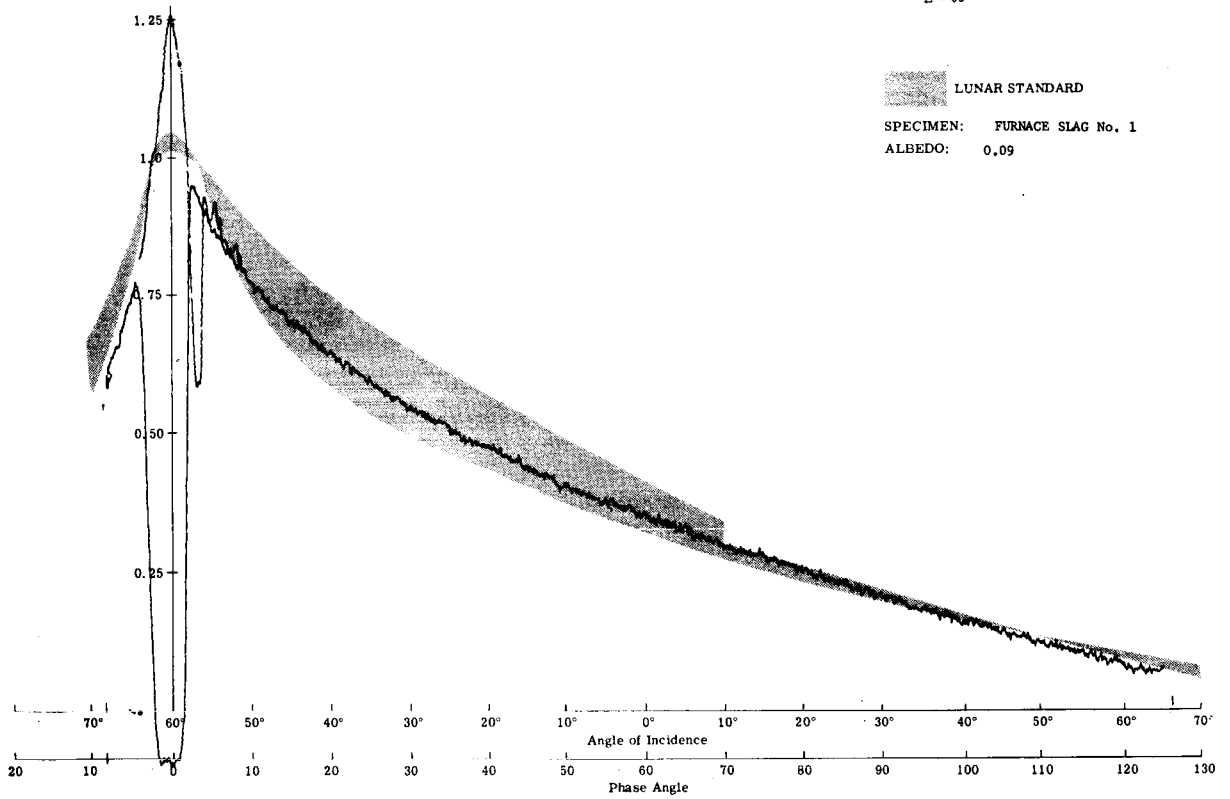
E = 60°



Blue

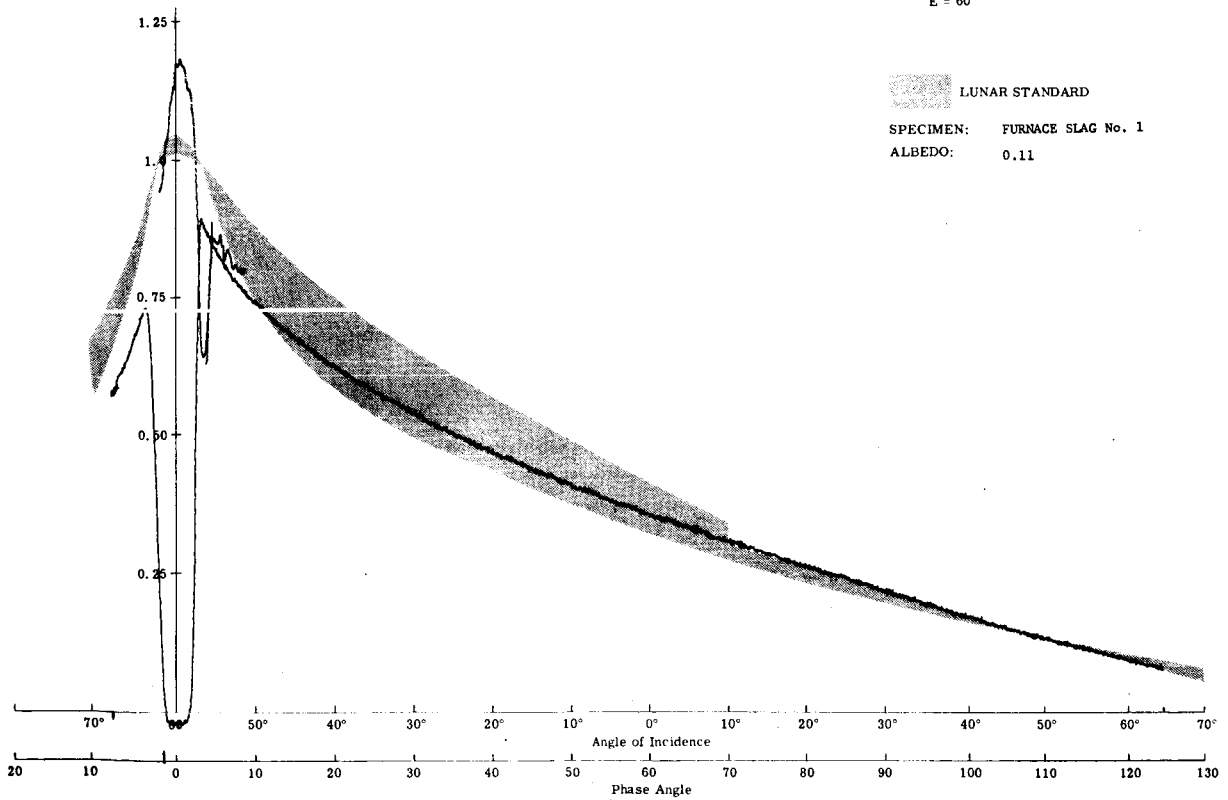
Fig. 7c Photometry of Furnace Slag No. 1 (E = 60°)

E = 60°



Red

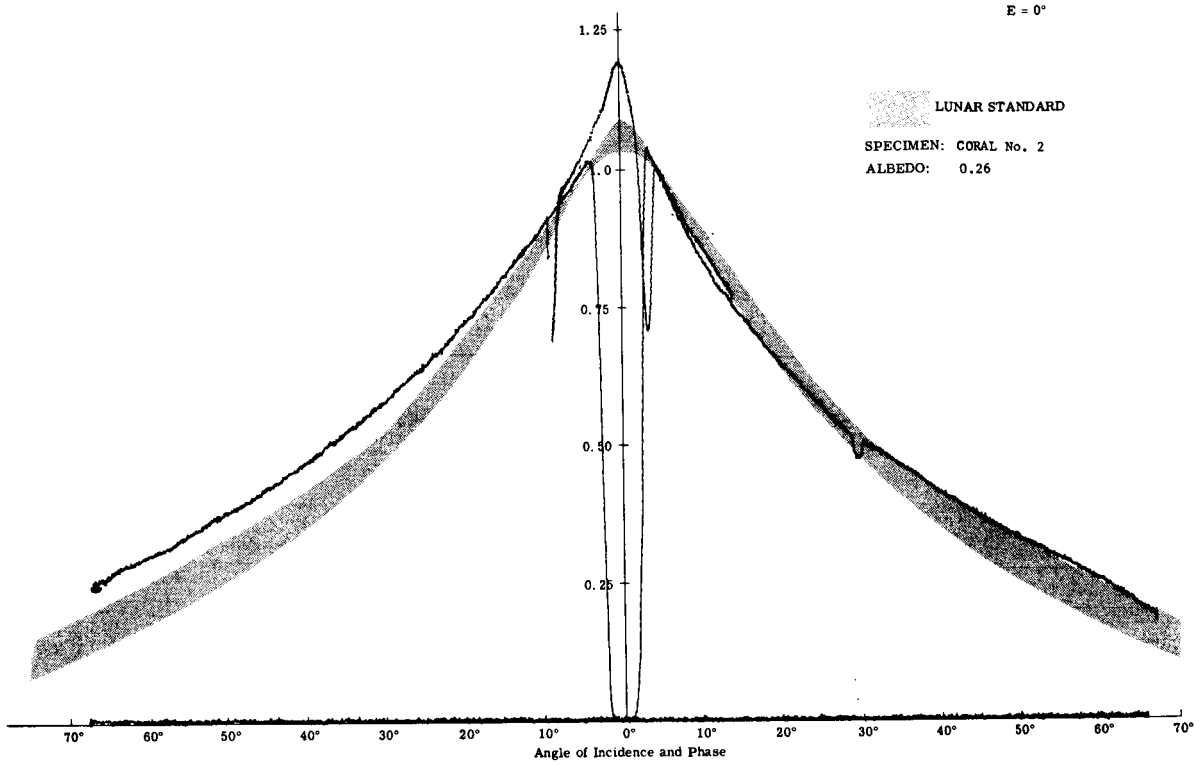
E = 60°



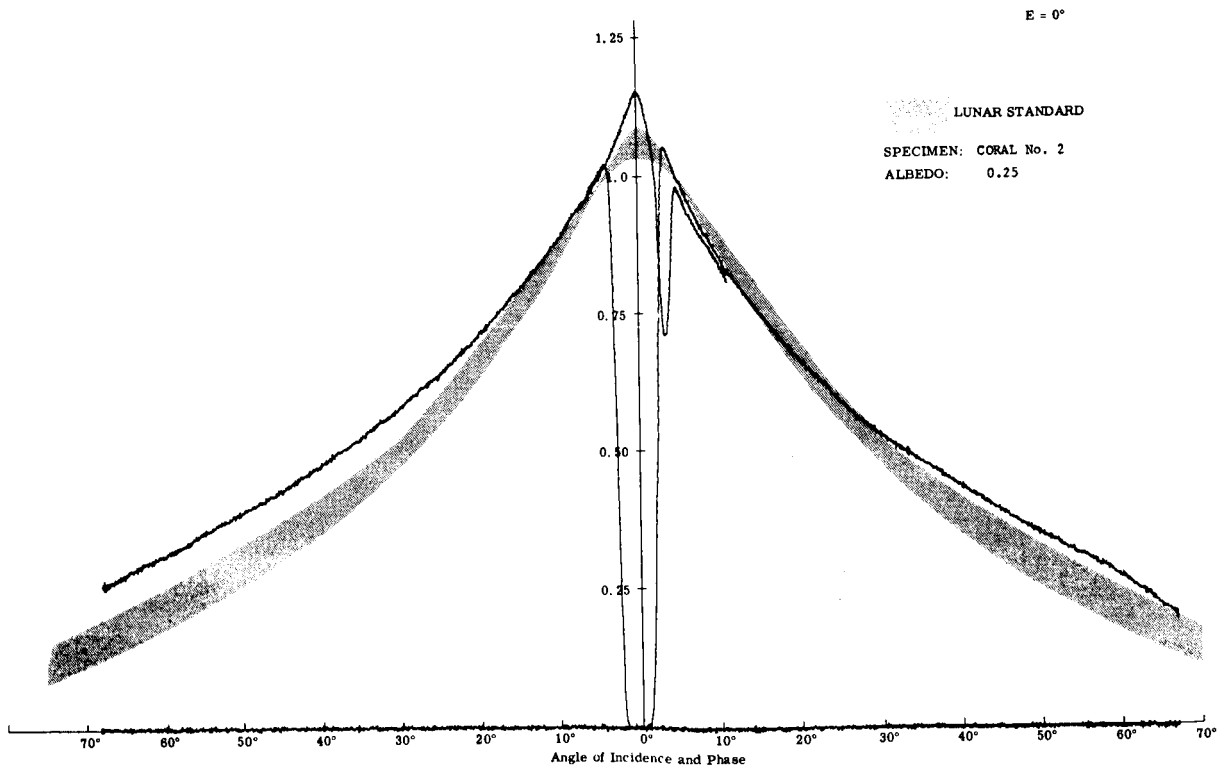
Infrared

Fig. 7c (Cont) Photometry of Furnace Slag No. 1 (E = 60°)

Research Dept  
RM-308  
January 1966

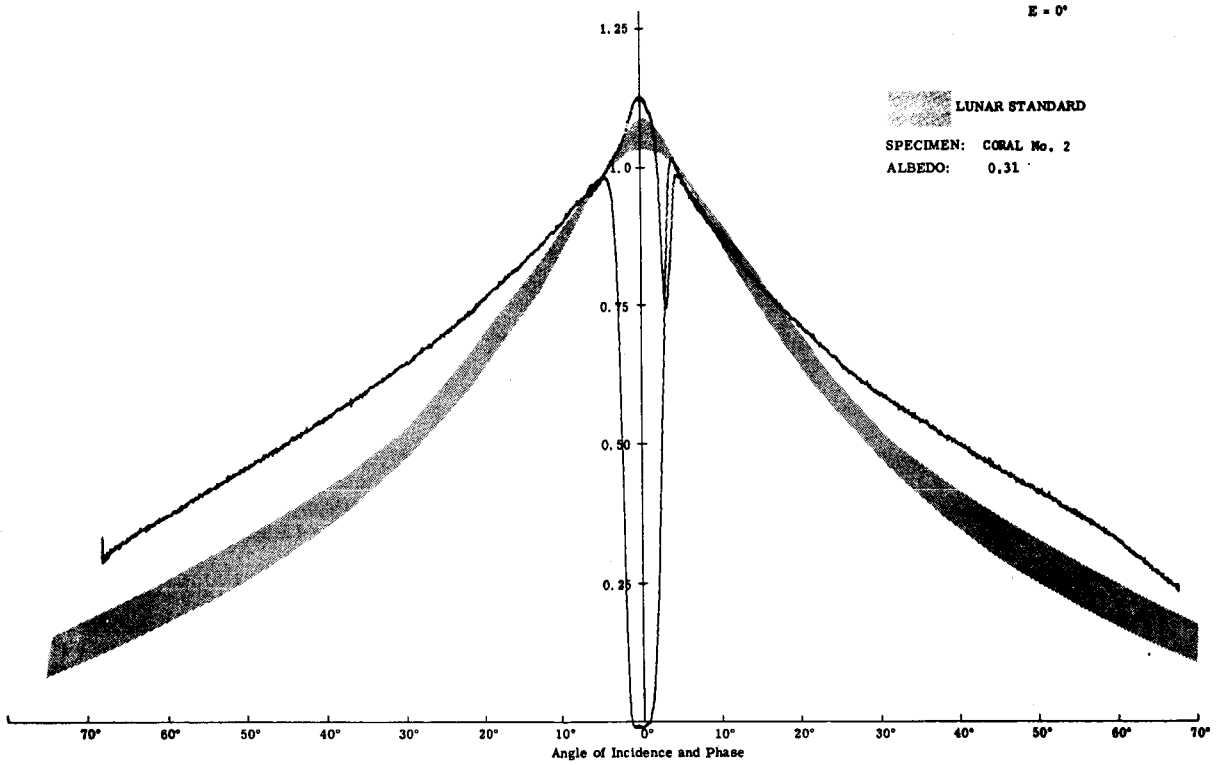


Visible

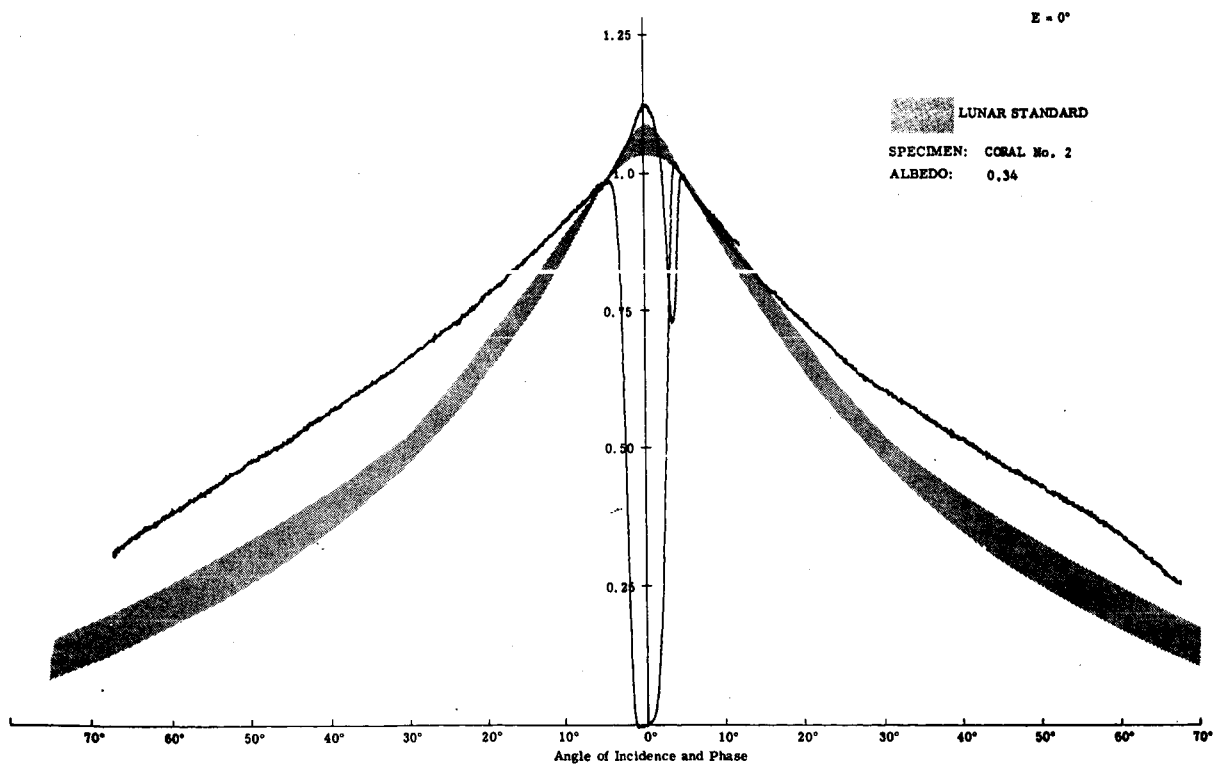


Blue

Fig. 8a Photometry of Coral No. 2 (E = 0°)



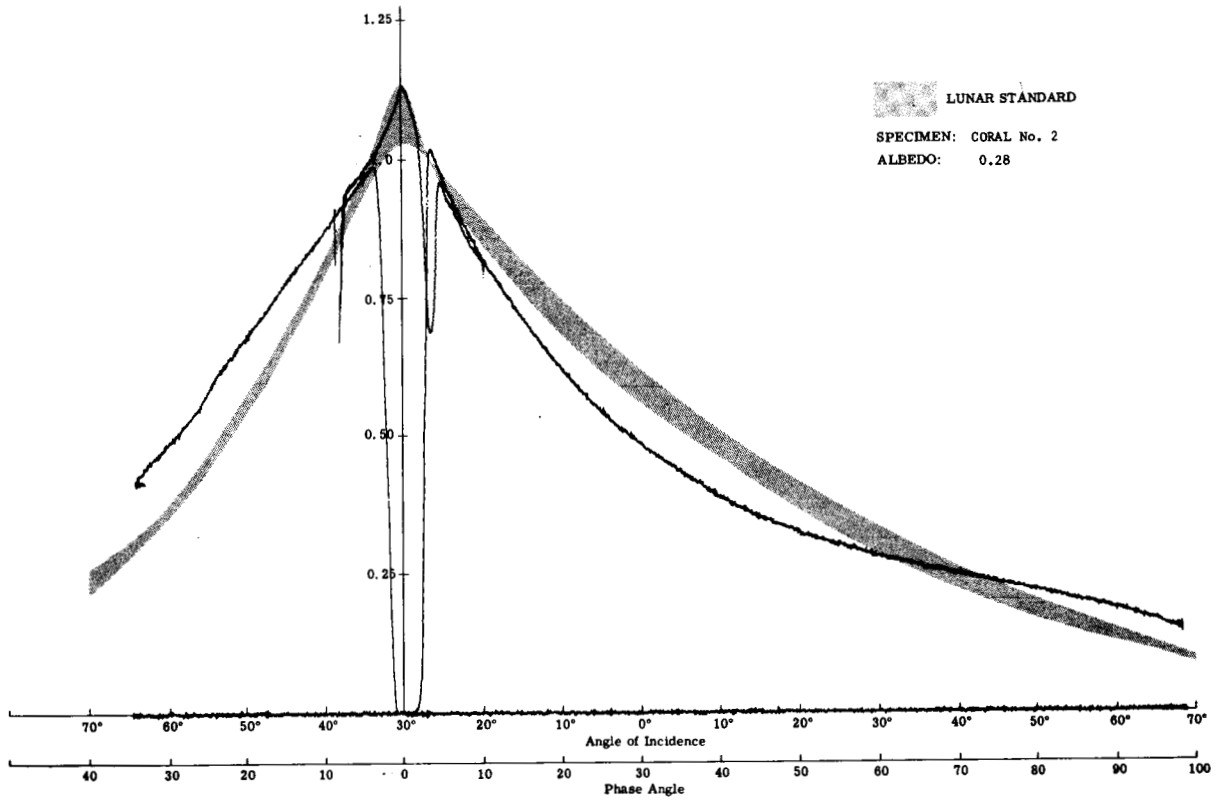
Red



Infrared

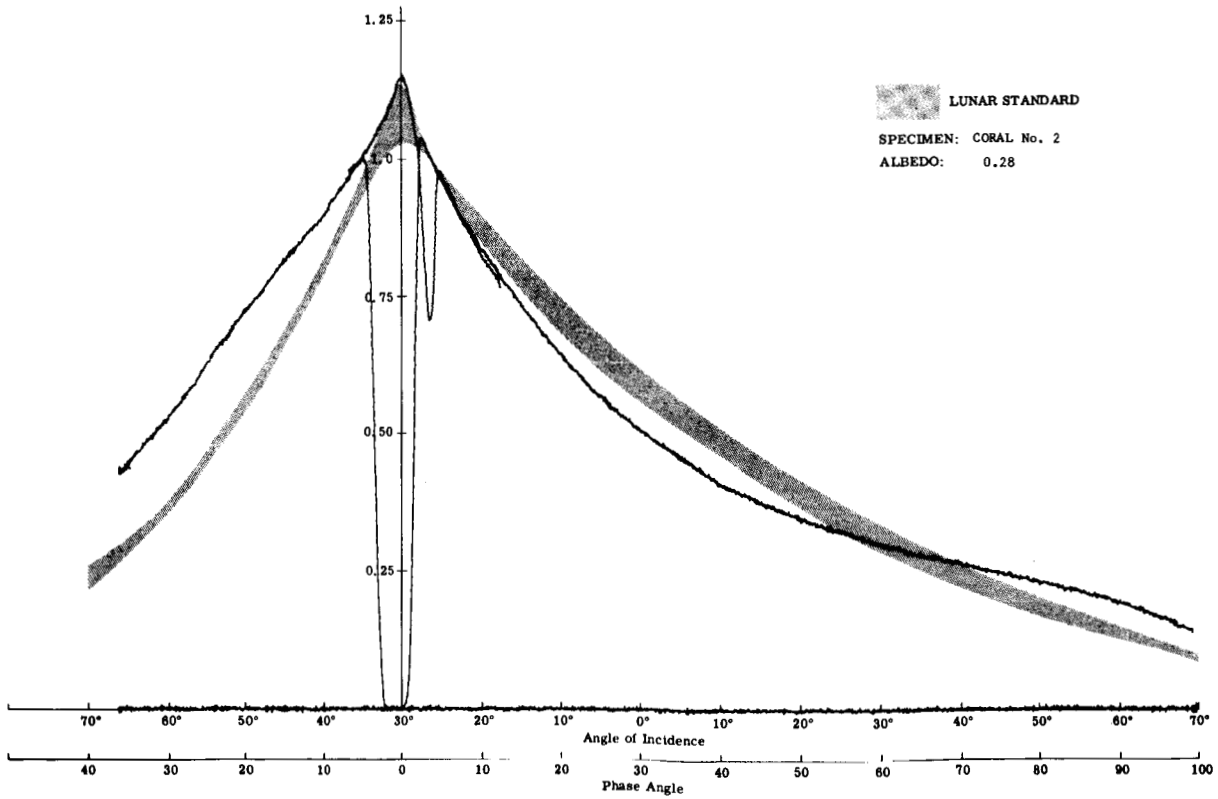
Fig. 8a (Cont) Photometry of Coral No. 2 (E = 0°)

E = 30°



Visible

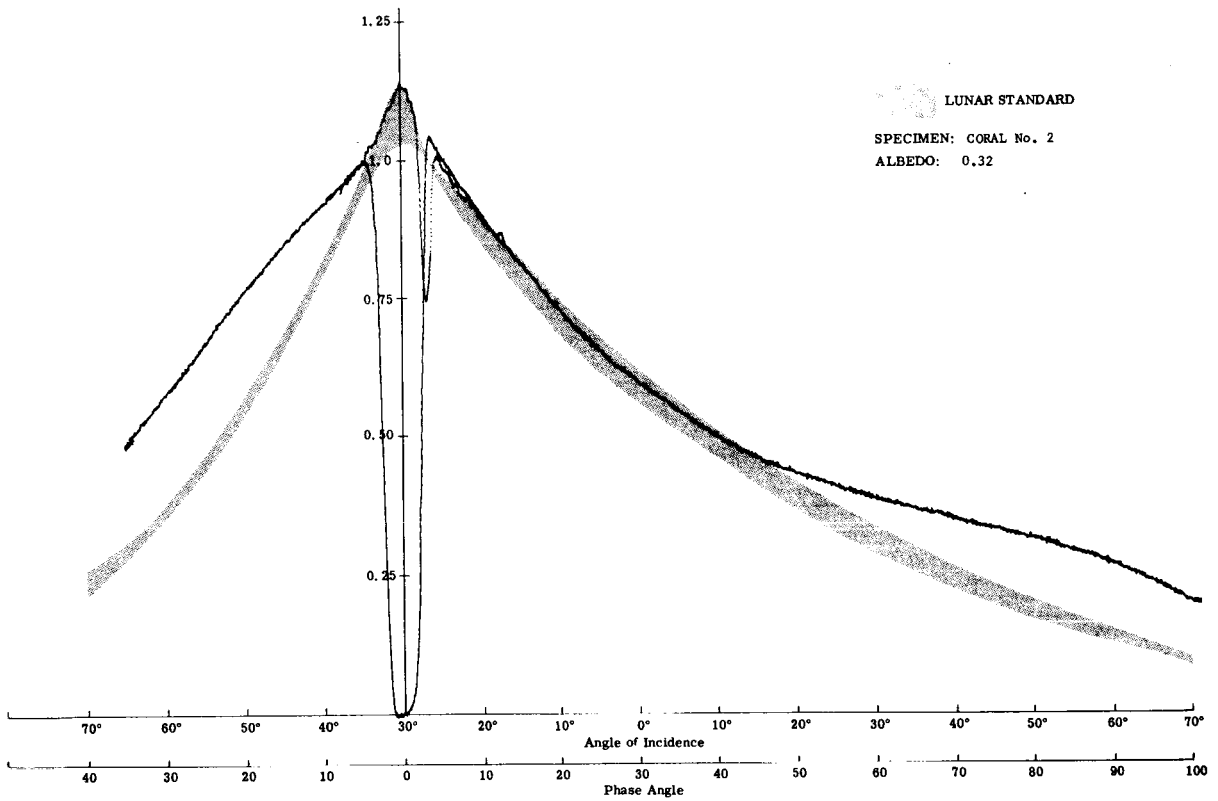
E = 30°



Blue

Fig. 8b Photometry of Coral No. 2 (E = 30°)

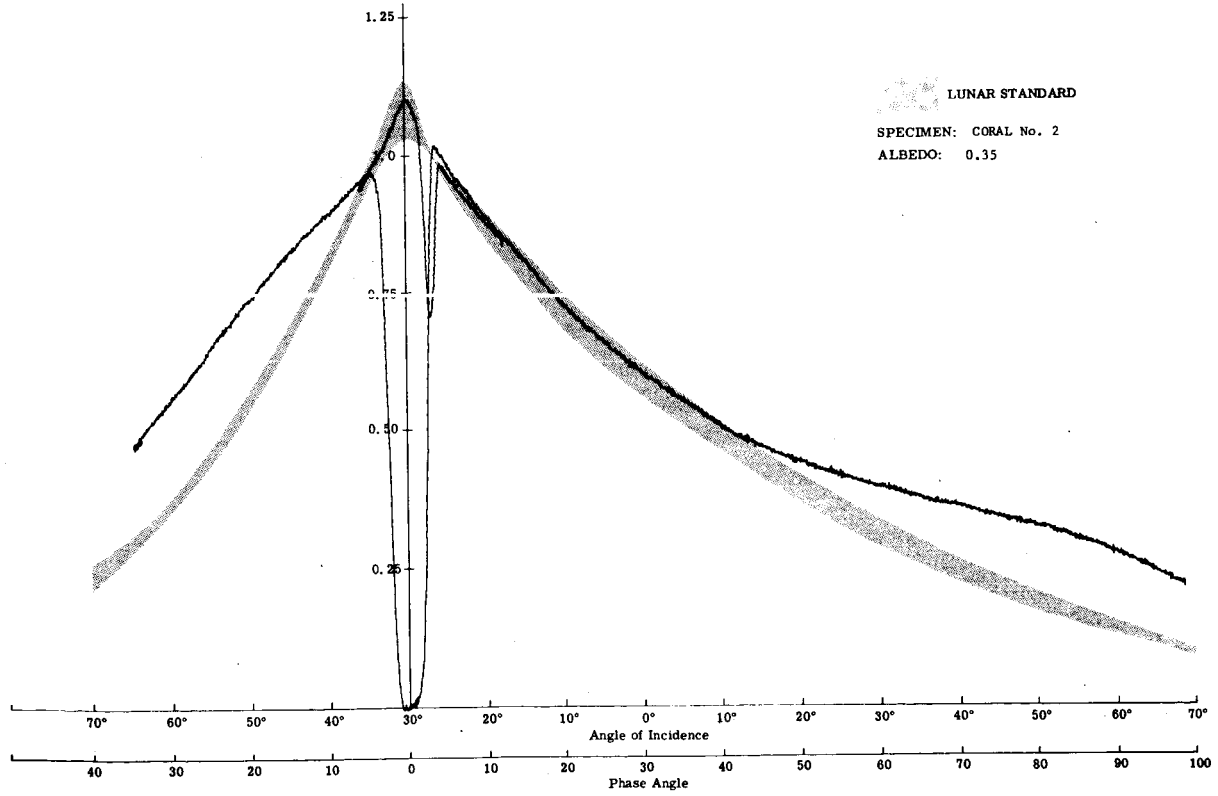
E = 30°



LUNAR STANDARD  
SPECIMEN: CORAL No. 2  
ALBEDO: 0.32

Red

E = 30°



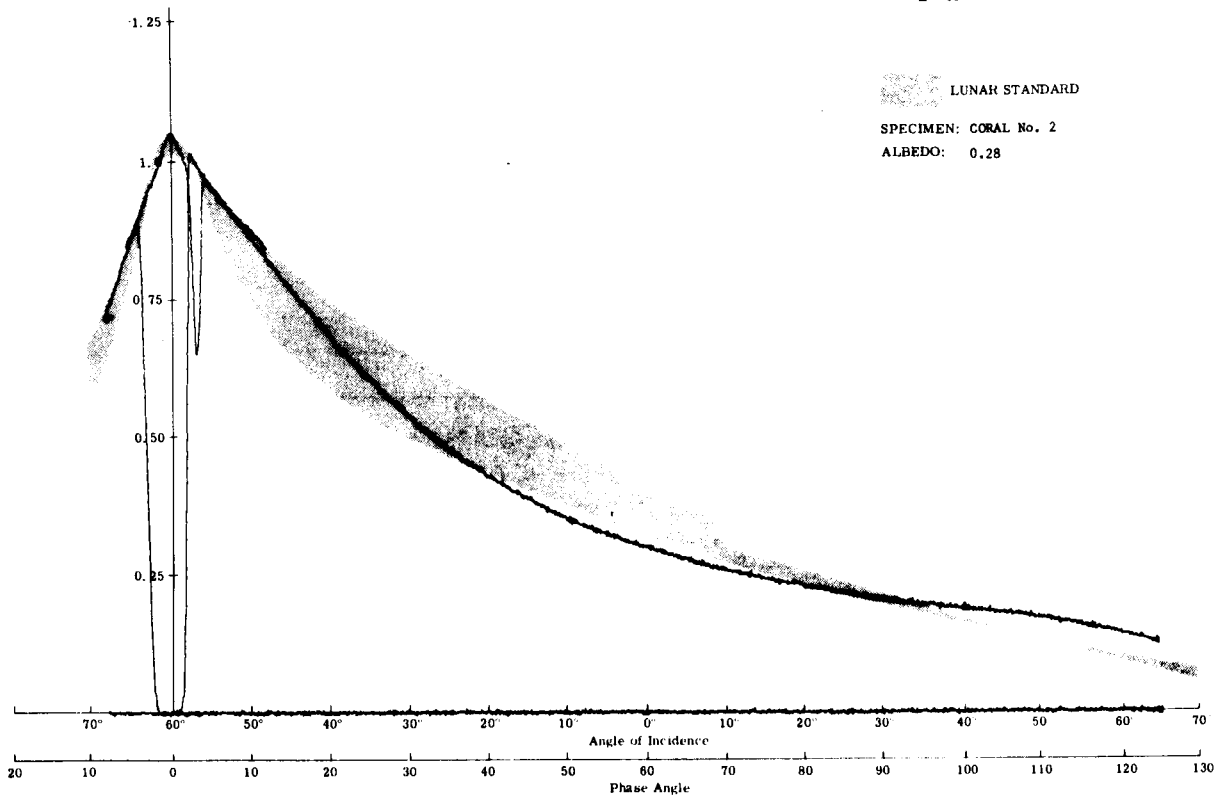
LUNAR STANDARD  
SPECIMEN: CORAL No. 2  
ALBEDO: 0.35

Infrared

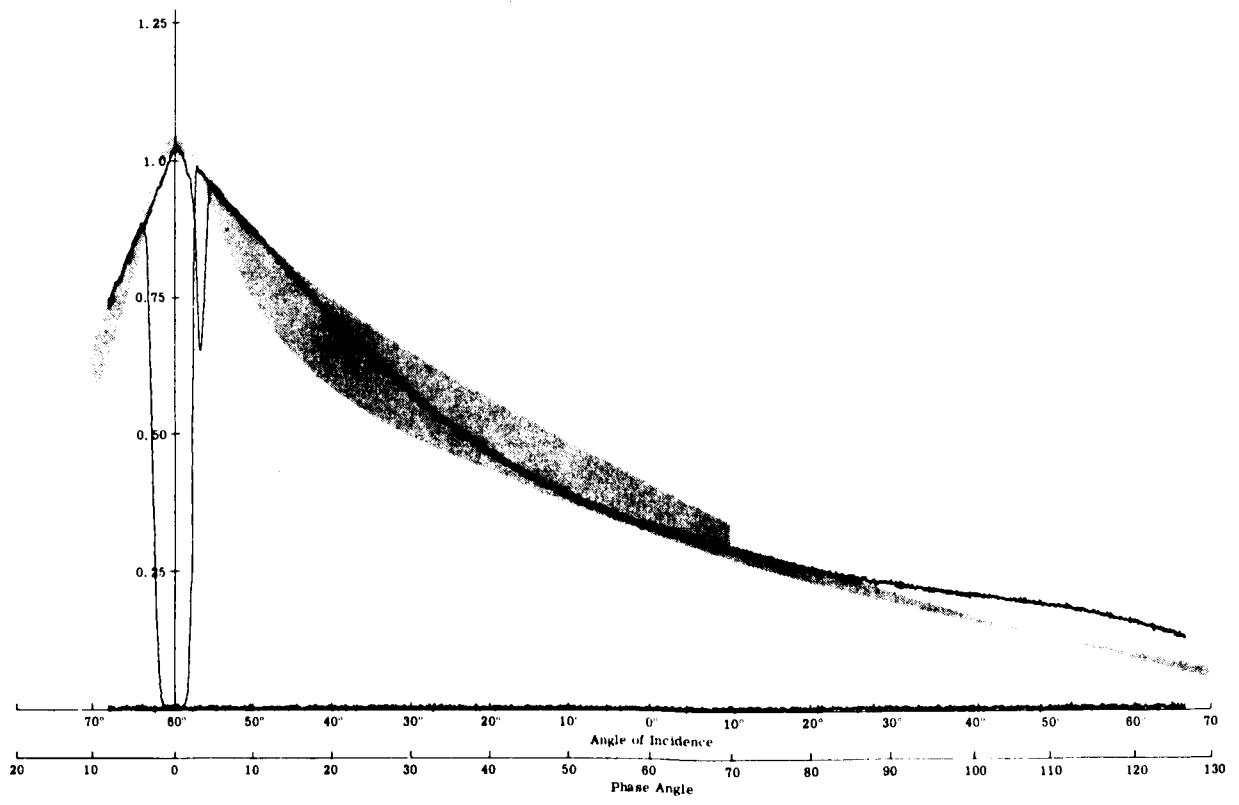
Fig. 8b (Cont) Photometry of Coral No. 2 (E = 30°)

Research Dept  
RM-308  
January 1966





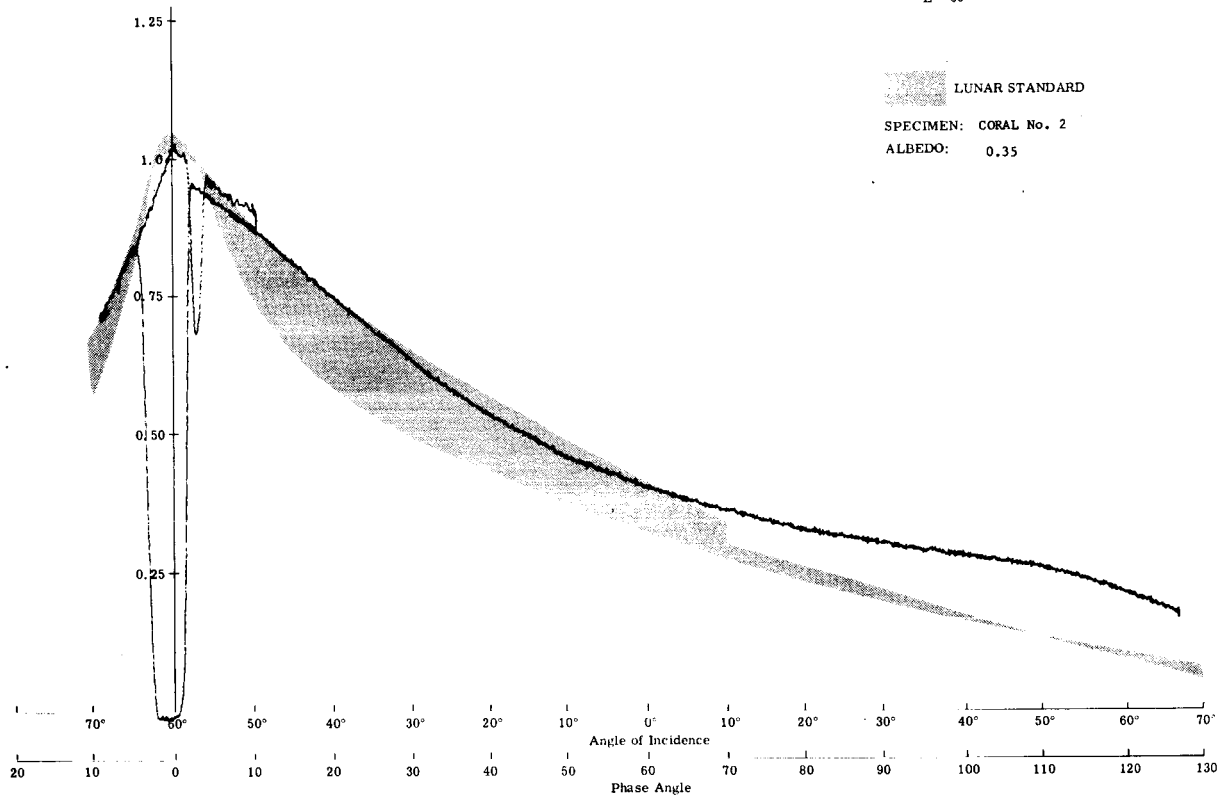
Visible



Blue

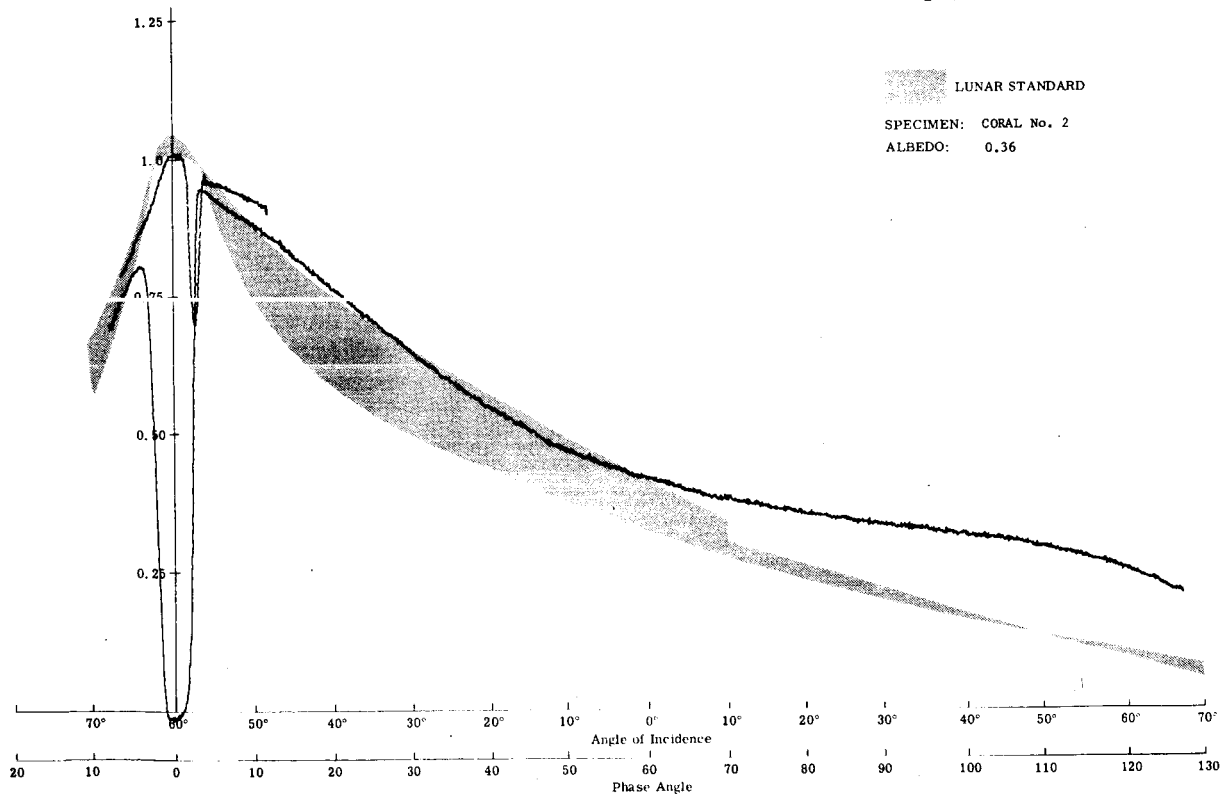
Fig. 8c Photometry of Coral No. 2 (E = 60°)

E = 60°



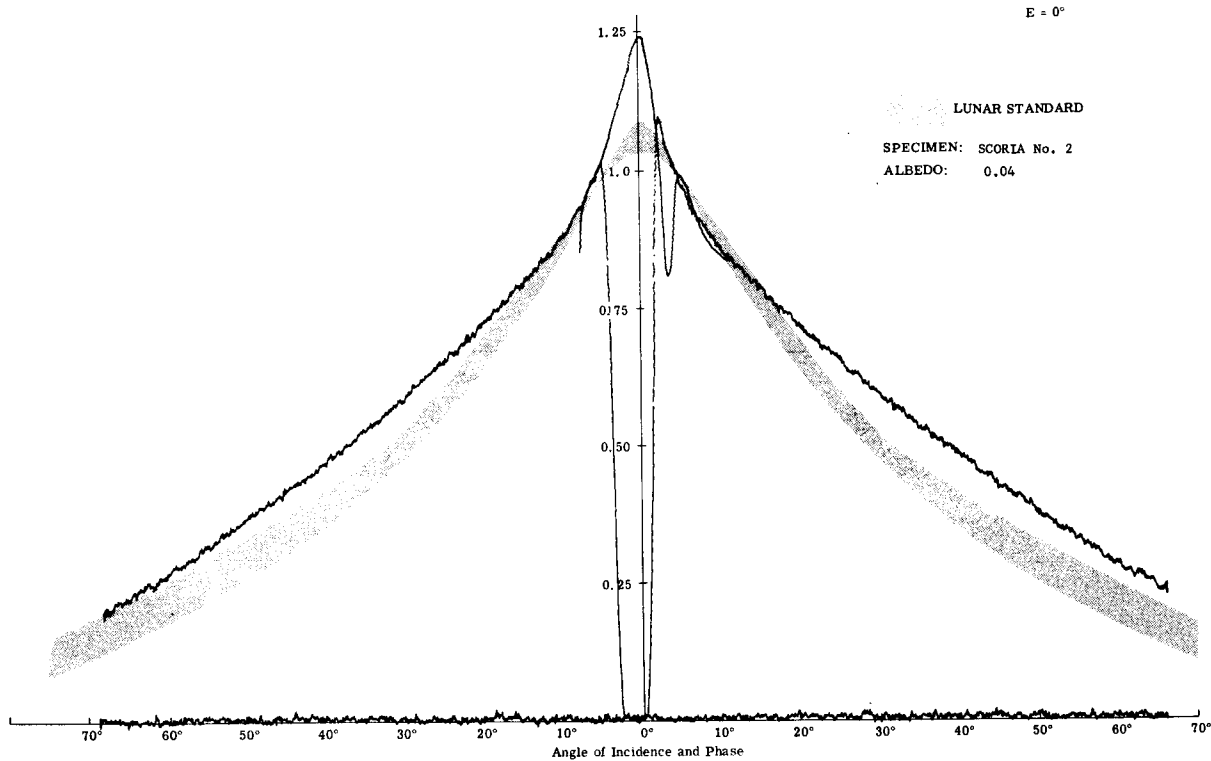
Red

E = 60°

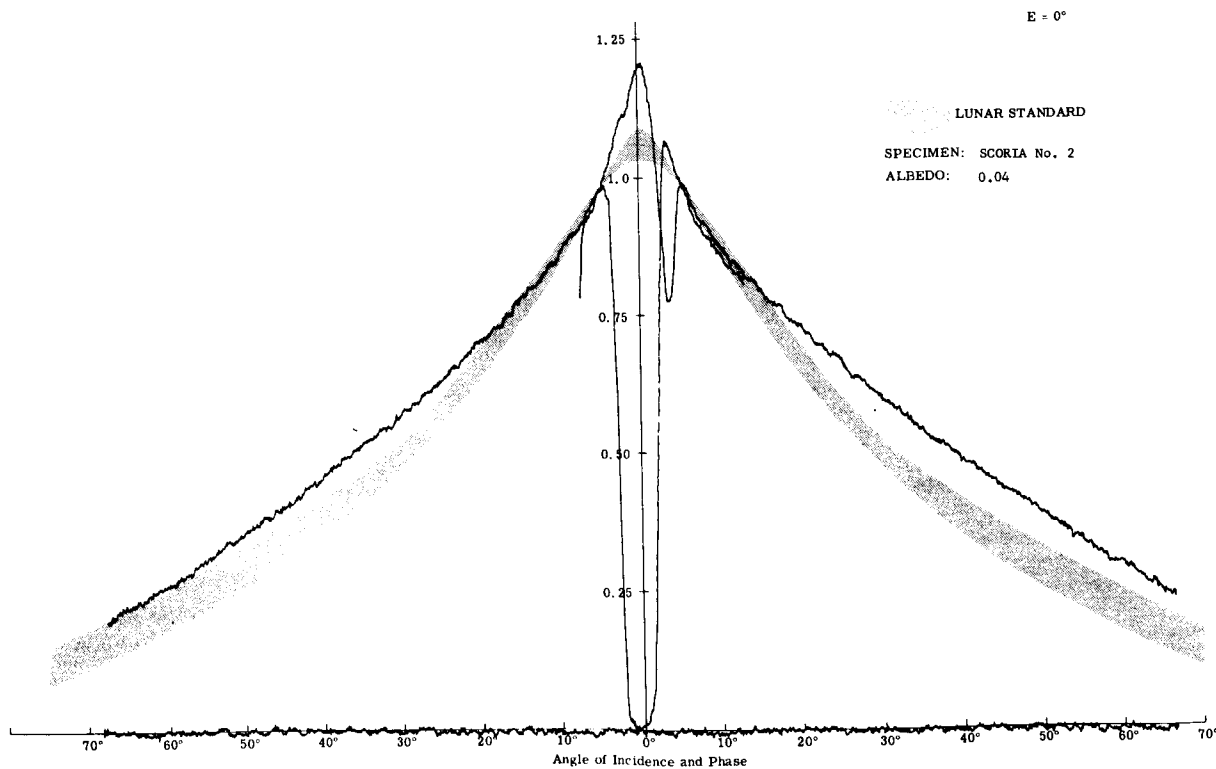


Infrared

Fig. 8c (Cont) Photometry of Coral No. 2 (E = 60°)

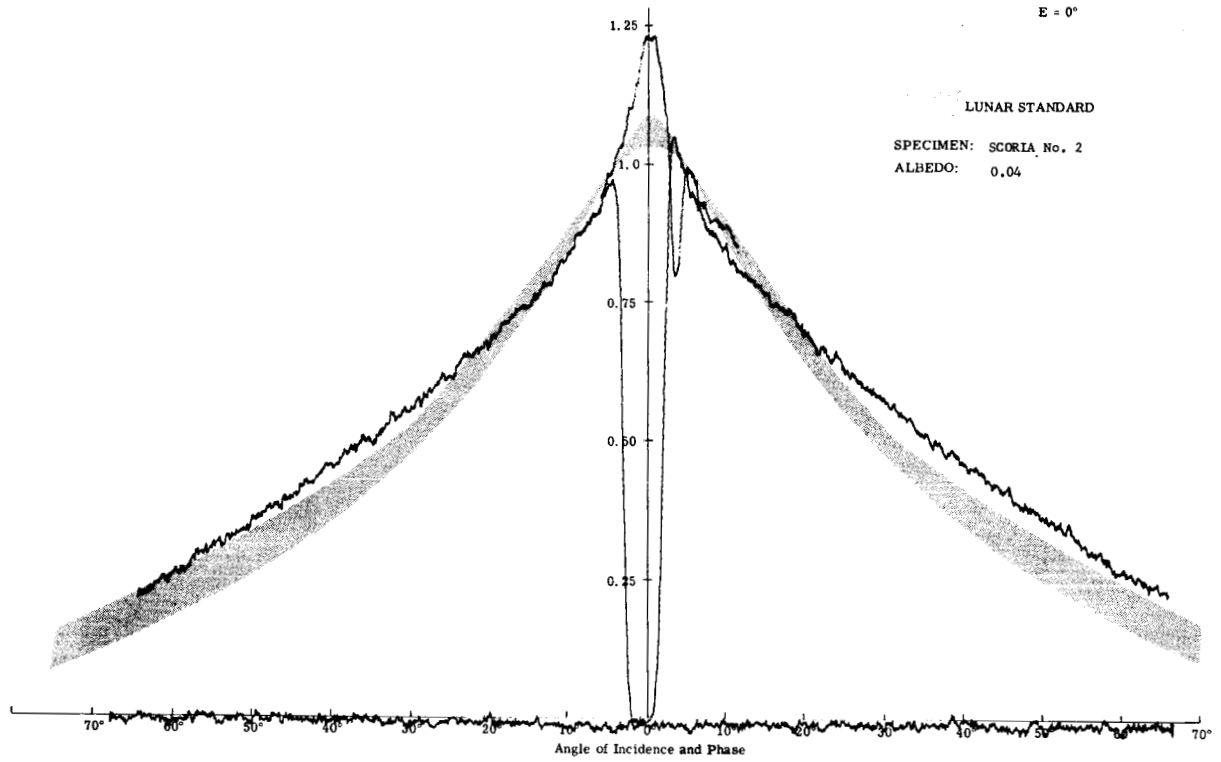


Visible

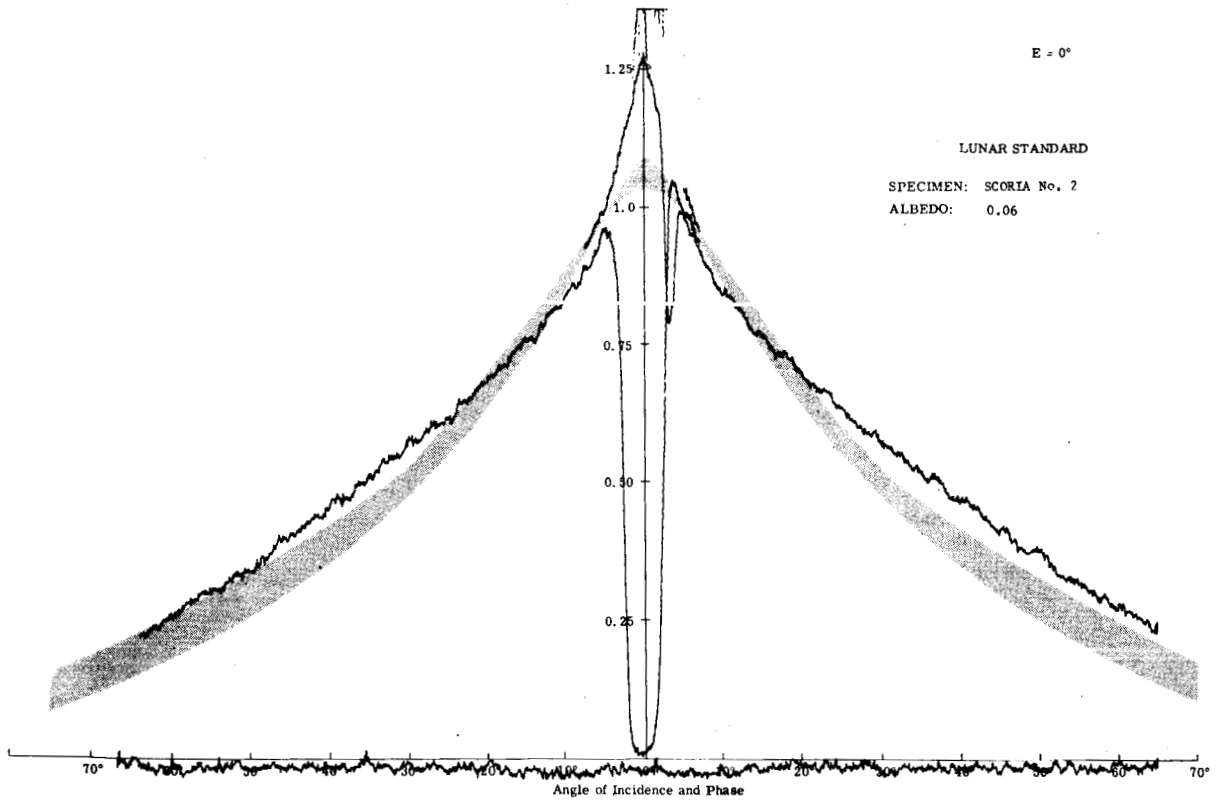


Blue

Fig. 9a Photometry of Scoria No. 2 (E = 0°)



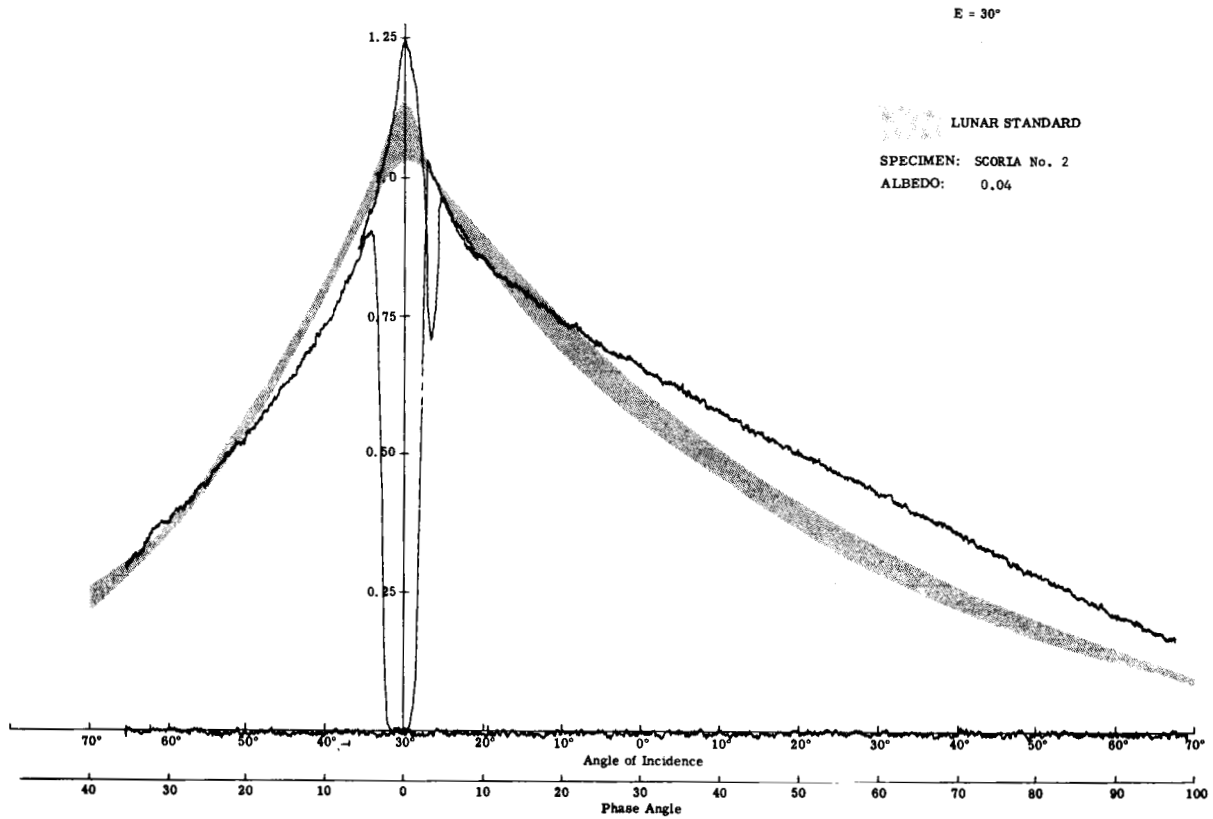
Red



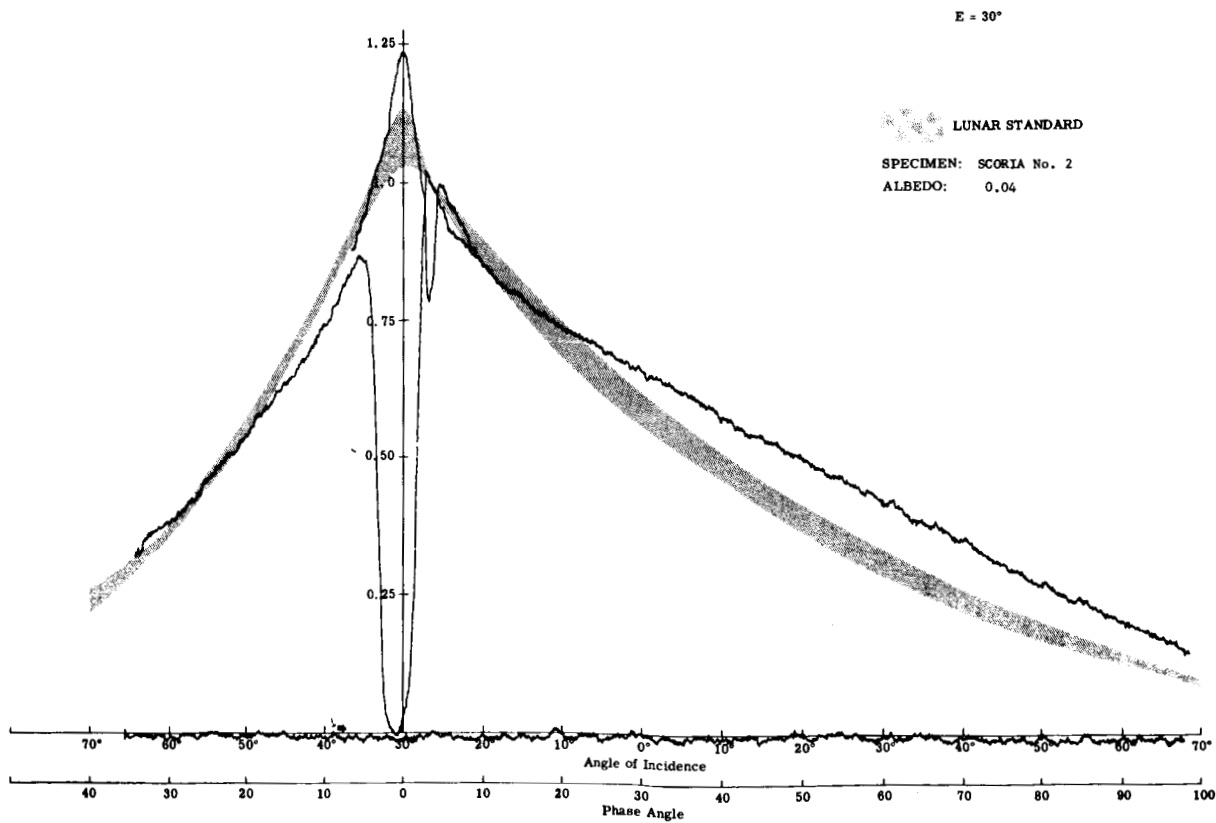
Infrared

Fig. 9a (Cont) Photometry of Scoria No. 2 (E = 0°)

Research Dept  
RM-308  
January 1966

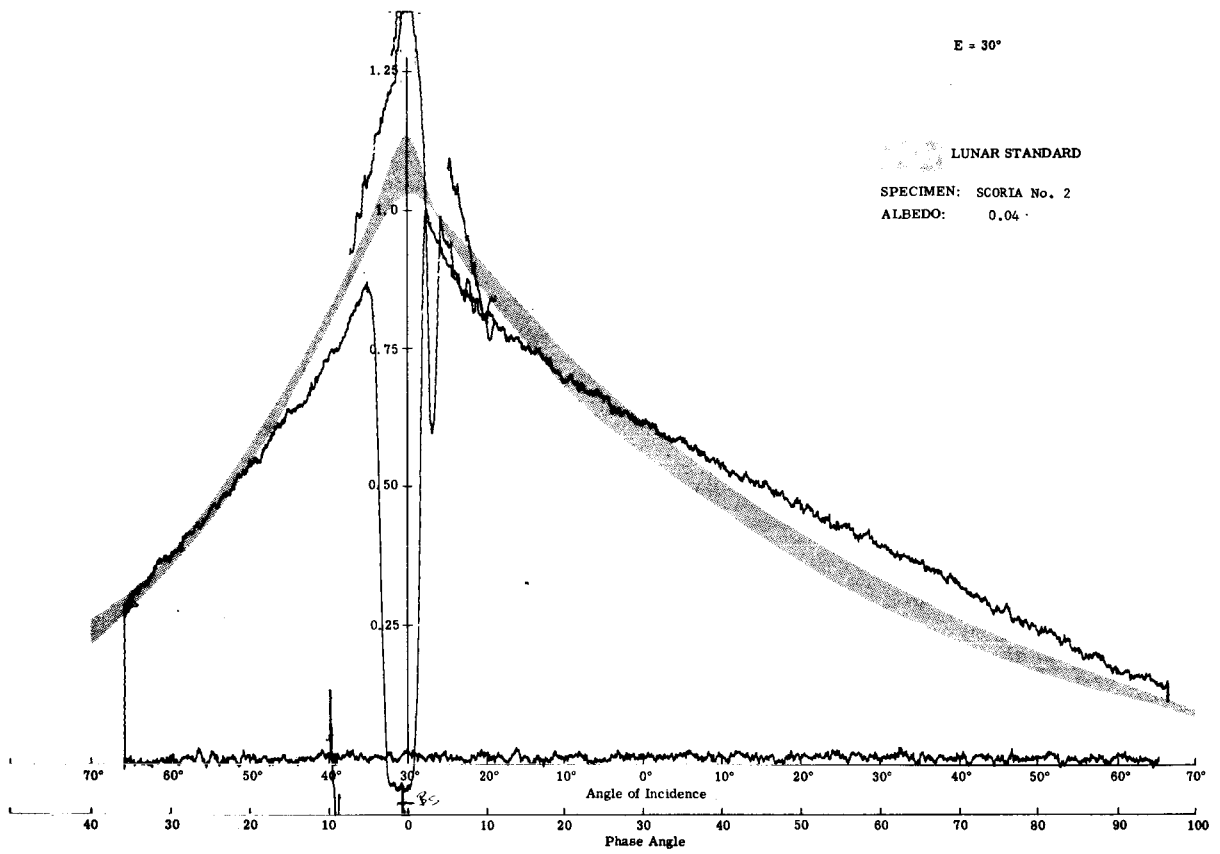


Visible

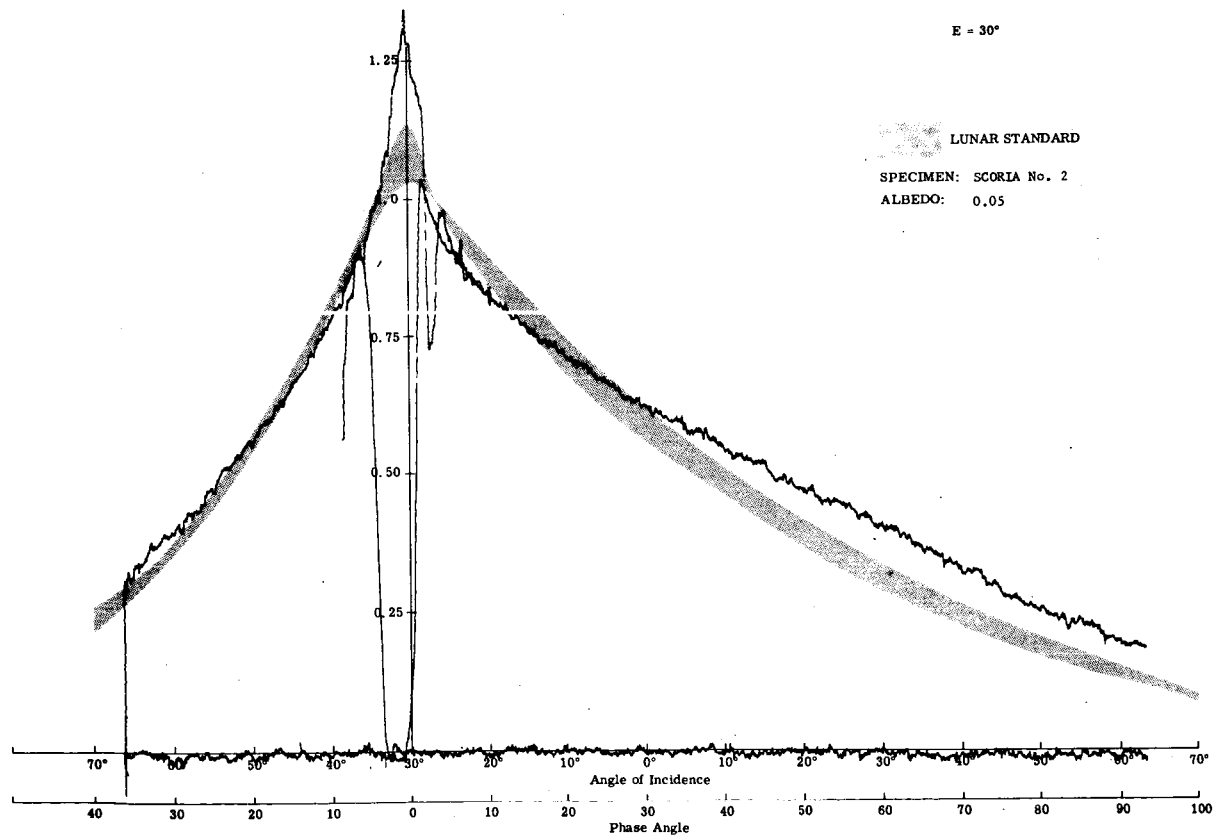


Blue

Fig. 9b Photometry of Scoria No. 2 (E = 30°)



Red

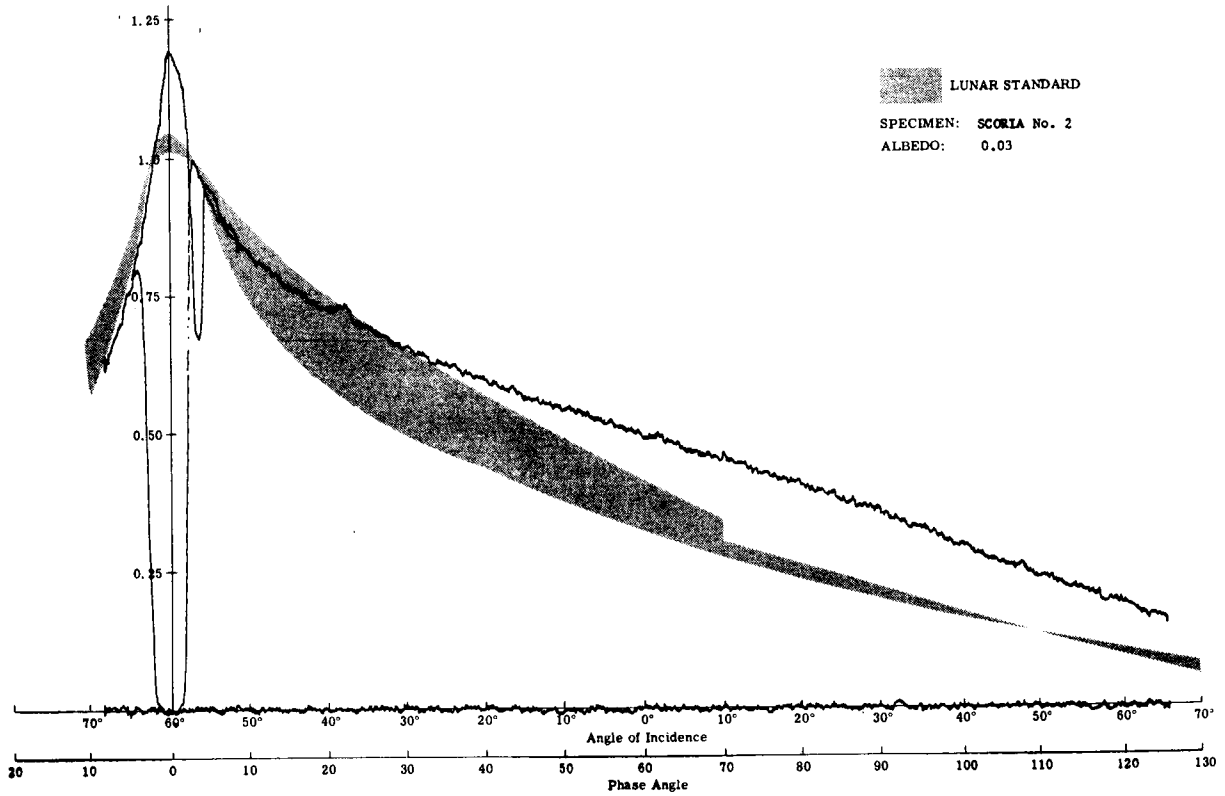


Infrared

Fig. 9b (Cont) Photometry of Scoria No. 2 (E = 30°)

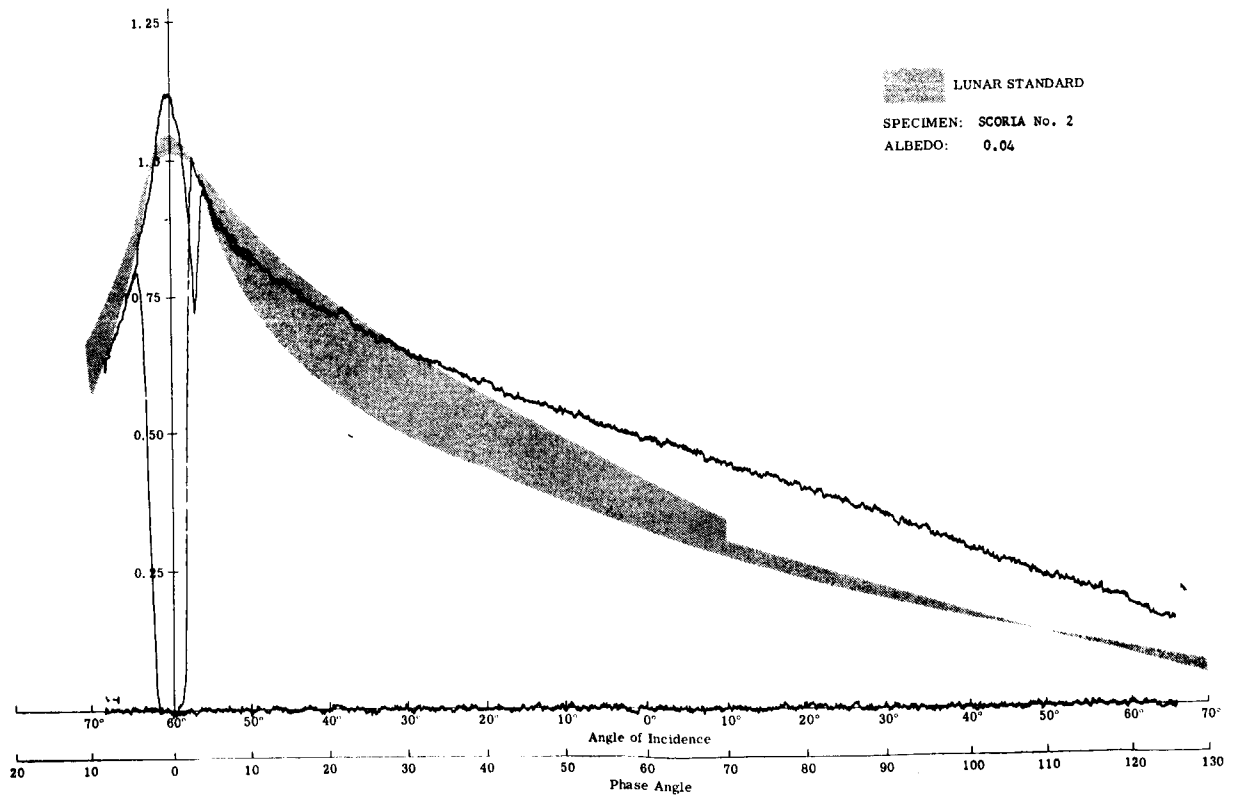
Research Dept  
RM-308  
January 1966

E = 60°



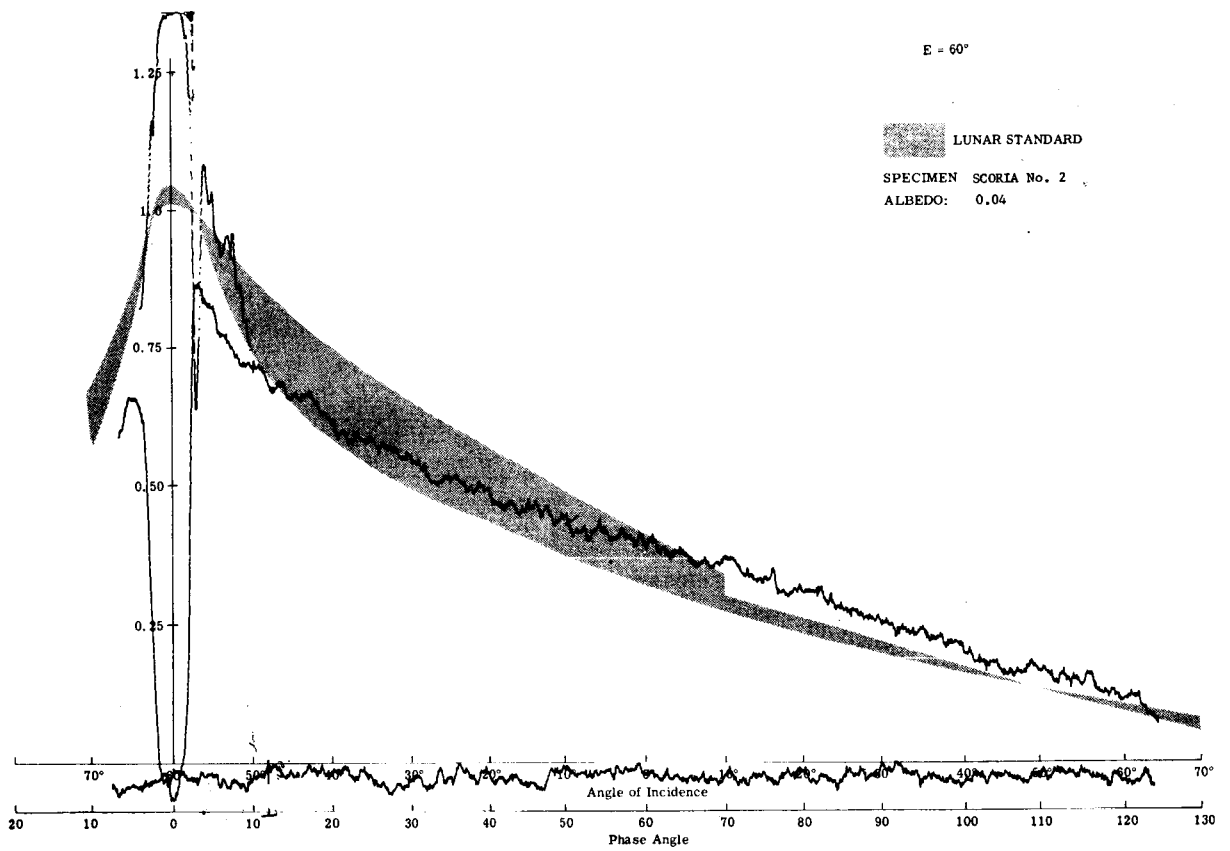
Visible

E = 60°

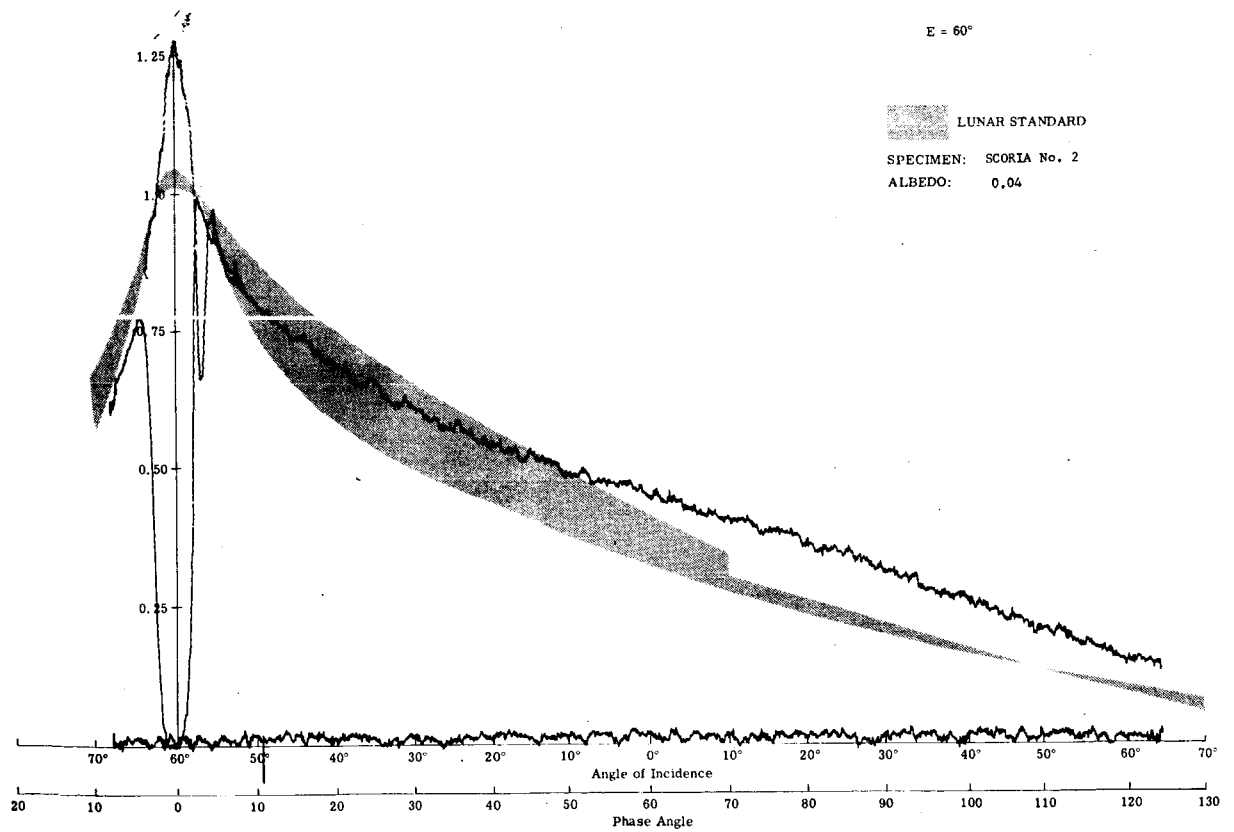


Blue

Fig. 9c Photometry of Scoria No. 2 (E = 60°)



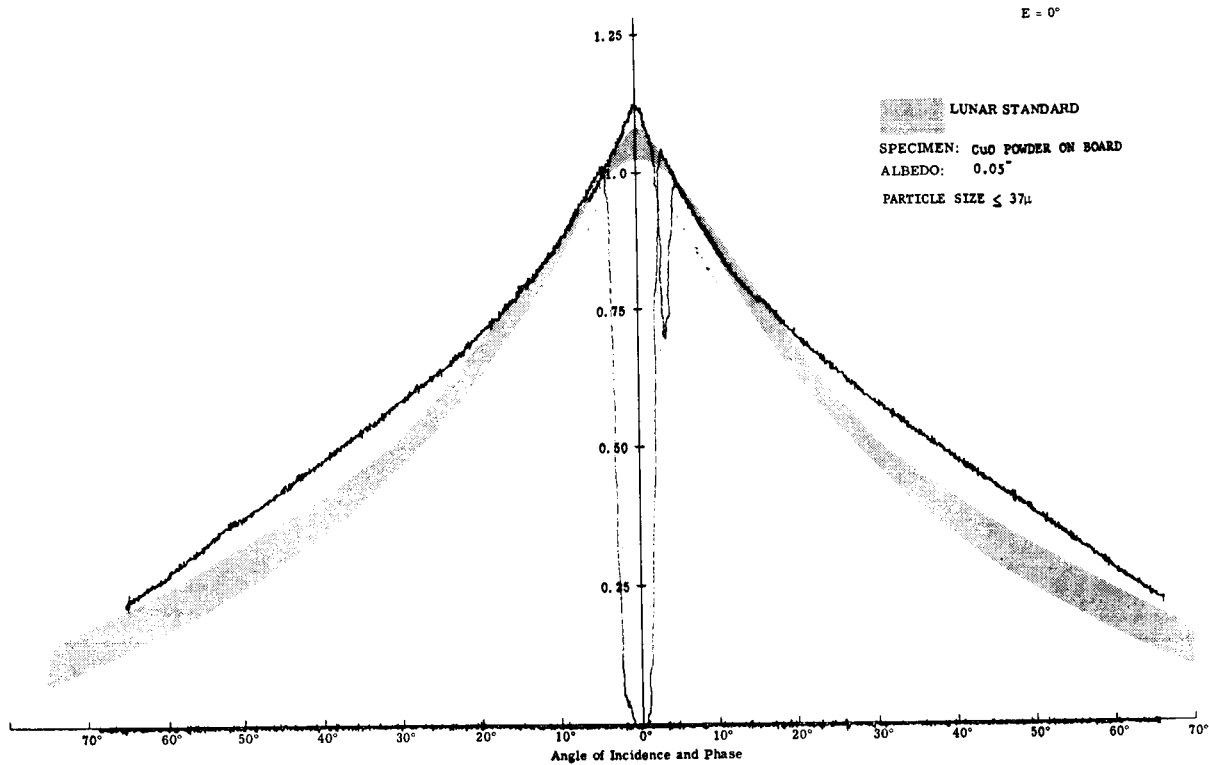
Red



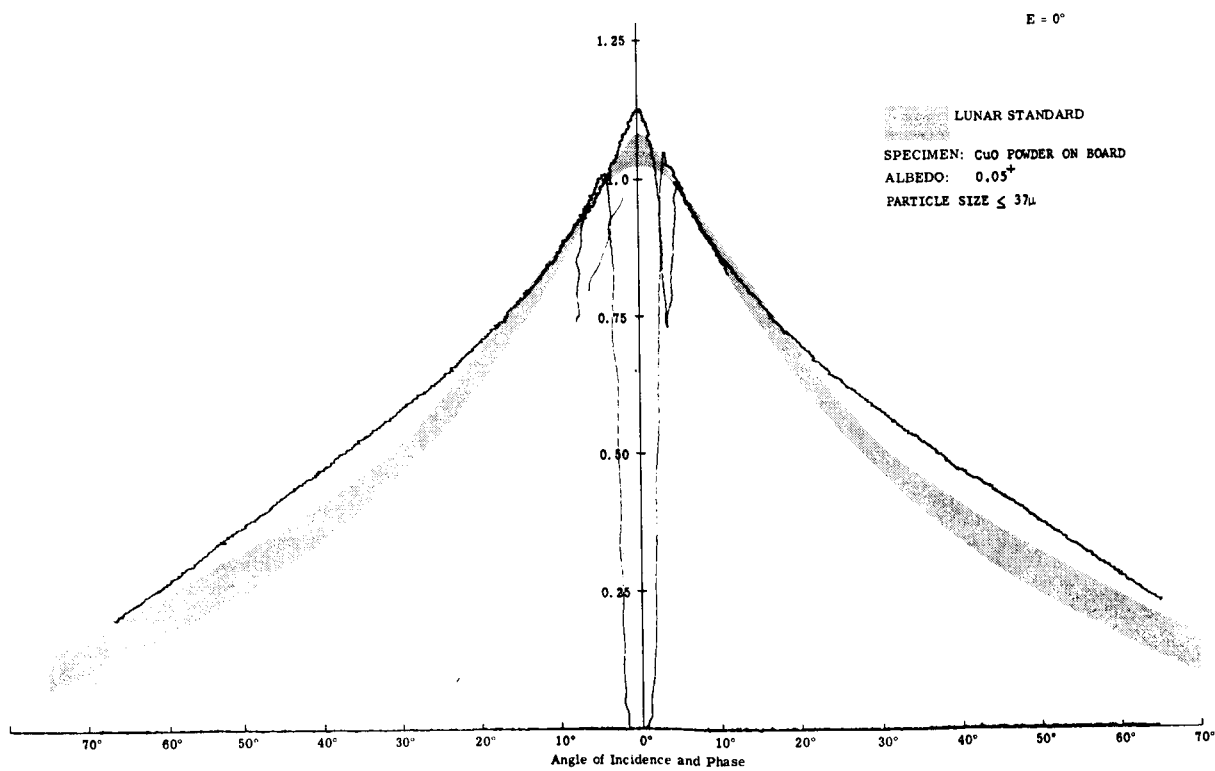
Infrared

Fig. 9c (Cont) Photometry of Scoria No. 2 (E = 60°)



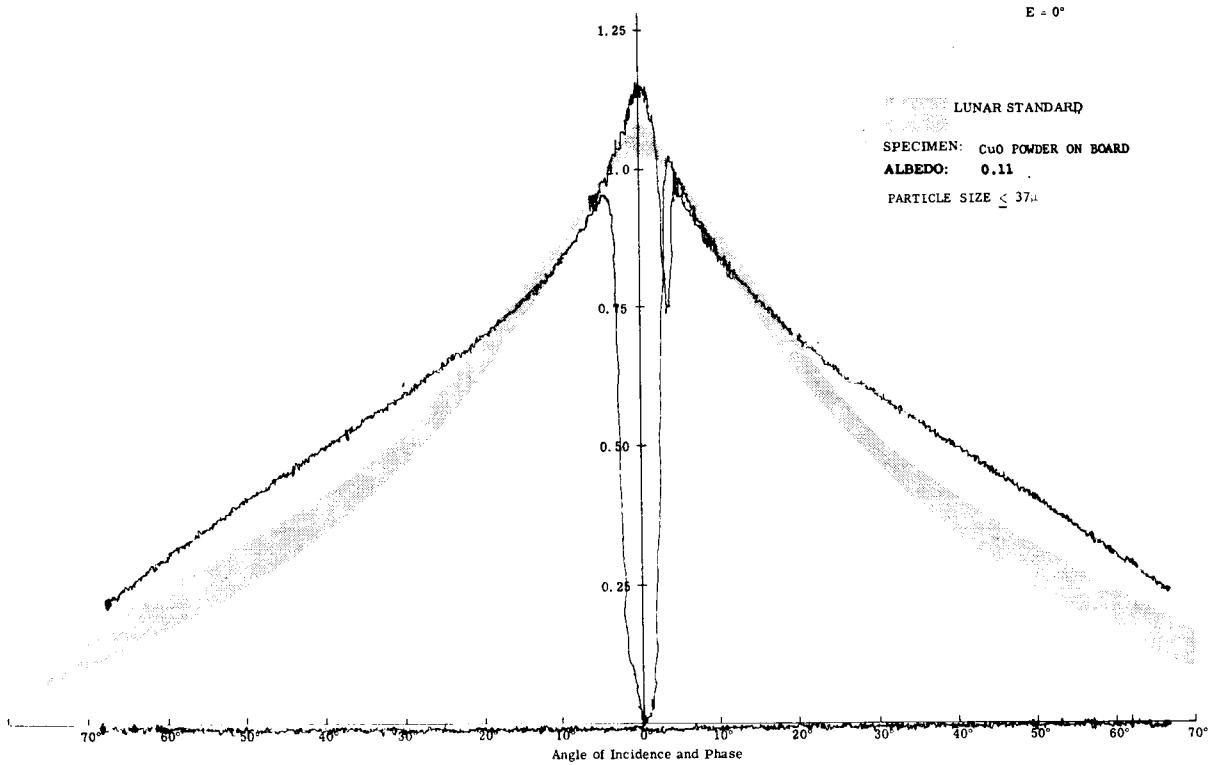


Visible

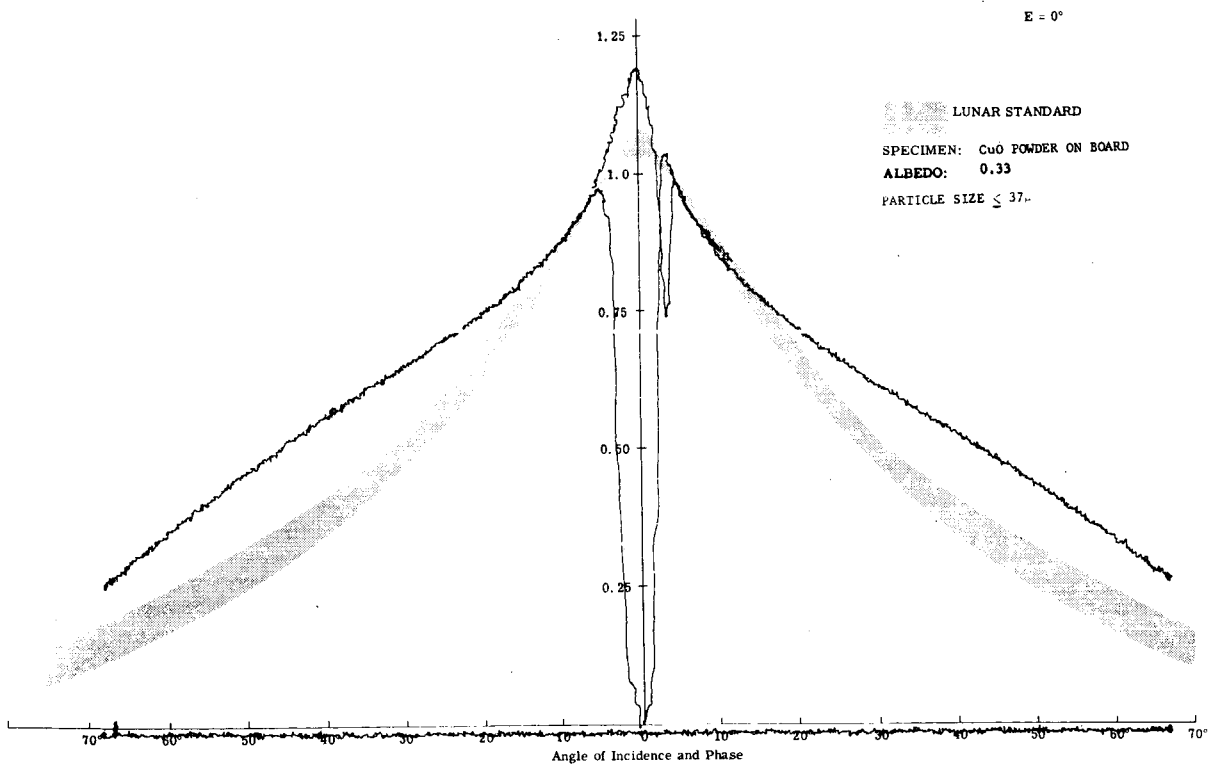


Blue

Fig. 10a Photometry of Copper Oxide Powder  
on Flat Board (E = 0°)



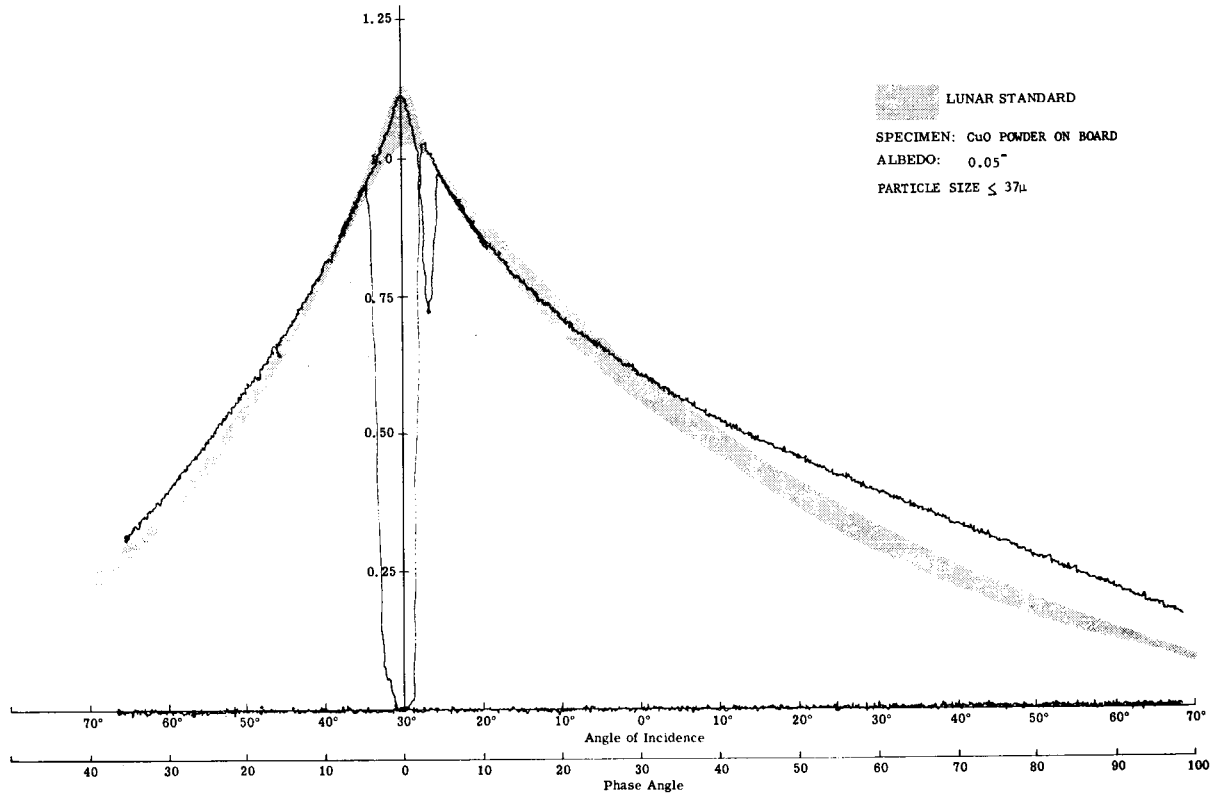
Red



Infrared

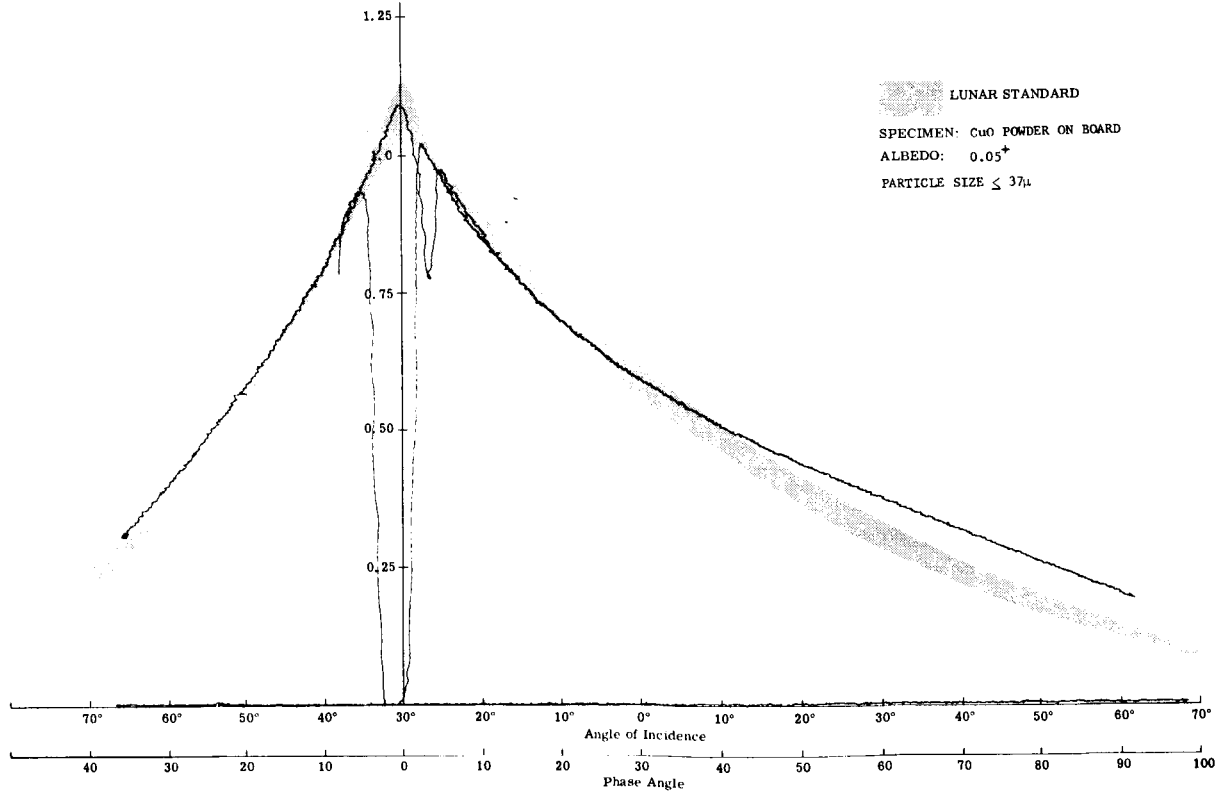
Fig. 10a (Cont) Photometry of Copper Oxide Powder  
on Flat Plate (E = 0°)

E = 30°



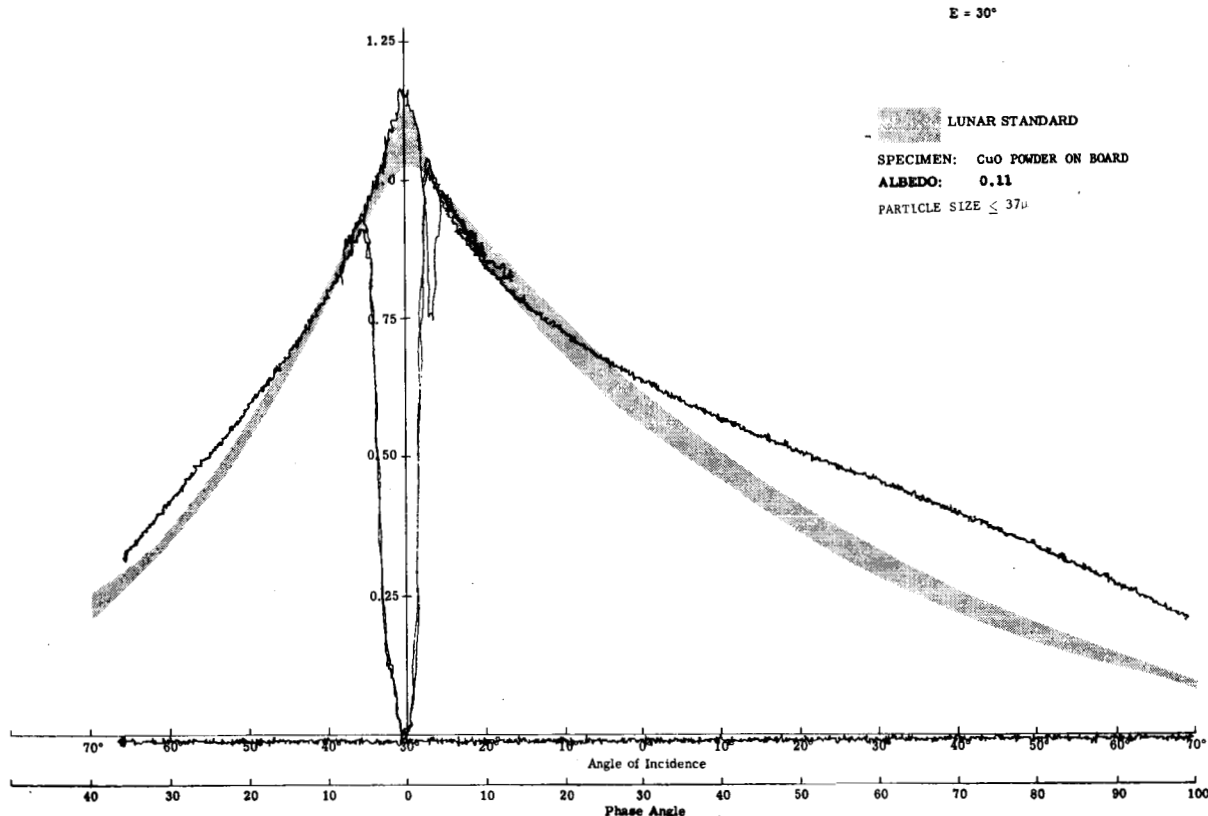
Visible

E = 30°

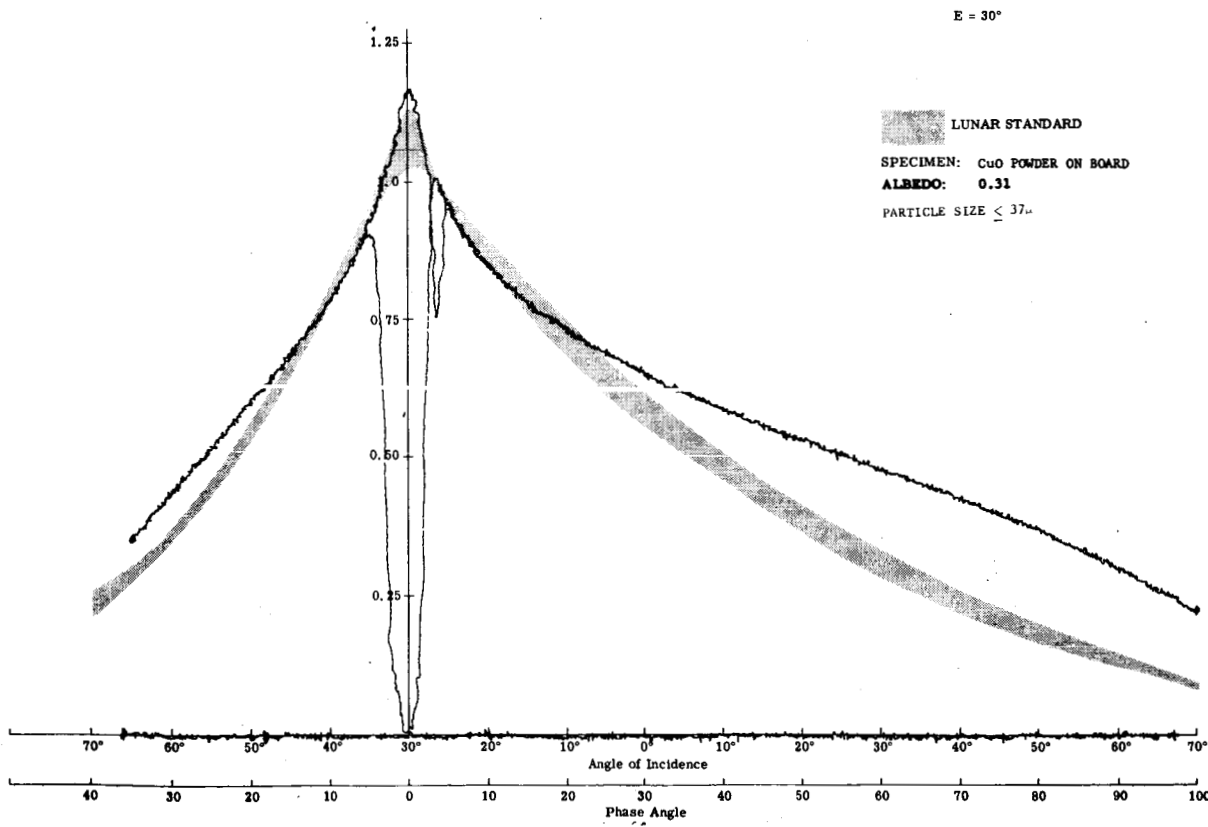


Blue

Fig. 10b Photometry of Copper Oxide Powder on Flat Board (E = 30°)

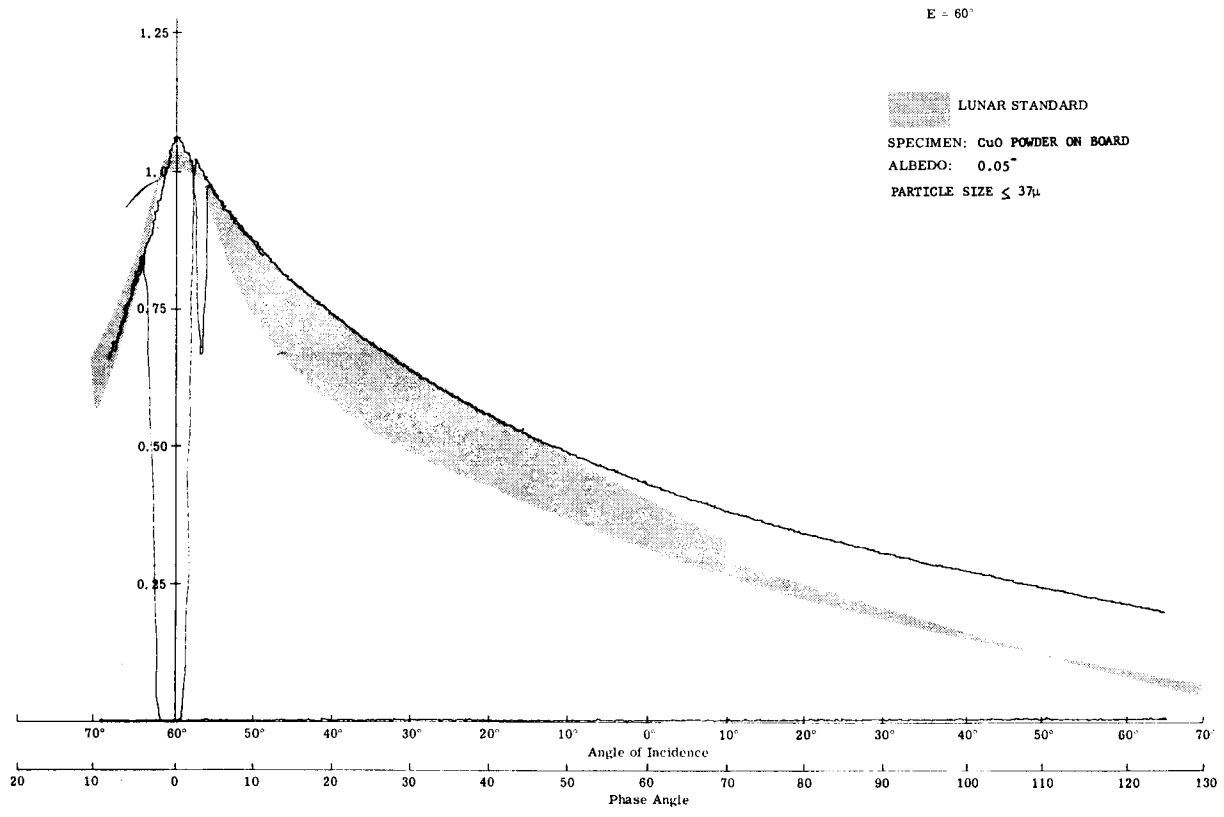


Red

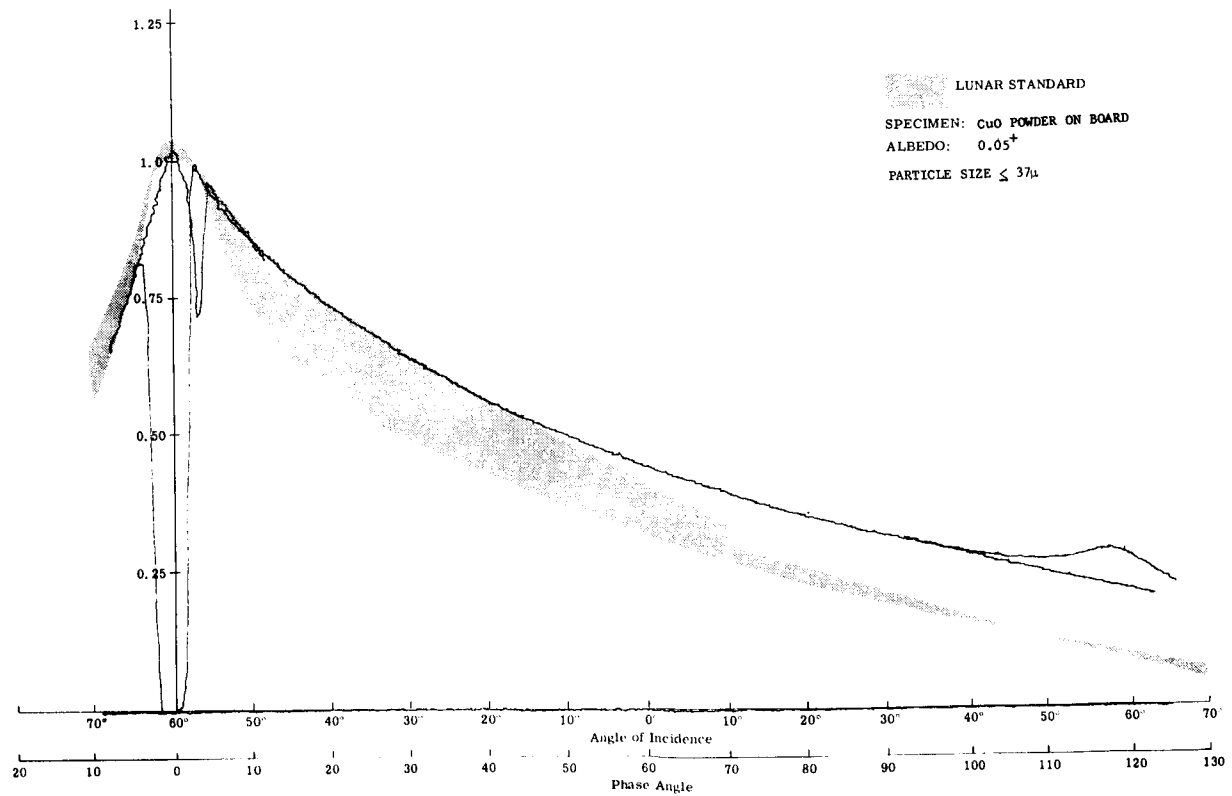


Infrared

Fig. 10b (Cont) Photometry of Copper Oxide Powder  
on Flat Board (E = 30°)

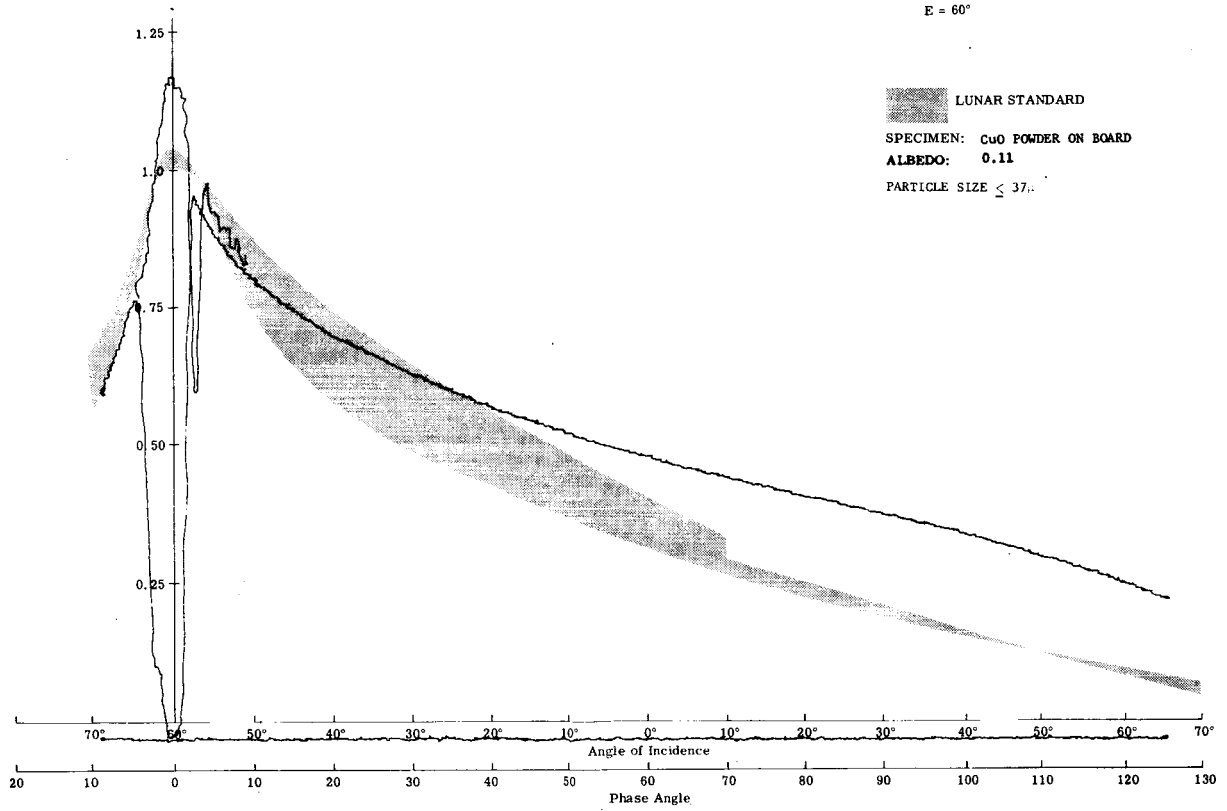


**Visible**

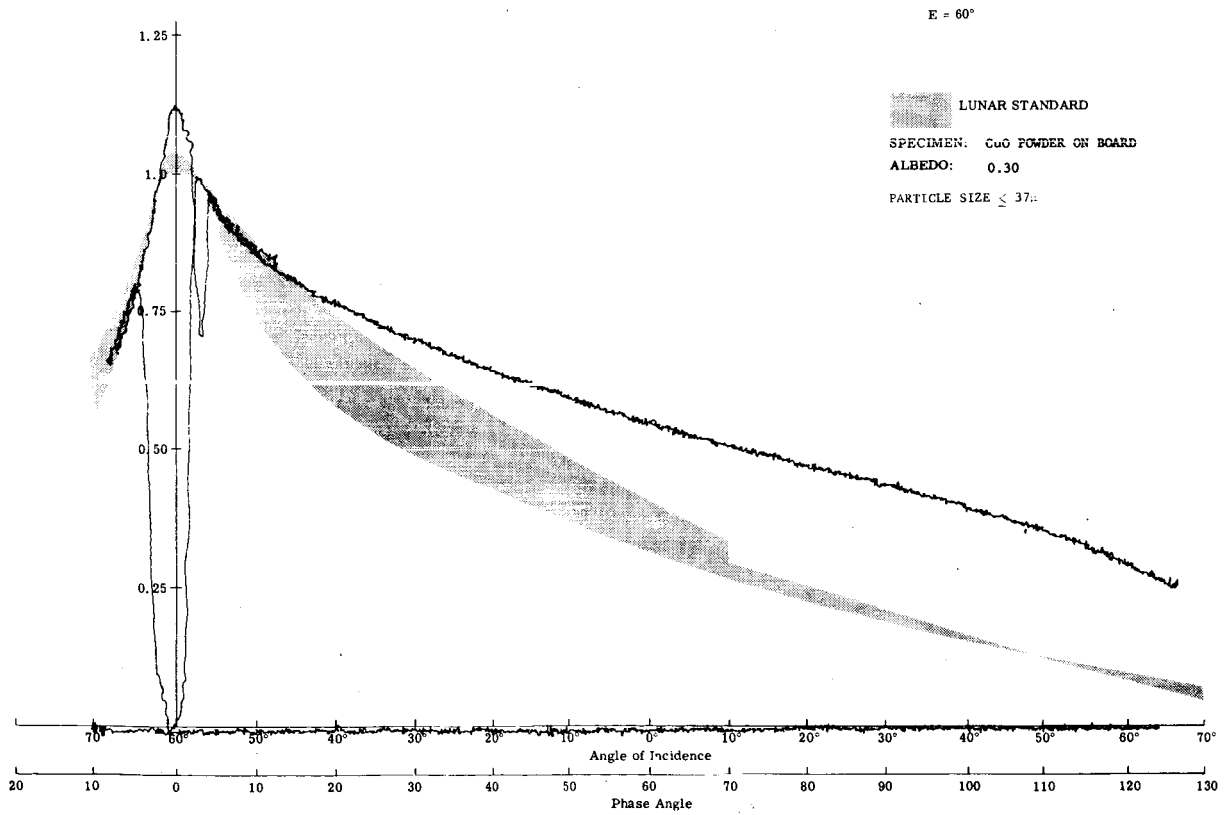


**Blue**

**Fig. 10c Photometry of Copper Oxide Powder on Flat Board (E = 60°)**

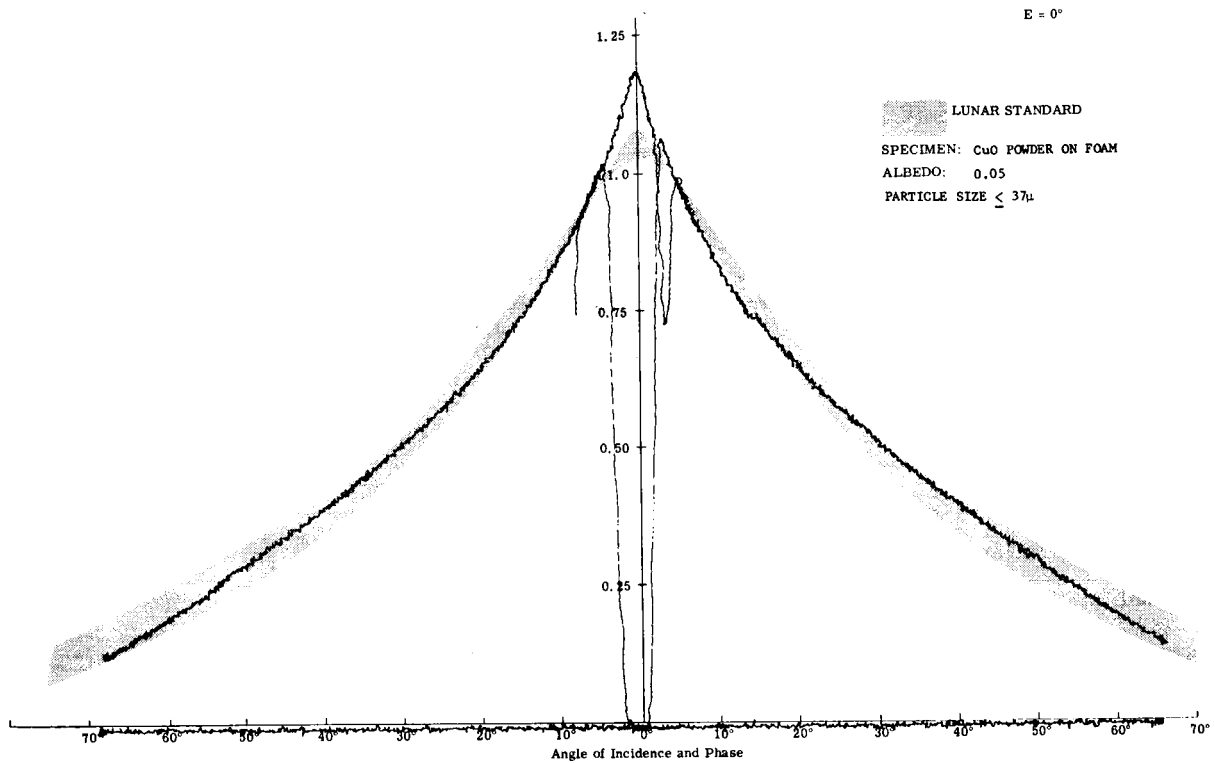


Red

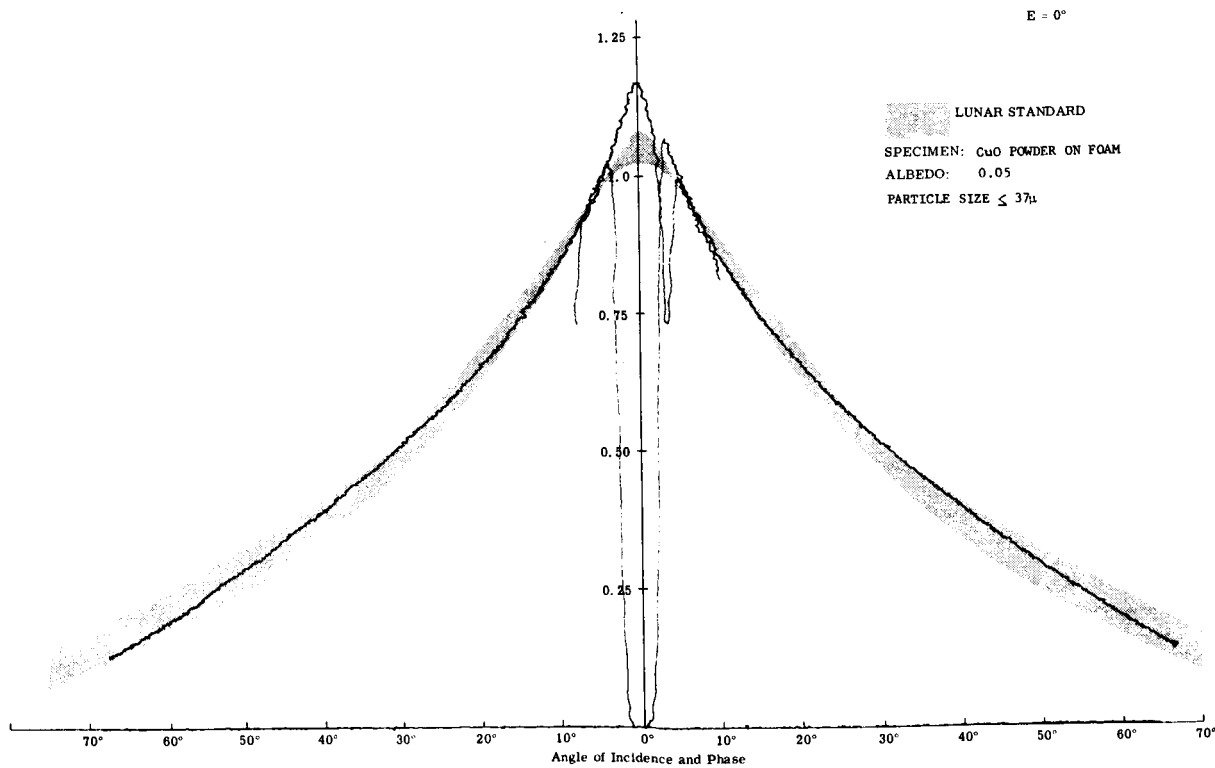


Infrared

Fig. 10c (Cont) Photometry of Copper Oxide Powder  
on Flat Board (E = 60°)

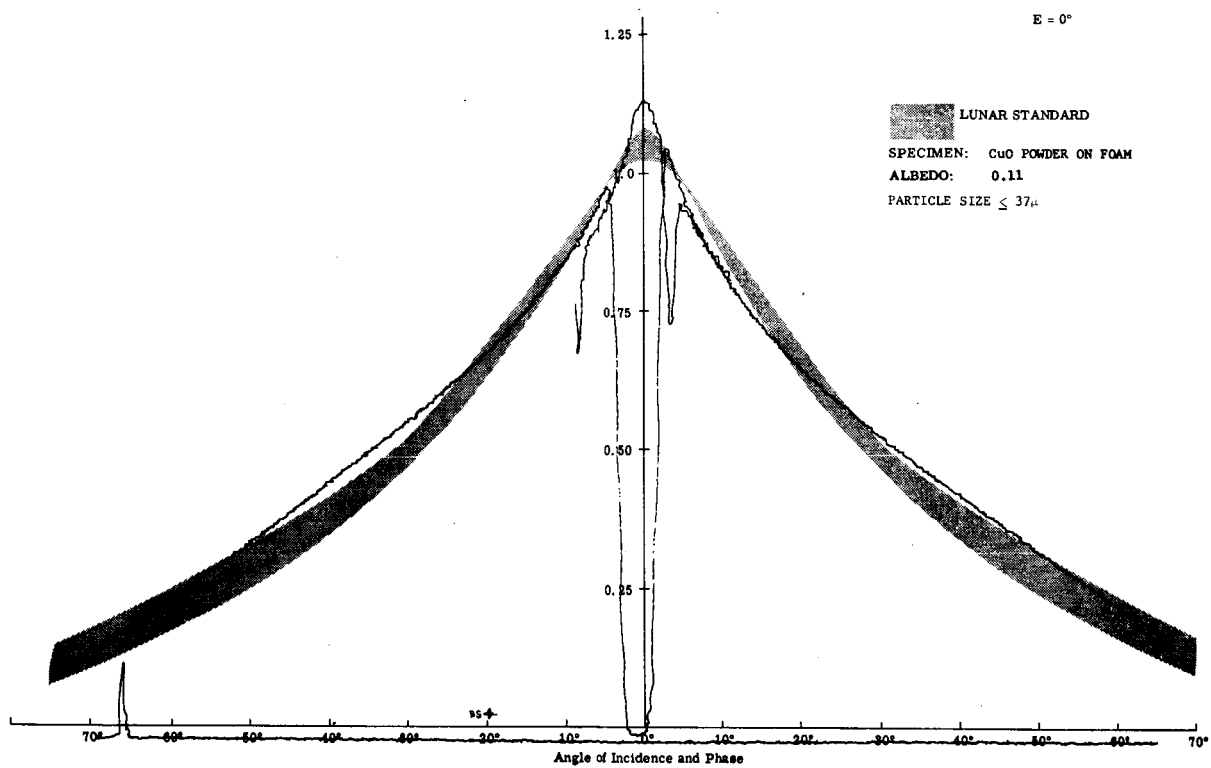


Visible

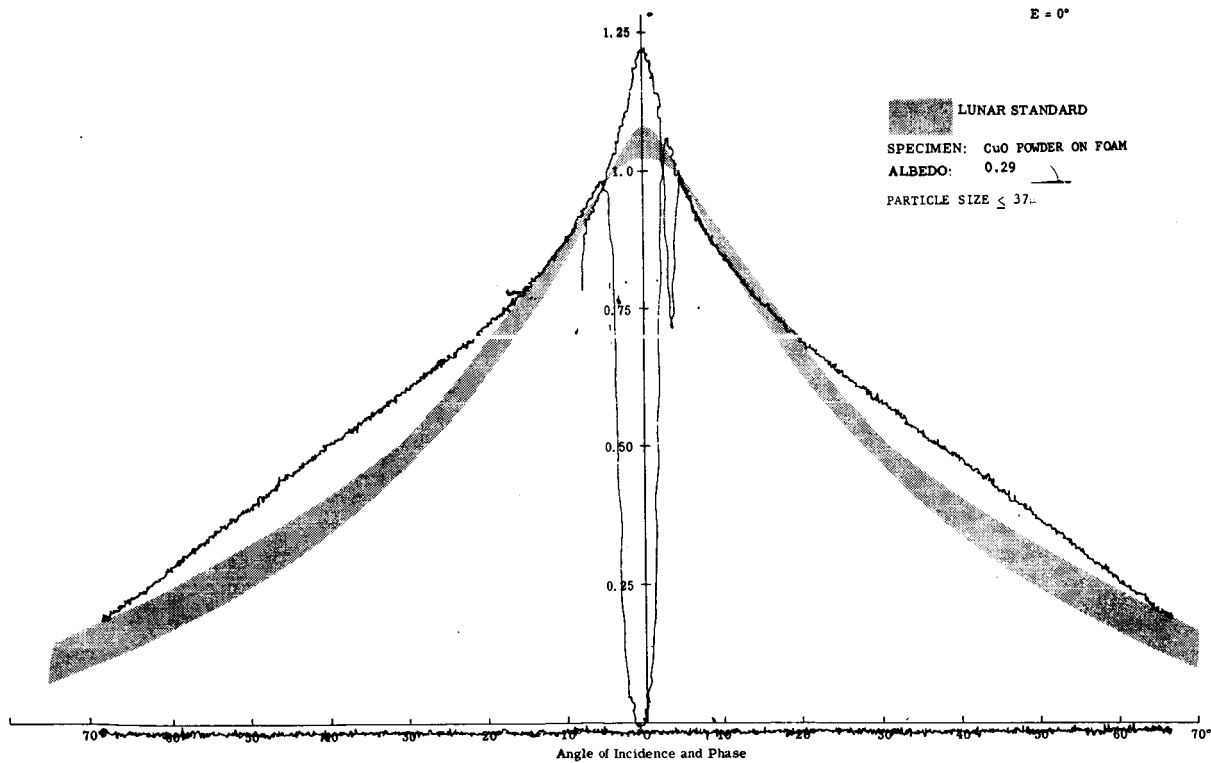


Blue

Fig. 11a Photometry of Copper Oxide Powder  
 on Foam (E = 0°)



Red

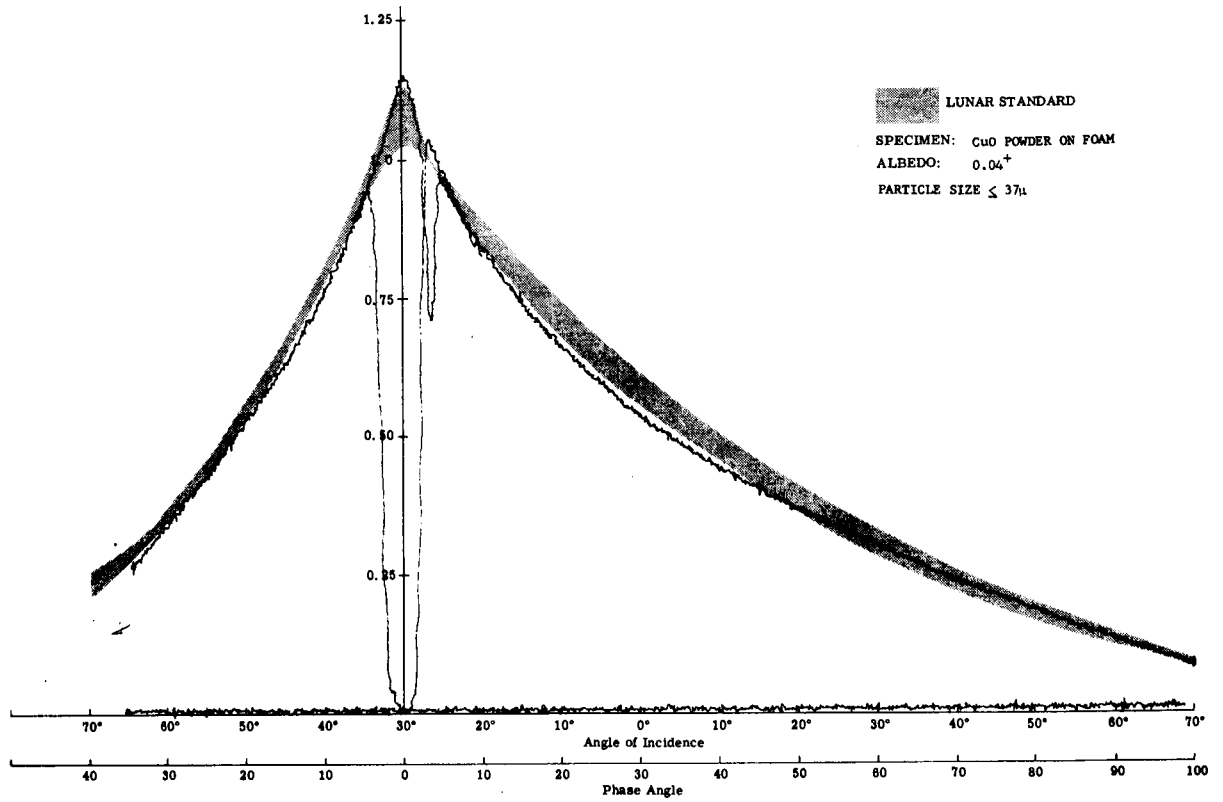


Infrared

Fig. 11a (Cont) Photometry of Copper Oxide Powder  
on Foam (E = 0°)

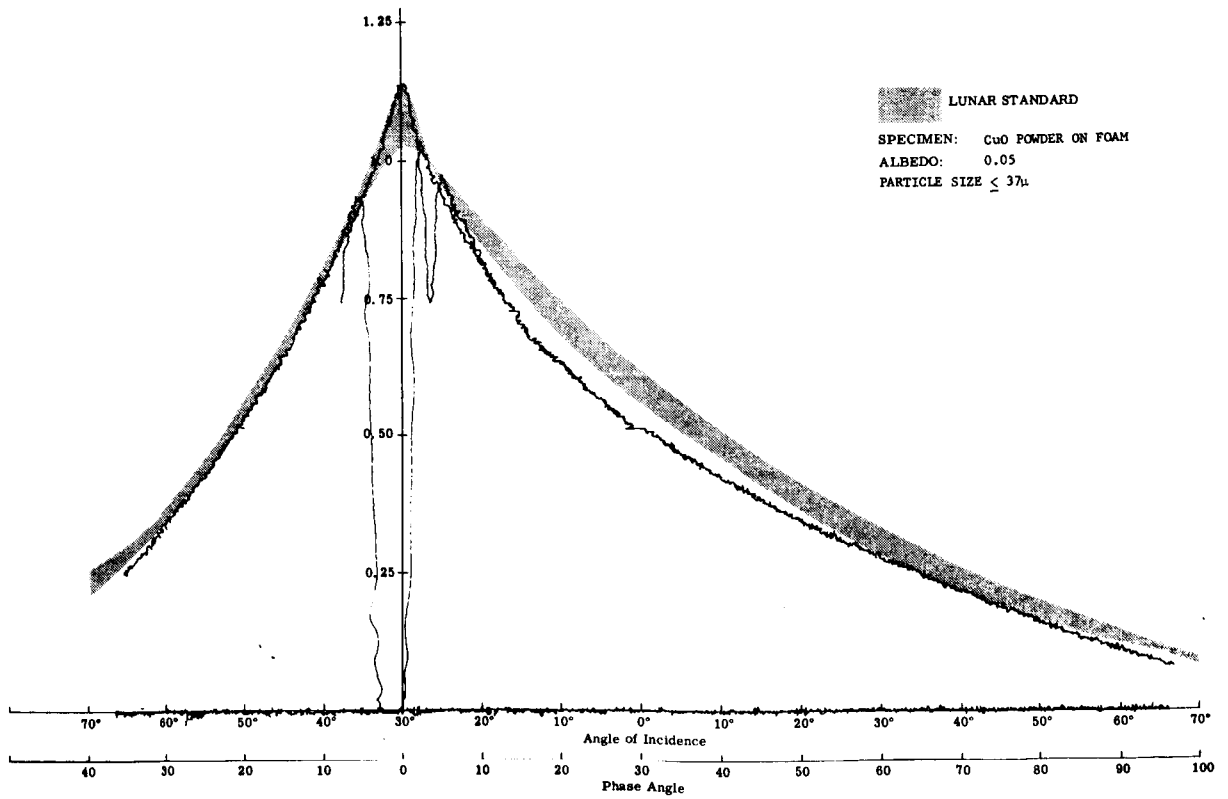


E = 30°



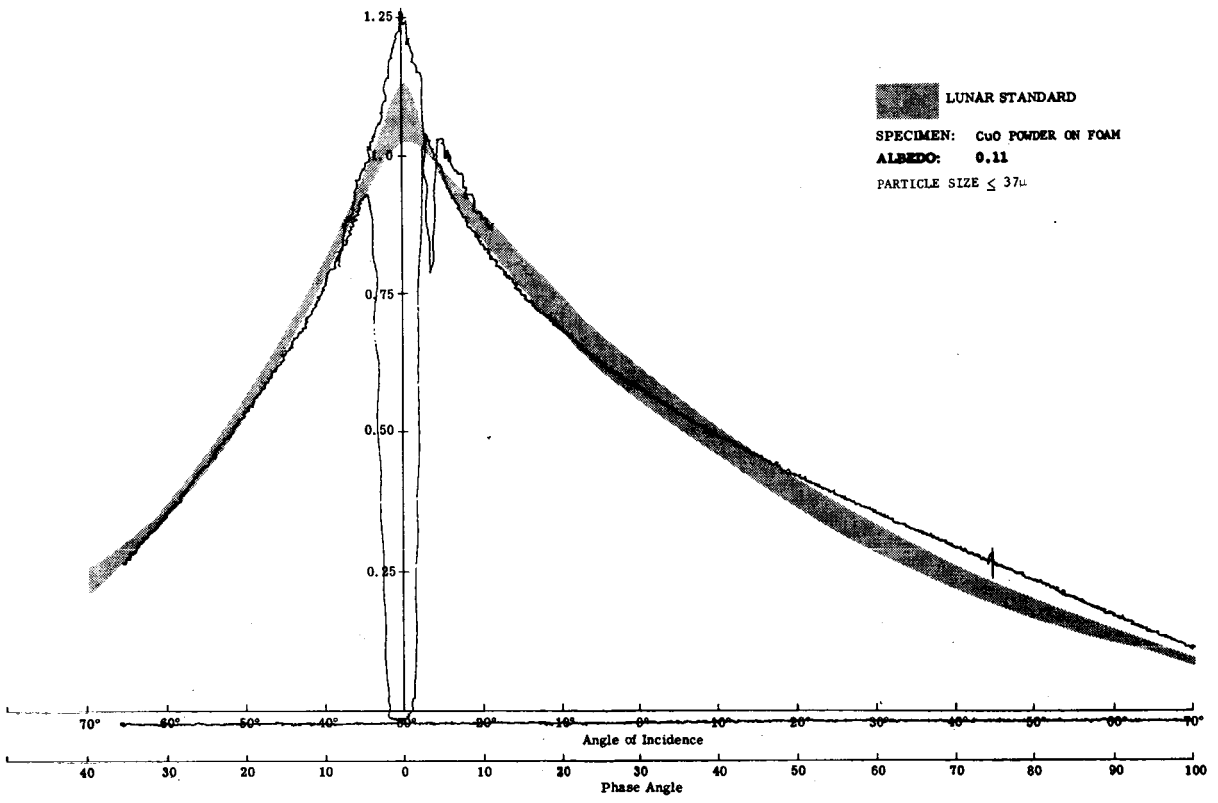
Visible

E = 30°

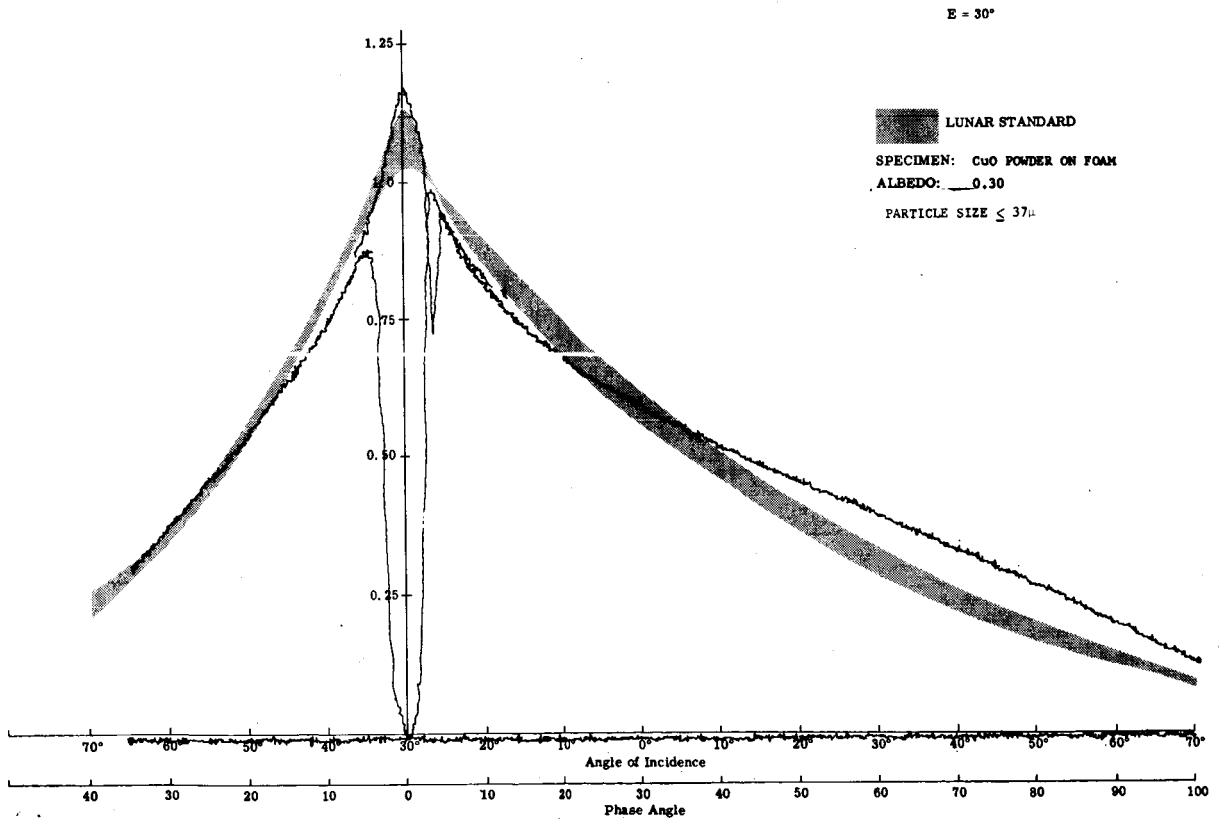


Blue

Fig. 11b Photometry of Copper Oxide Powder on Foam (E = 30°)



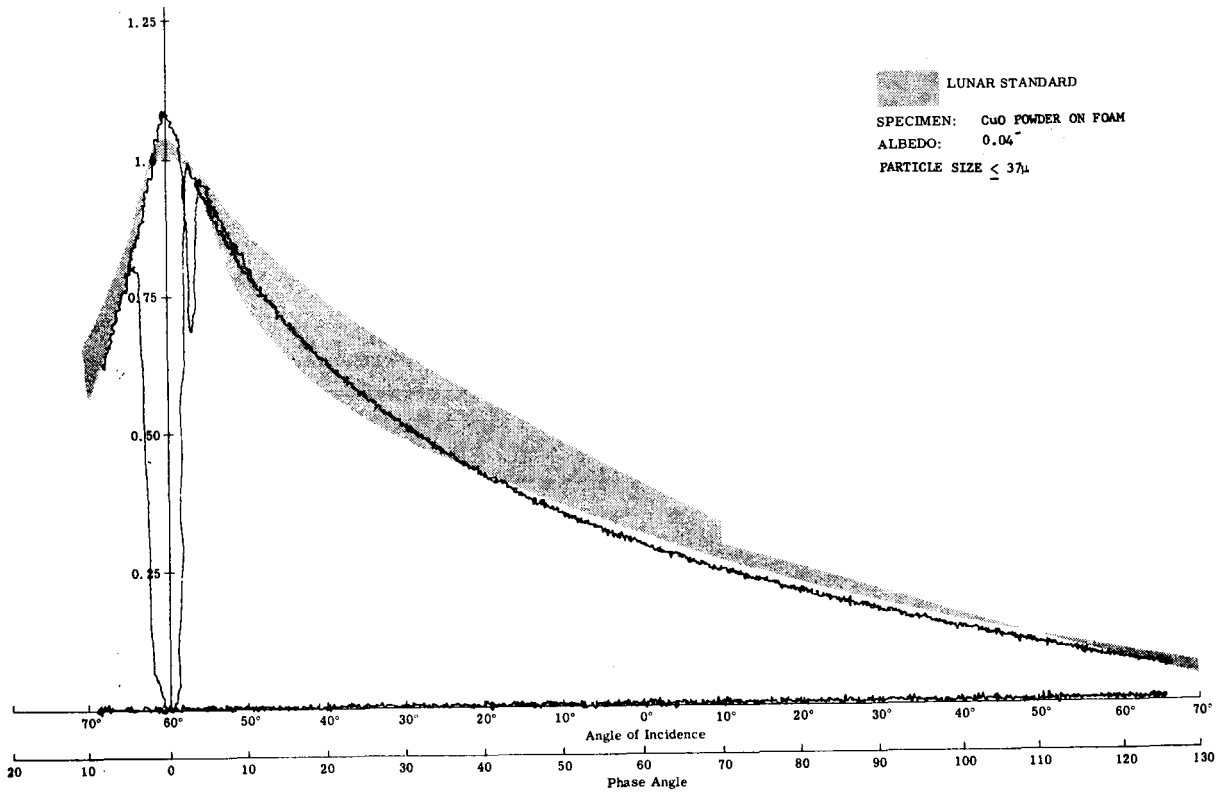
Red



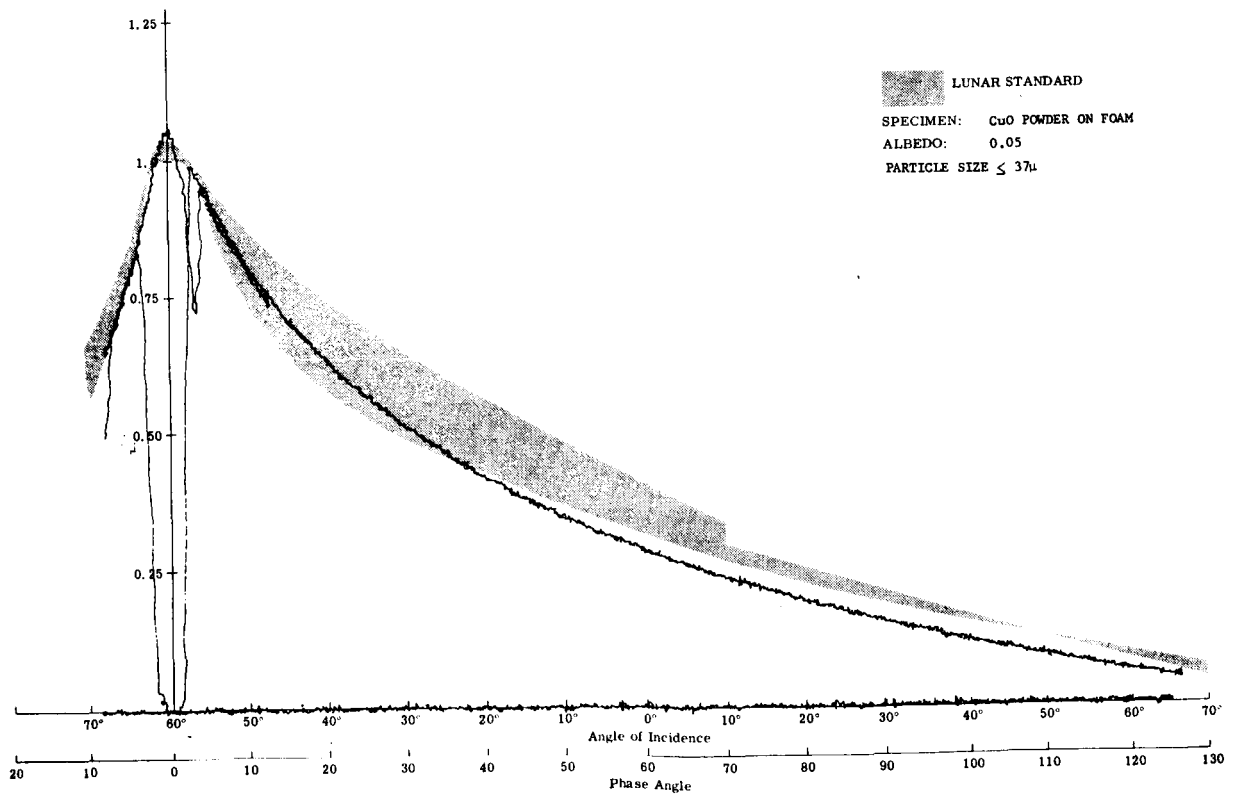
Infrared

Fig. 11b (Cont) Photometry of Copper Oxide Powder on Foam (E = 30°)

E = 60°



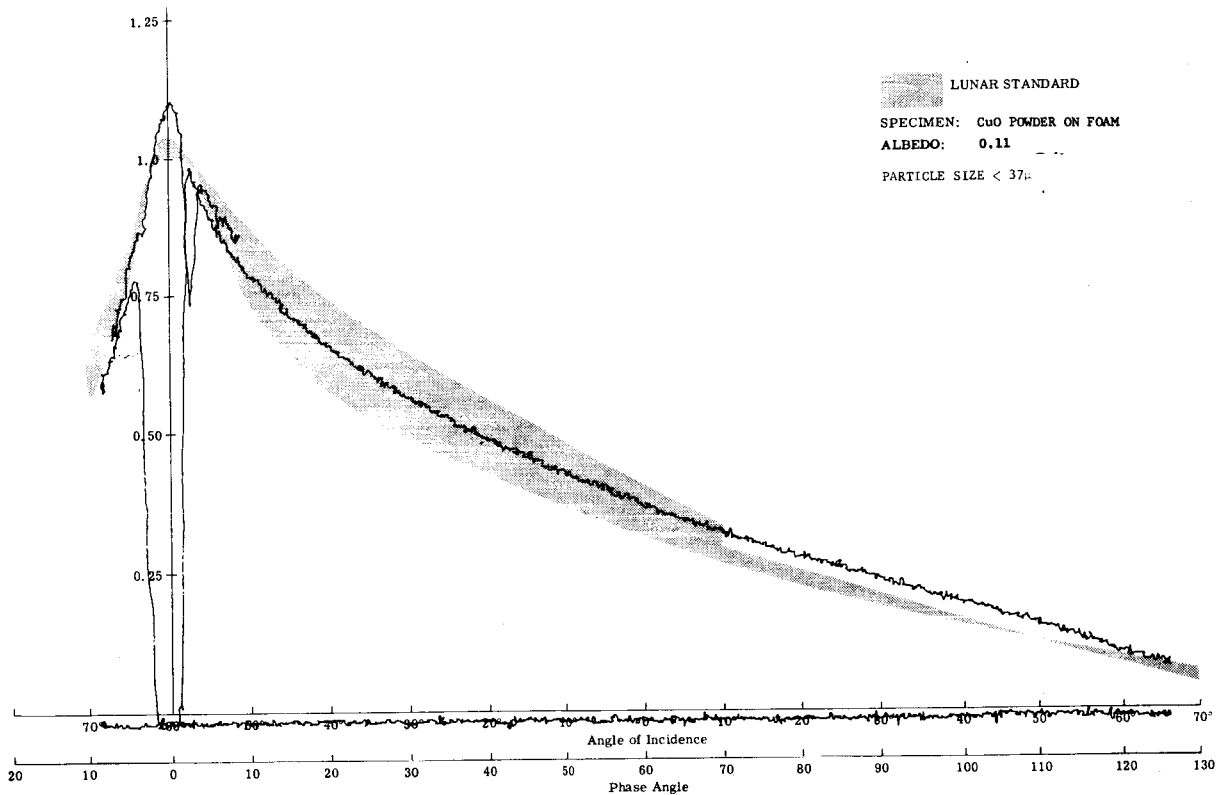
Visible



Blue

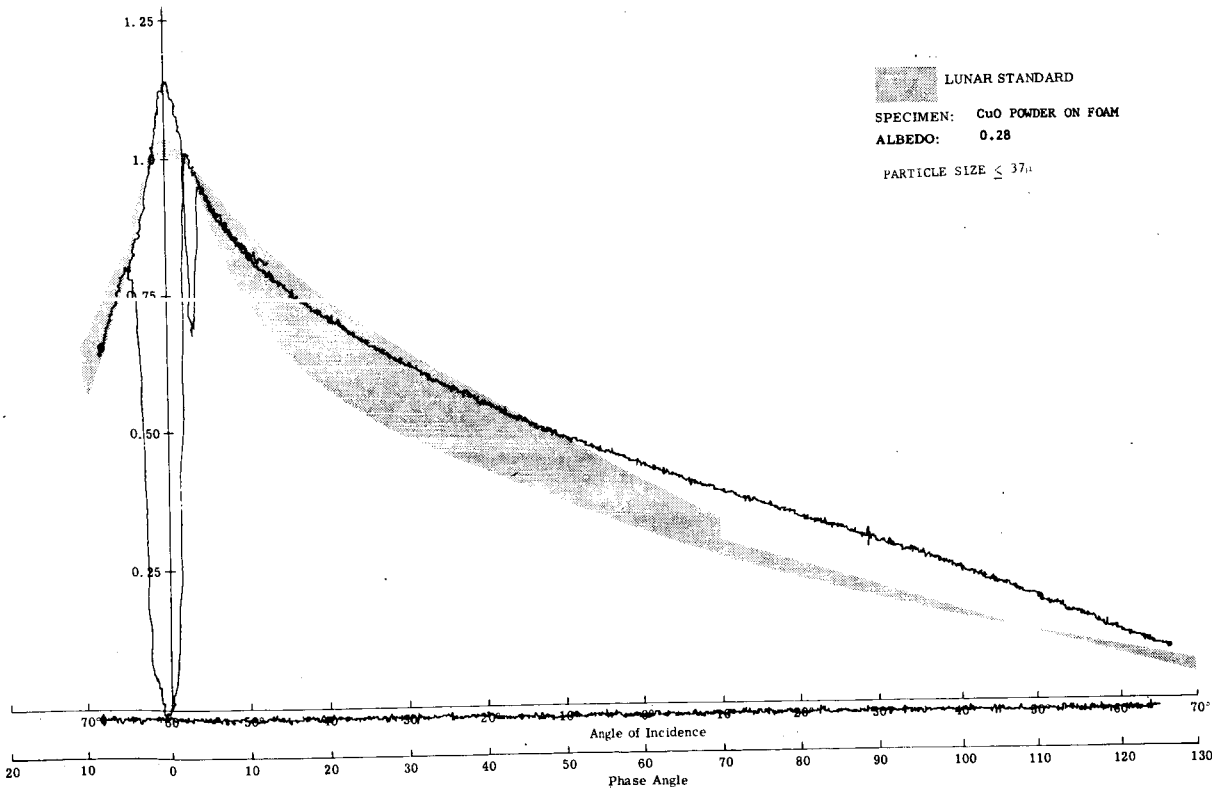
Fig. 11c Photometry of Copper Oxide Powder on Foam (E = 60°)

E = 60°



Red

E = 60°



Infrared

Fig. 11c (Cont) Photometry of Copper Oxide Powder on Foam (E = 60°)



Fig. 12 Volcanic Cinder No. 4

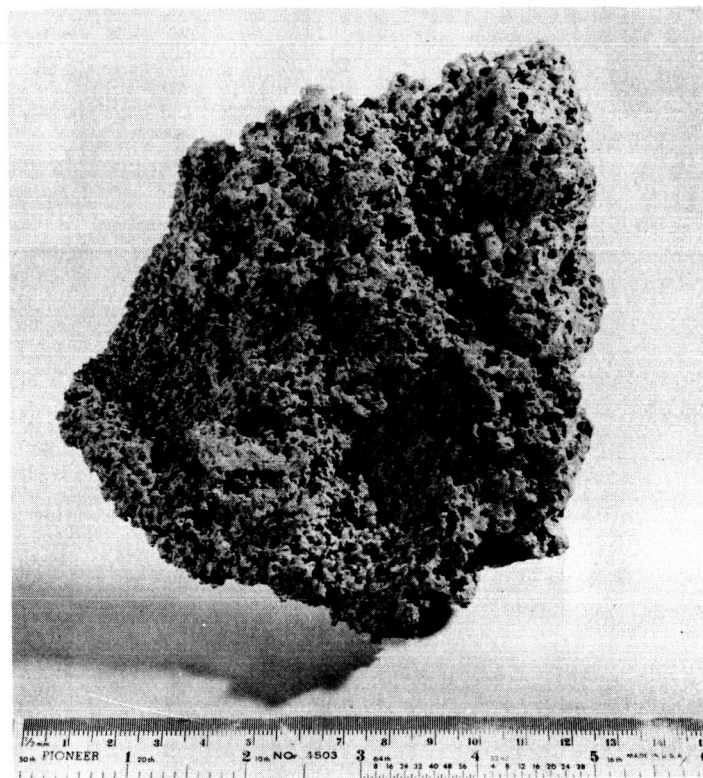


Fig. 13 Furnace Slag No. 1

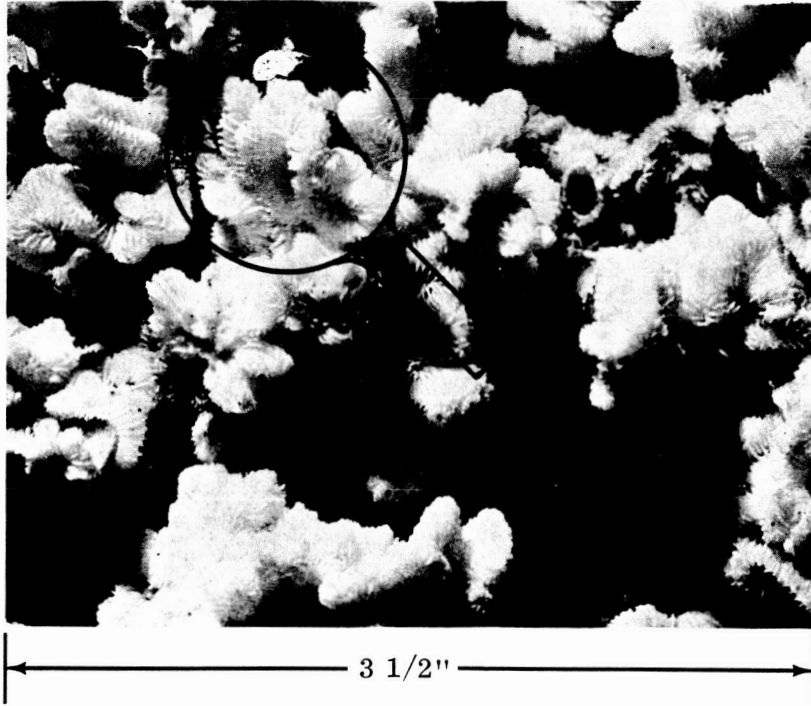


Fig. 14 Coral No. 2

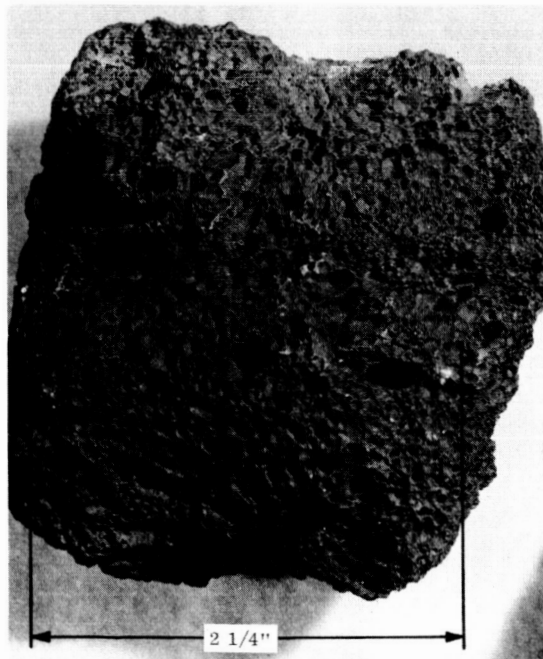


Fig. 15 Scoria No. 2

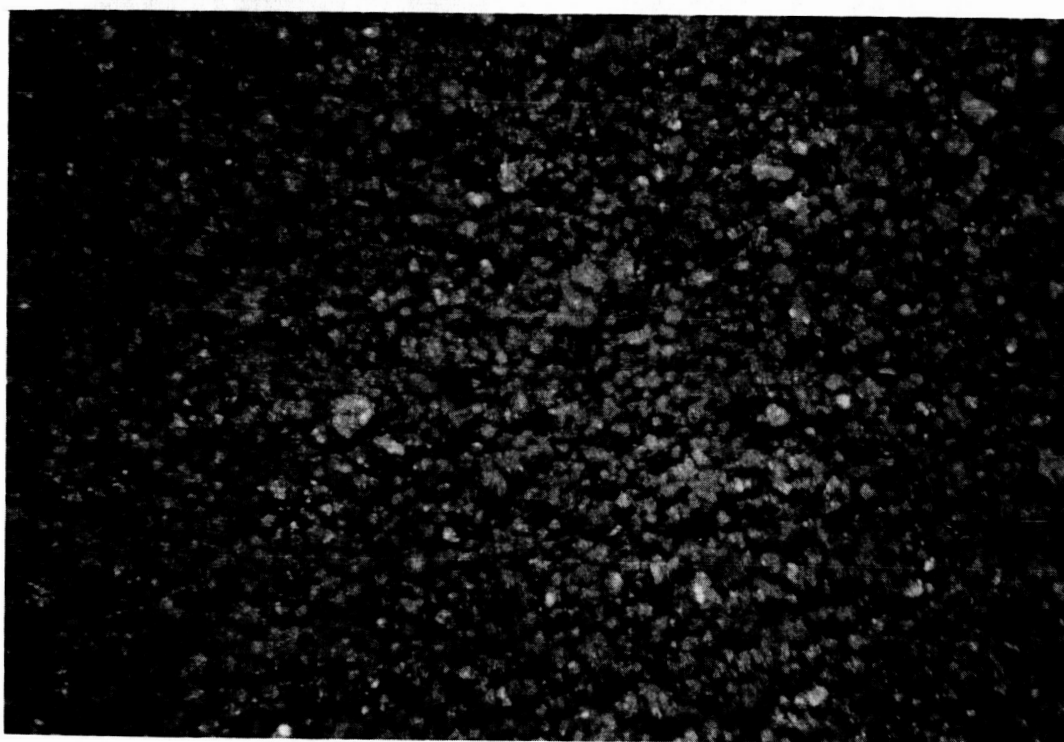


Fig. 16 Copper Oxide (Magnified 25X)





Fig. 17 Copper Oxide on Foam


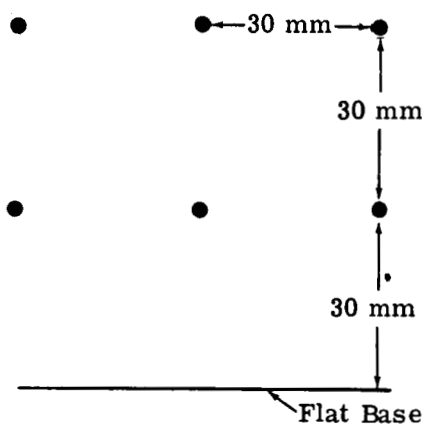
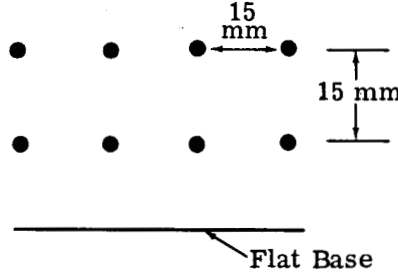
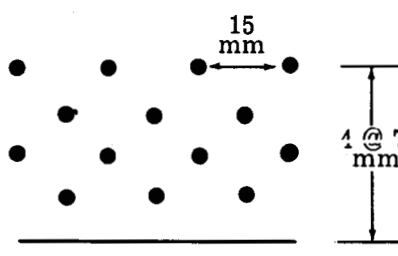
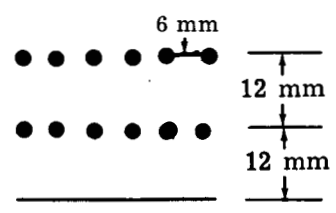
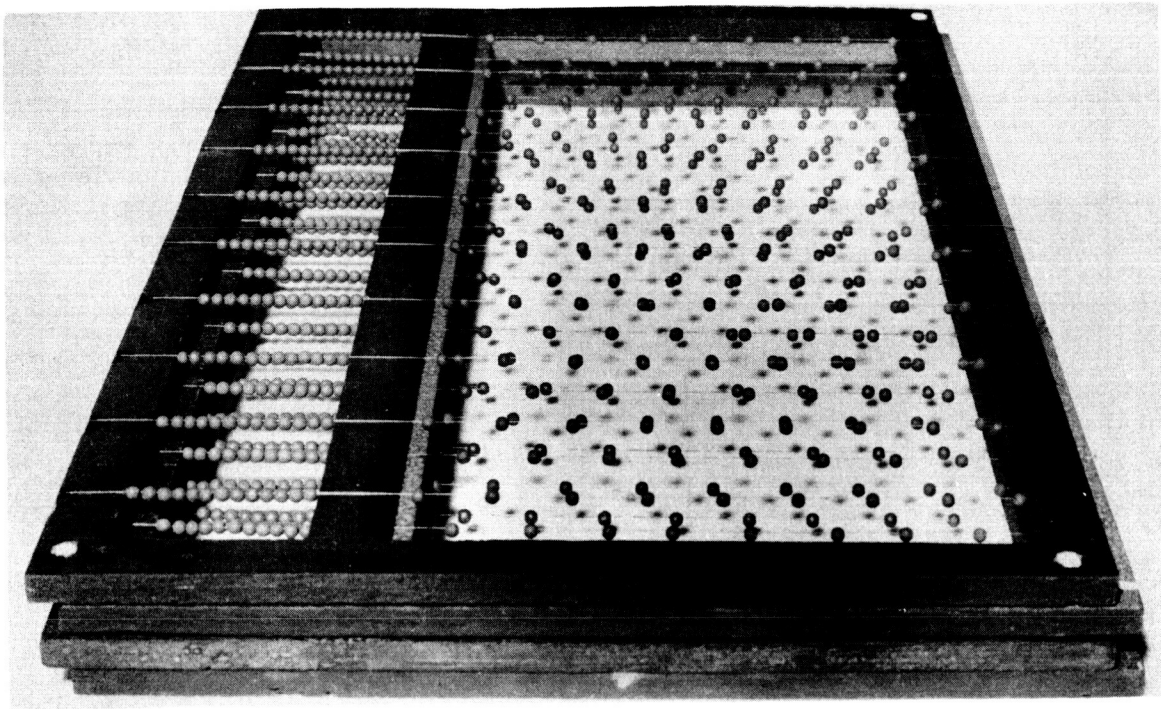
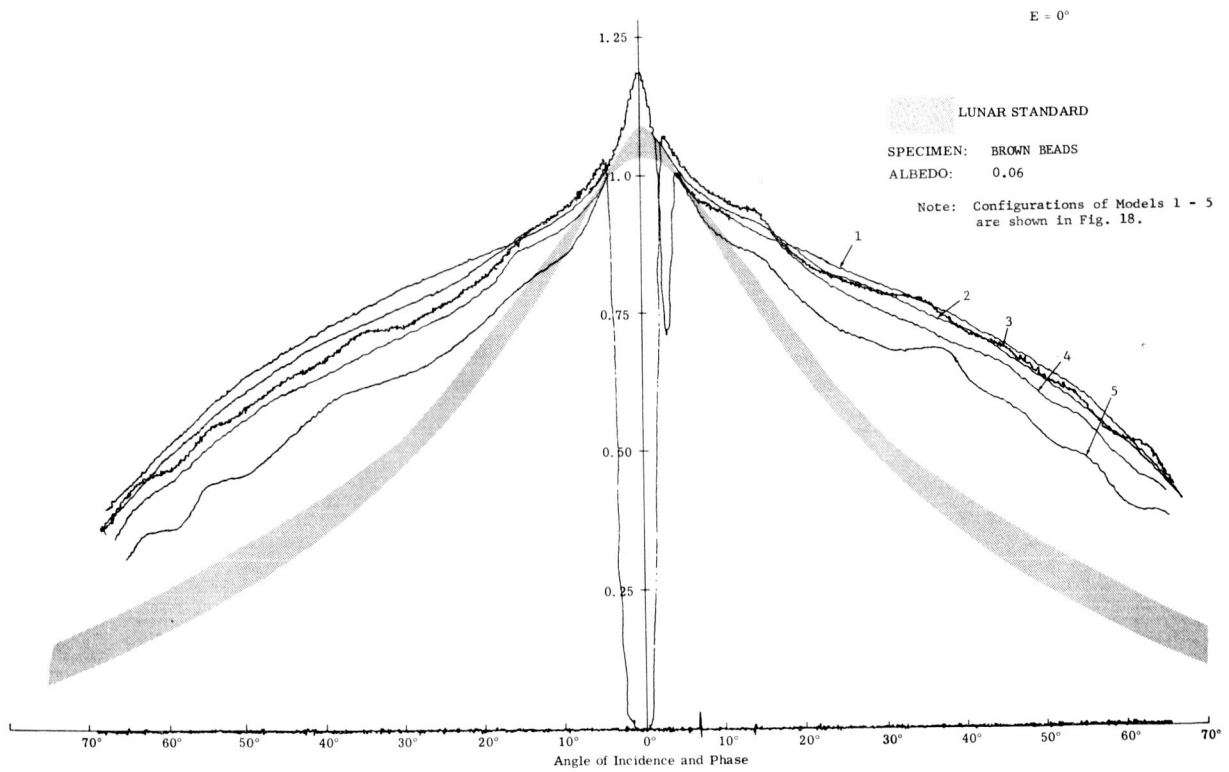
Model No.	Geometry	Particle Spacing to Diameter Ratio	Number of Particles per 30 x 30 mm viewed area
1	 Flat Base	(no particles)	0
2	 Flat Base	10 : 1 in x, y and z directions	2
3	 Flat Base	5 : 1 in x, y and z directions	8
4	 1 @ 7 mm	x = 5:1 y = 5:1 z = 2:1	16
5		x = 2:1 y = 5:1 z = 4:1	20

Fig. 18 Experimental Models of Suspended Particles



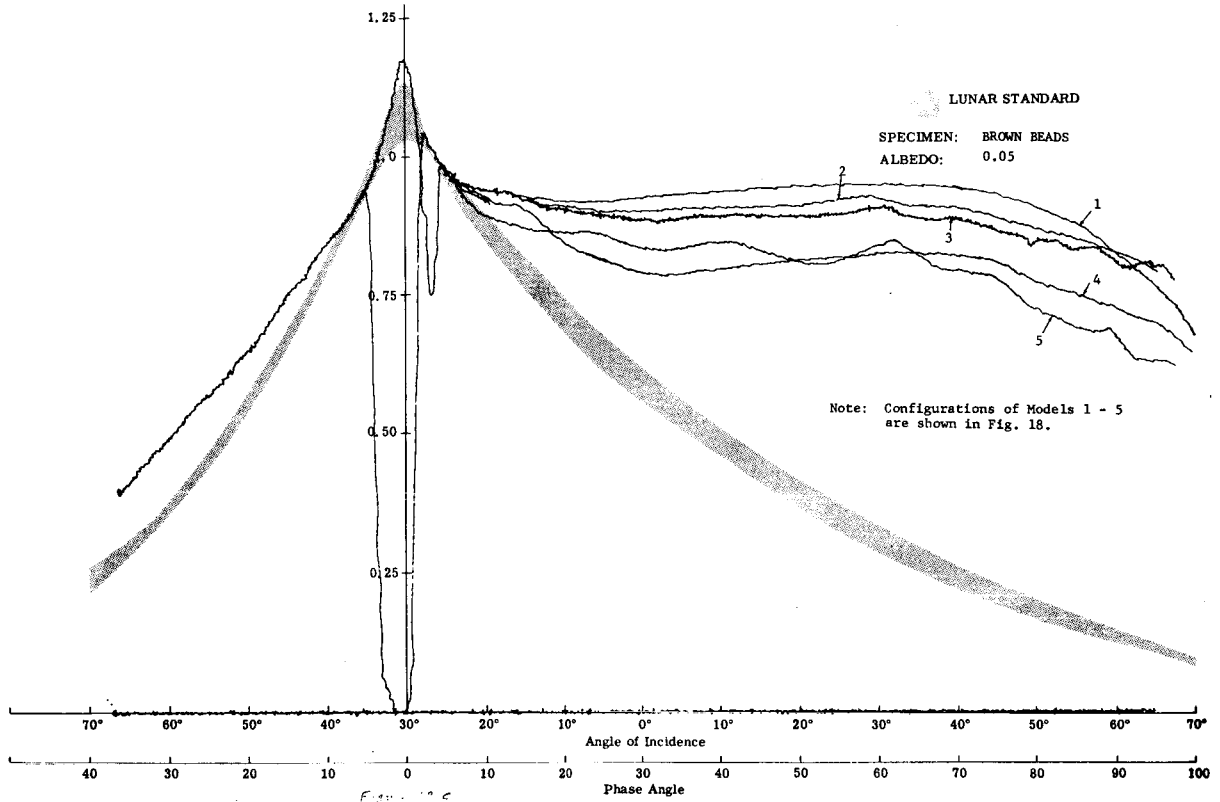
a) Photograph of Brown Beads Model



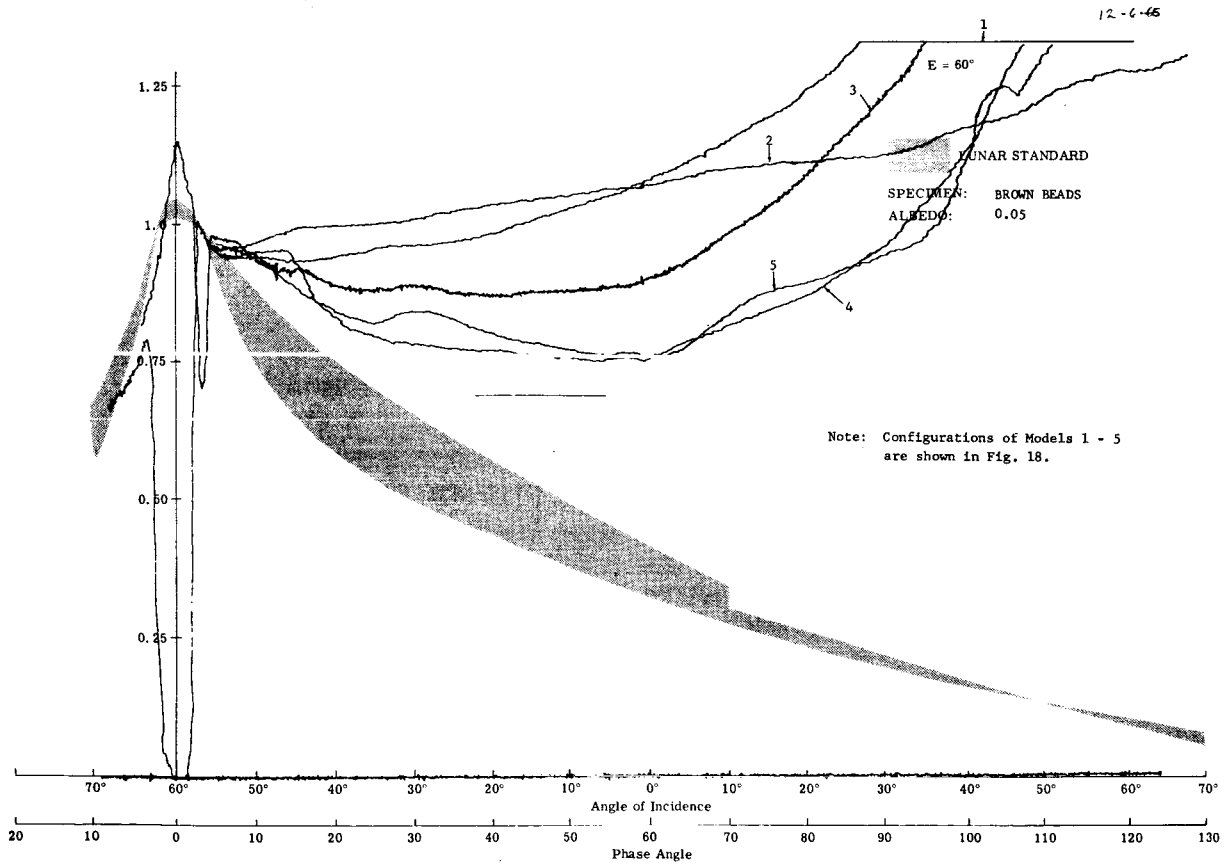
b) E = 0°

Fig. 19 Photometry of Suspended Particles Model

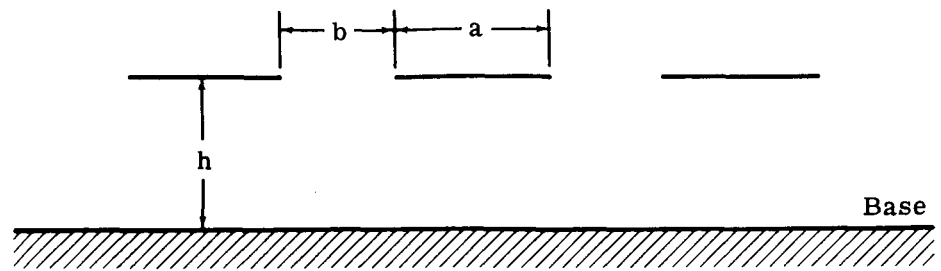
E = 30°



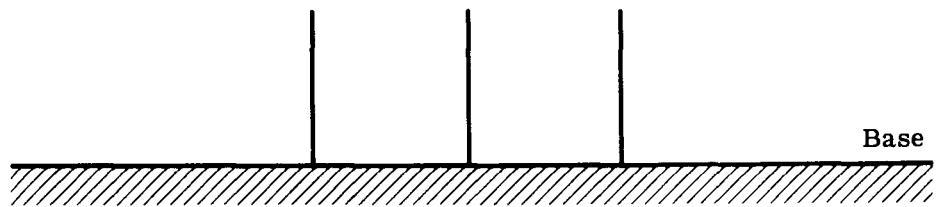
c) E = 30°



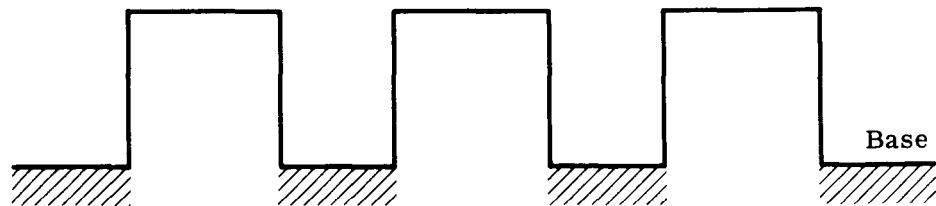
d) E = 60°



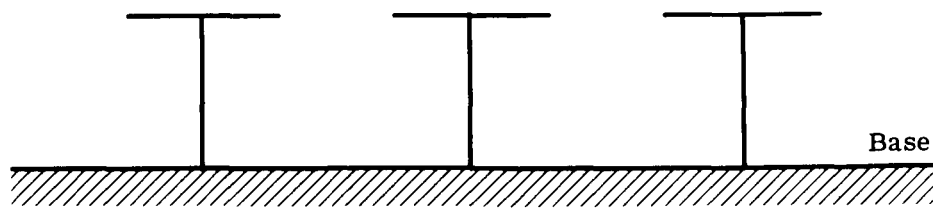
a) Suspended Strip Model



b) Vertical Strip Model



c) Furrow Model



d) T-Model

Fig. 20 Geometry of Four Contrived Photometric Models

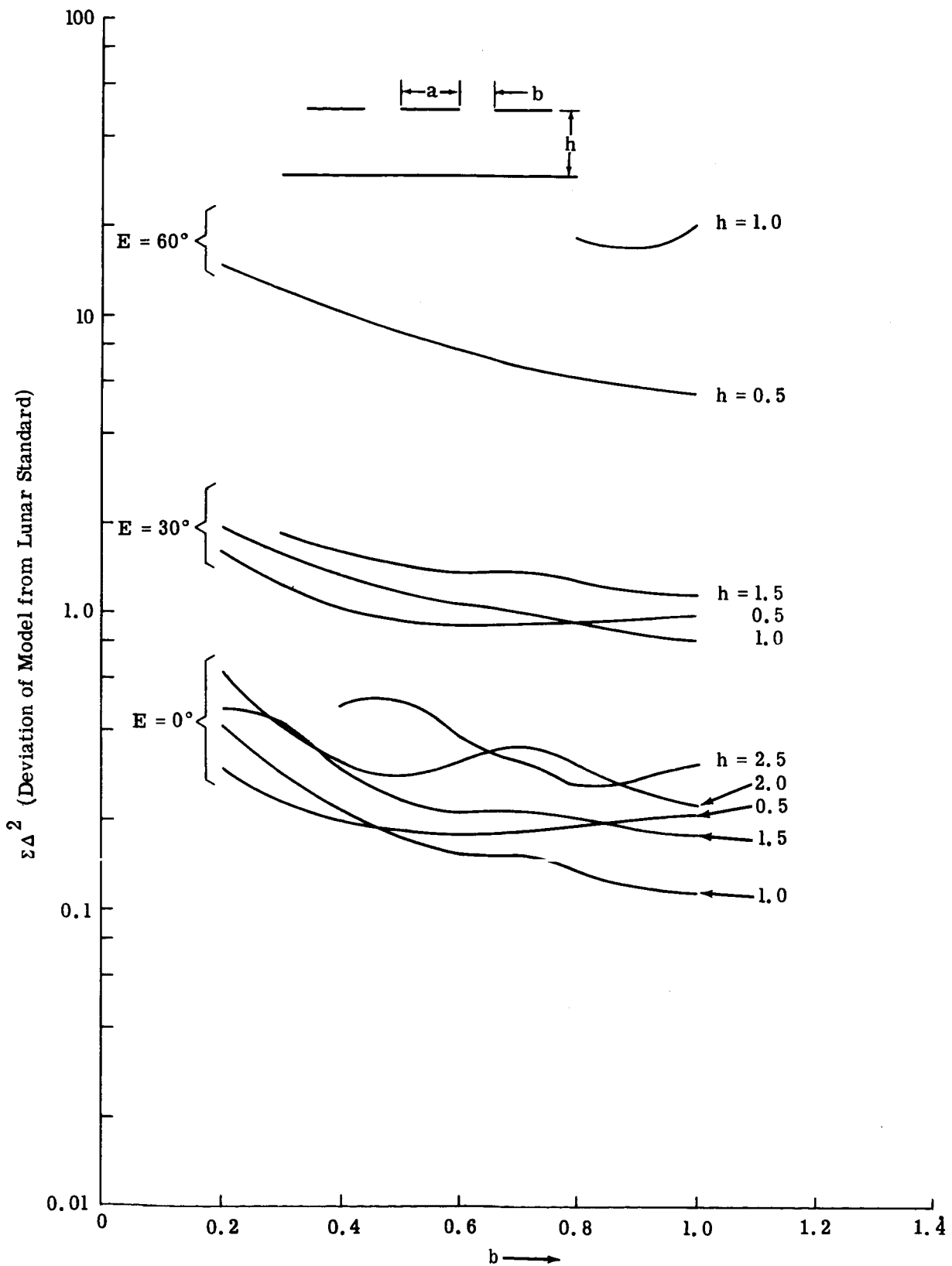


Fig. 21a Extent of Moon-Model Photometric Deviations - Suspended Strip Model

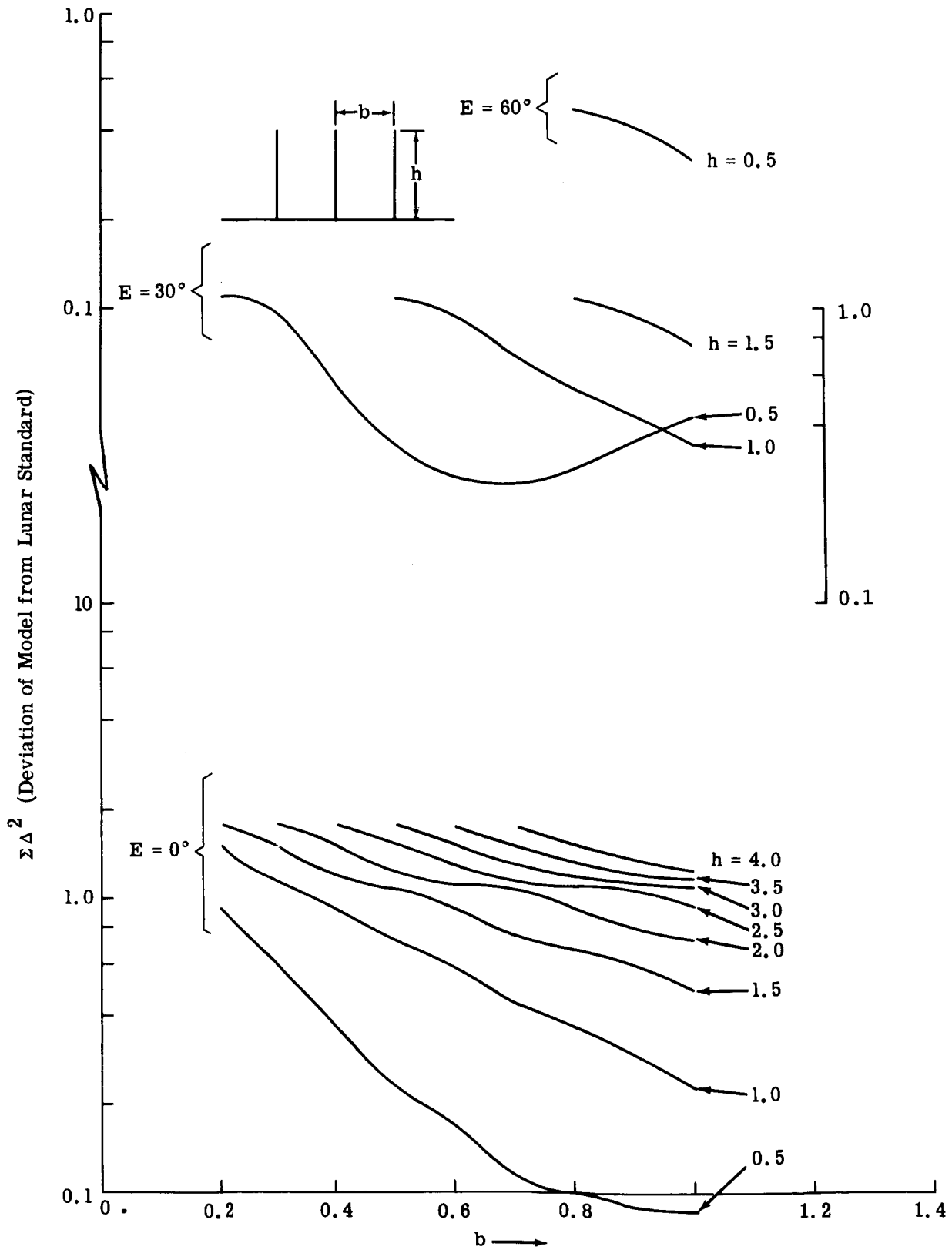


Fig. 21b Extent of Moon-Model Photometric Deviations - Vertical Strip Model

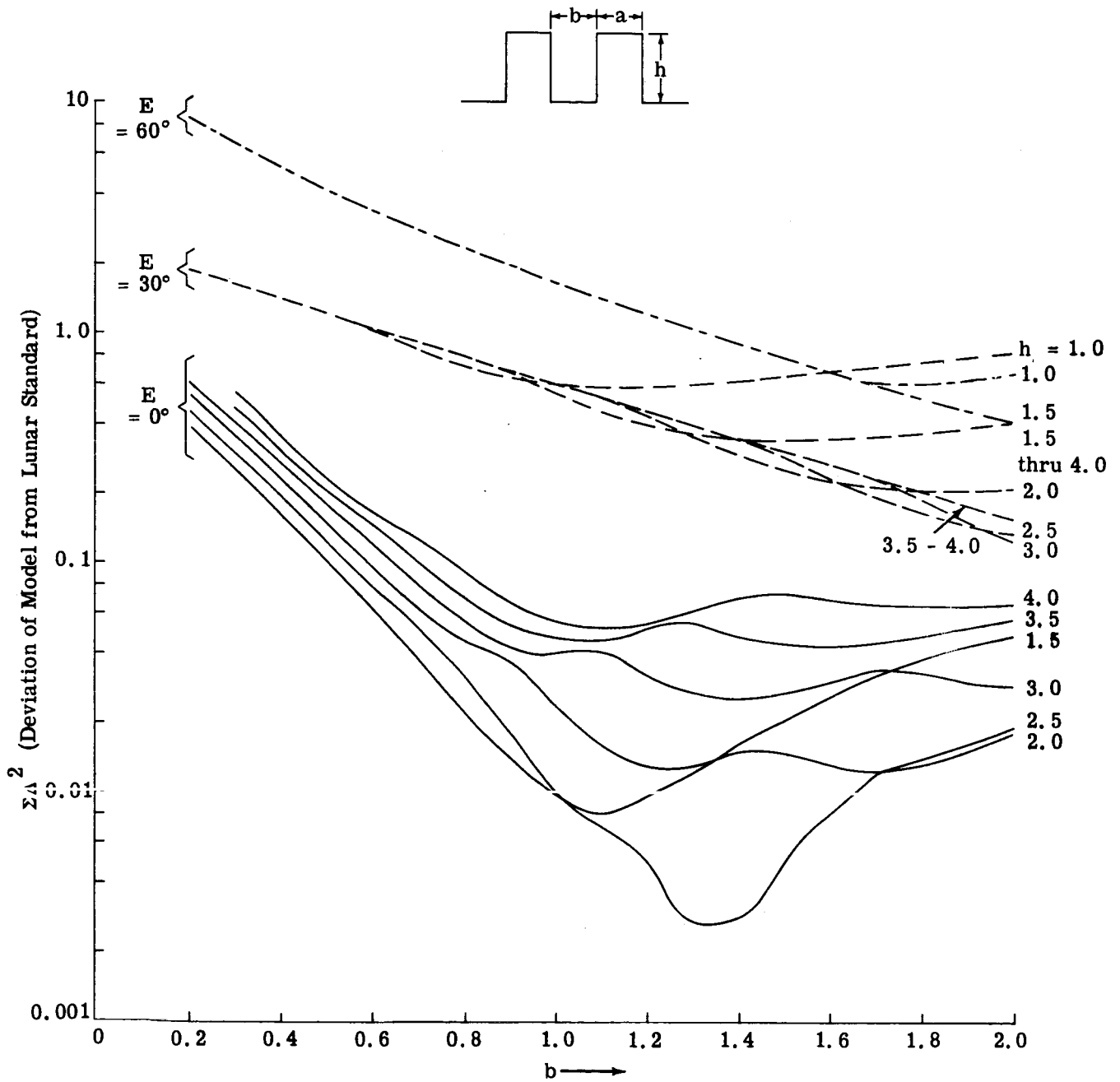


Fig. 21c Extent of Moon-Model Photometric Deviations - Furrow Model



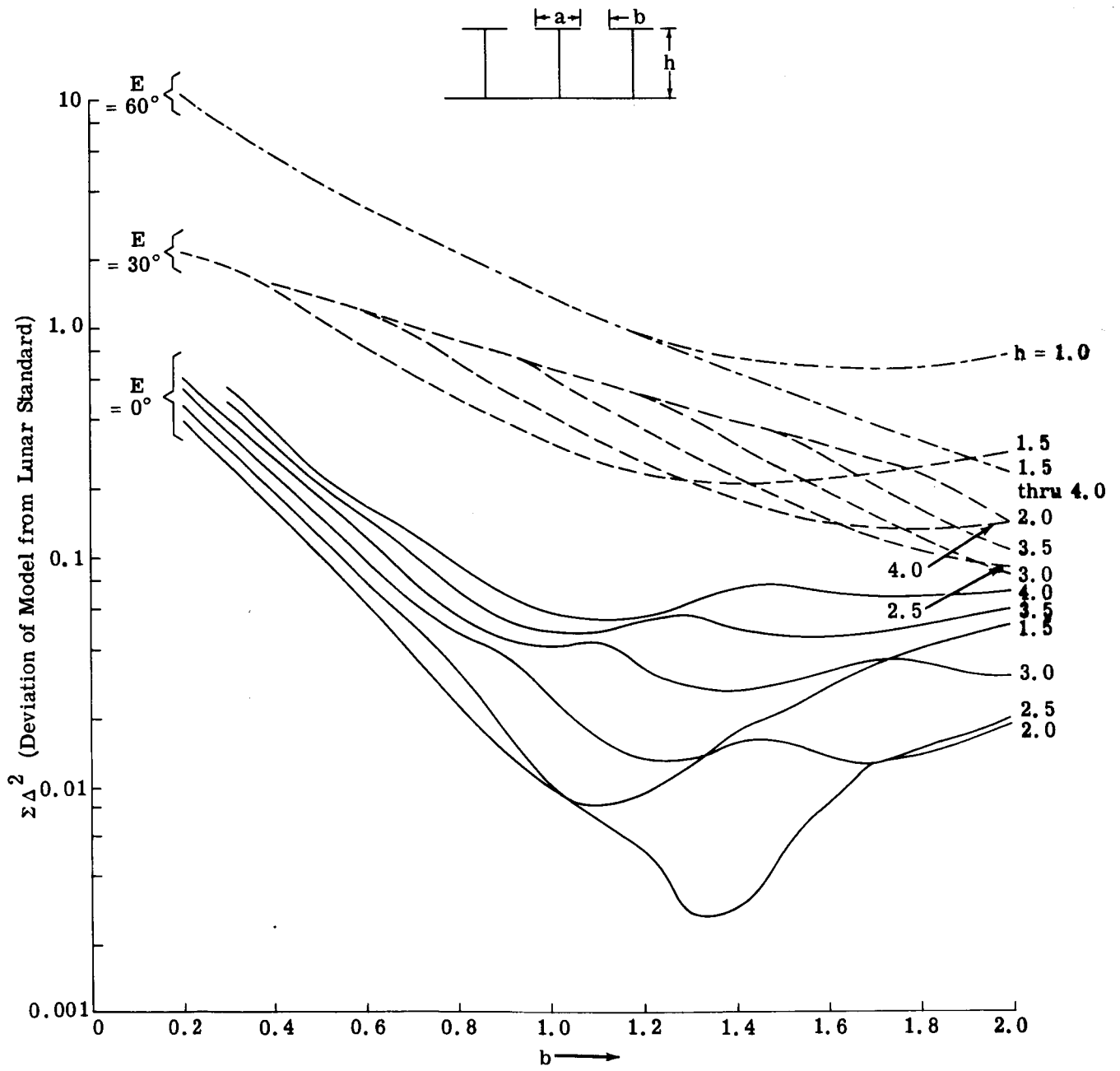


Fig. 21d Extent of Moon-Model Photometric Deviations - T-Model

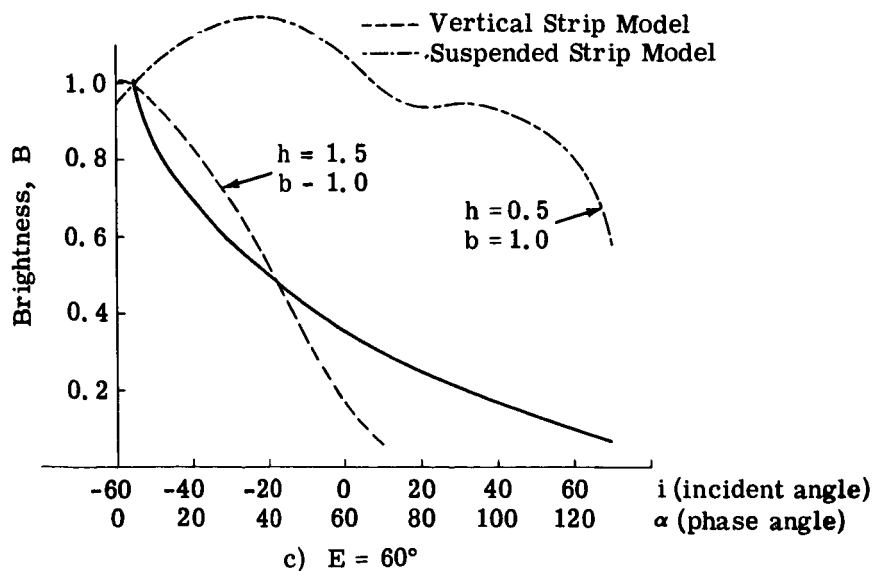
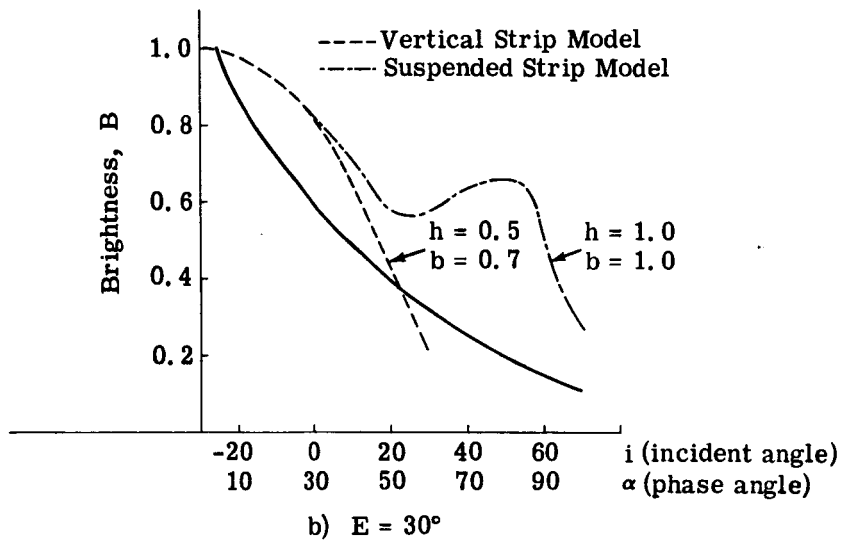
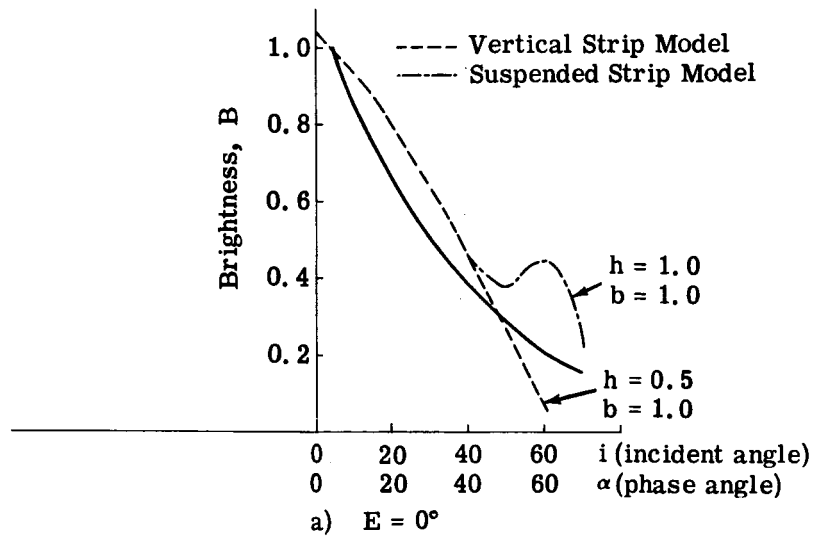


Fig. 22. Photometry of Vertical and Suspended Strip Models

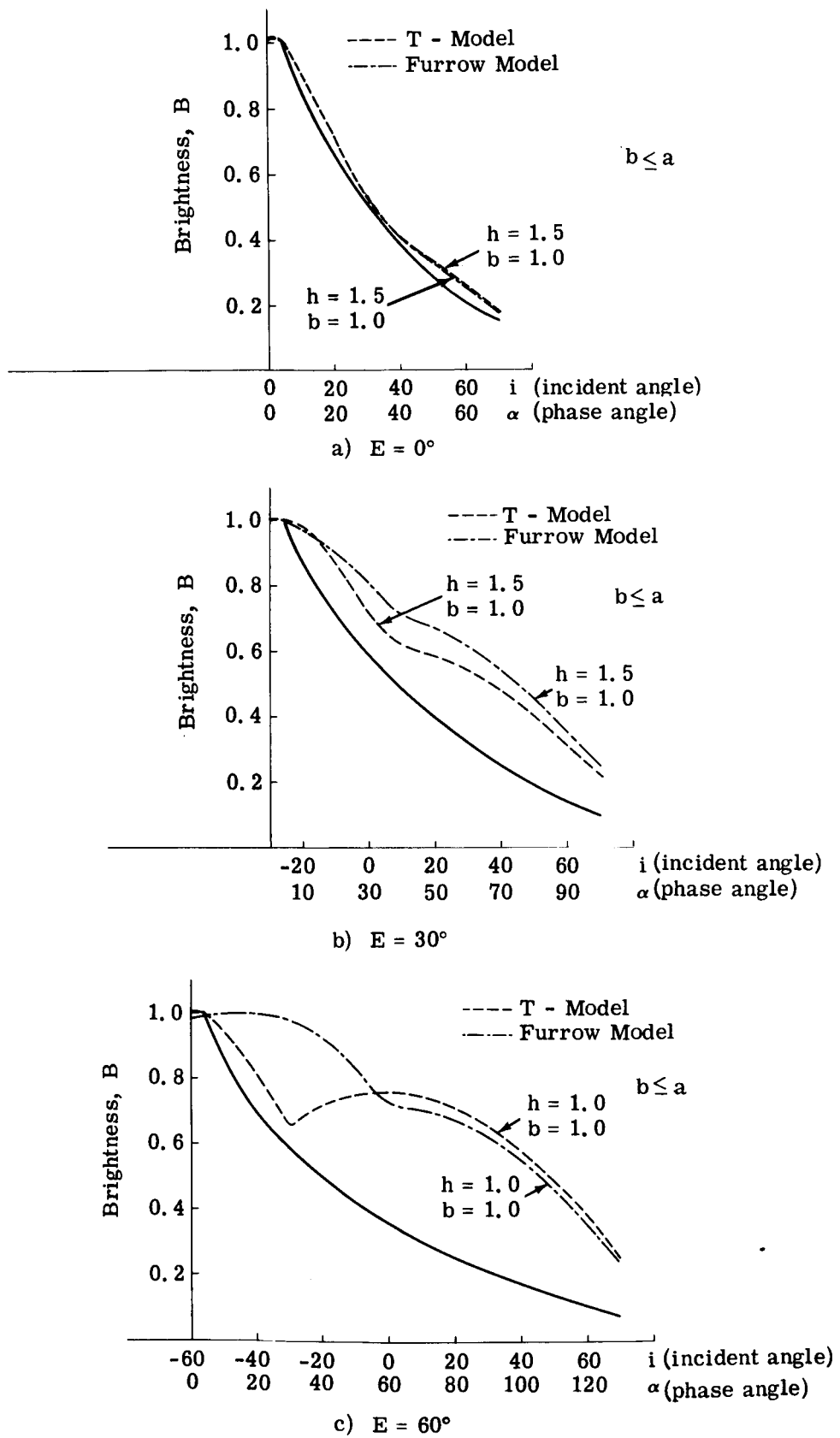
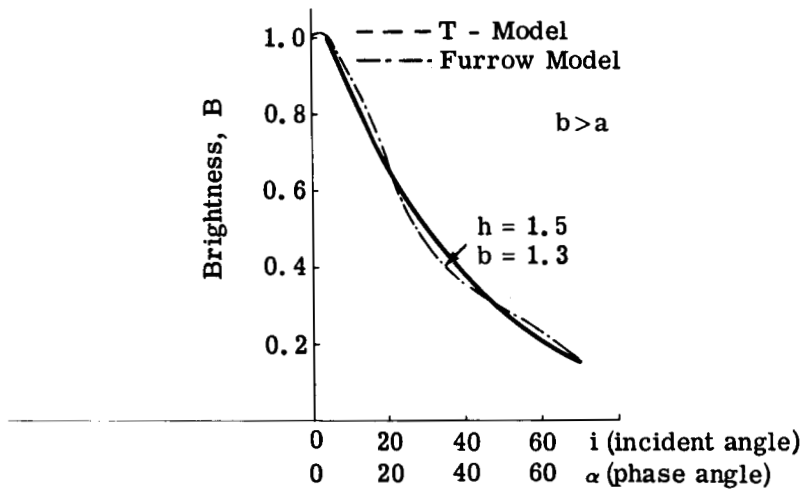
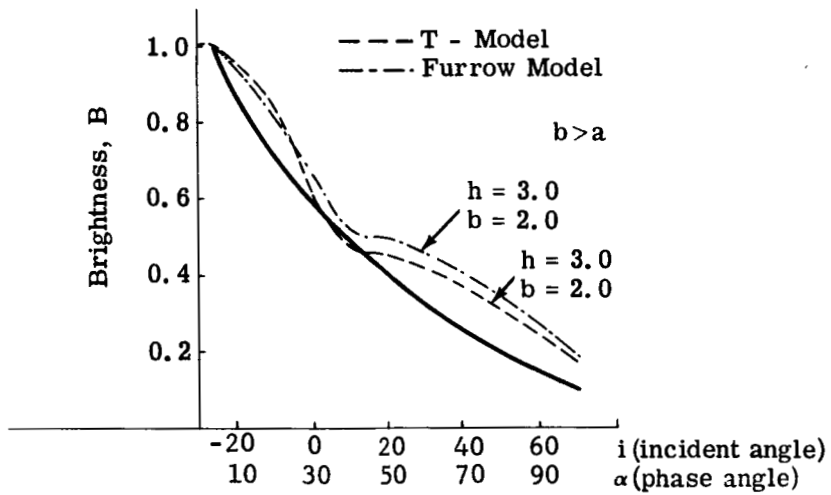


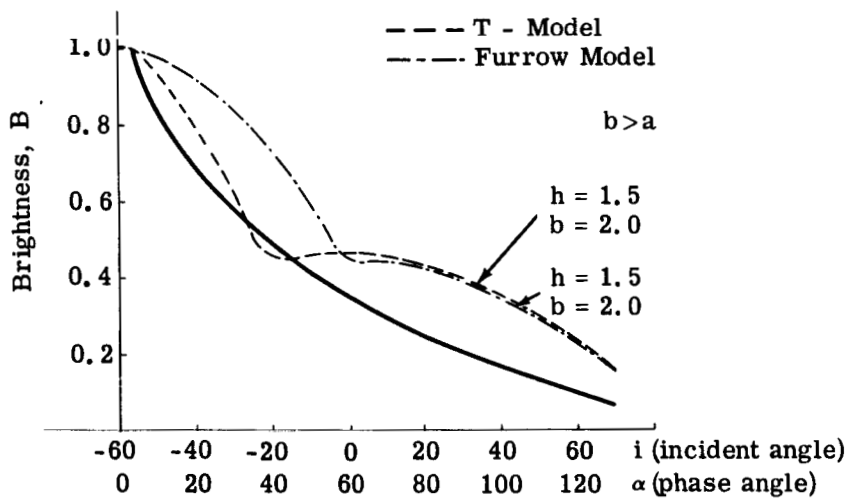
Fig. 23. Photometry of T and Furrow Models ( $b \leq a$ )



a)  $E = 0^\circ$



b)  $E = 30^\circ$



c)  $E = 60^\circ$

Fig. 24 Photometry of T and Furrow Models  
( $b > a$ )

## APPENDIX

### List of Symbols

- a = length of horizontal elements
- b = length of opening between horizontal and/or vertical elements
- B = computed brightness
- c = length of elements in direction perpendicular to intensity equator
- E = viewing angle of photometer
- h = length of vertical elements
- i = angle of incidence of illumination
- K = normalization constant
- $\rho_A$  = average reflectivity of horizontal elements
- $\rho_B$  = average reflectivity of base material
- $\rho_V$  = average reflectivity of vertical elements

## Discussion of Computer Program

Utilizing the four "simple" geometric configurations described in the section on analytical models, a computer program was written, based upon the geometrical analyses given in this Appendix.

The mathematical logic of the program is straightforward and can be described briefly as follows:

For all models, more than one case (A, B, C, etc.) is presented, each being defined by the viewing angle  $E$ , and particular combinations of the linear elements  $a$ ,  $b$ , and  $h$ . For all cases, the brightness,  $B$ , expressed as a product of a particular form of optical scattering law (in this case Lambert's law of diffuse reflection), and a surface area that is both illuminated and viewed by the photometer, is given alongside the corresponding region of validity defined by the boundary conditions on the angle of incidence,  $i$ . As can be readily observed, the complete interval on  $i$  extends from the photometer position,  $E$ , to a value of  $i$  approaching  $+90^\circ$  in most cases, corresponding to a motion of the source from left to right along the intensity equator.

As written in the present analysis, the relationships are valid for values of  $b \leq a$ . In the case of the "T" and Furrow models however, they are extended to include cases for which  $b > a$ .

For a given set of input parameters for each model, namely  $a$ ,  $b$ , and  $h$ , the computer determines for a particular viewing angle ( $0^\circ$ ,  $30^\circ$ , or  $60^\circ$ ) the case and consequently which set of equations it shall use to compute the called-for information. The results desired in the present instance are: 1) the normalized brightness versus phase curves for all models, viewing angles, and possible combinations of linear elements prescribed in the input data; and 2) the computation of the sum of the squares of the deviations (computed at regular predetermined values of the phase angle) between the normalized photometric curves determined in 1), and those of the actual lunation curves of the moon. Expressed mathematically, the latter sum can be written as:

$$(\Sigma \Delta^2) = \sum_{i=i_0}^{i=70^\circ} \left| B_{L_i} - B_{C_i} \right|^2 ,$$

where  $B_L$  and  $B_C$  represent the lunar and contrived model brightnesses respectively, and the summation indices run from a value of  $i = i_0$  (corresponding to a phase angle,  $\alpha = |E| + i$ , equal to  $4^\circ$ ), to a value of  $i = 70^\circ$ , which is the largest angle of incidence for which the standard lunation curves are given. Information on the  $B_L$ 's (lunar brightnesses) for all three viewing angles were taken from Ref. 2 and introduced numerically into the program as input. Because the brightness curves for the moon are already normalized to correspond to a value of one at  $4^\circ$  phase angle, the curves computed in 1, and later used for comparison with the lunar data in 2, had also to be normalized at the same phase angle before any meaningful interpretation could be given to them. The latter was accomplished by the use of a subroutine, utilizing the normalization factor,  $K$ , which had to be evaluated for all combinations of input data. In addition to the parameters already mentioned as input data, values of  $c$  (length of elements in direction perpendicular to intensity equator),  $\rho_A$ ,  $\rho_B$ , and  $\rho_V$  (average reflectivity values) were selected. A brief summary of all the input information (excluding input data on the lunation curves) is given in Table 2, which also shows the minimum, maximum and incremental values of all the linear elements.

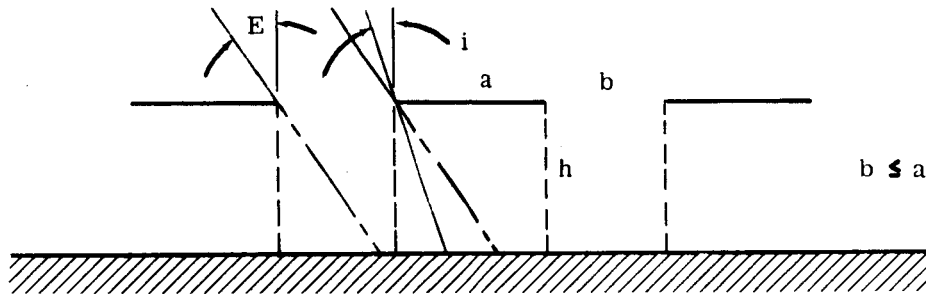
Table 2

SUMMARY OF INPUT DATA

Linear Element	Average Reflectivity	Minimum	Maximum	Increment
a	= .1	1	1	0
b		.1a	1.0a	.1a
h	= .1	.5a	4.0a	.5a
c	-----	1	1	0
Base Material	= .1	-----	-----	-----

Photogeometric Analysis of Contrived Models

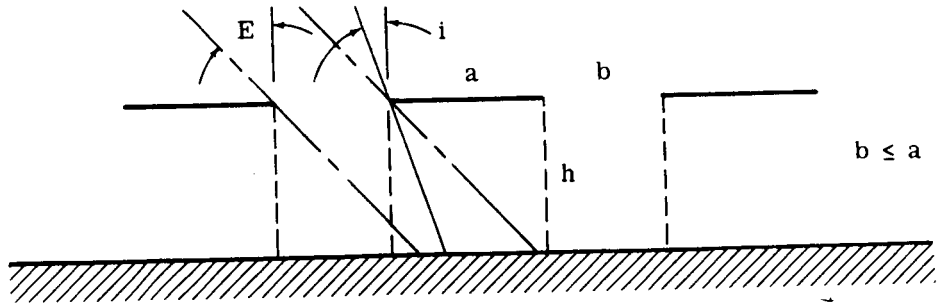
SUSPENDED STRIP MODEL



Case A:  $\text{Tan}^{-1}(0) \leq E \leq \text{Tan}^{-1}\left(\frac{b}{h}\right)$

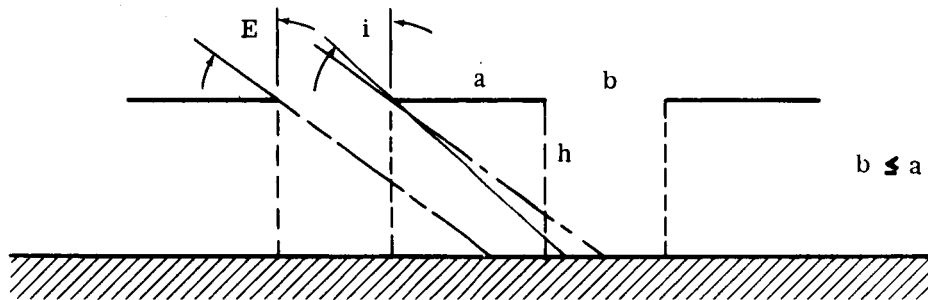
Boundary Condition on $i$ :	Brightness, $B$
$-E \leq i \leq \tan^{-1}\left(\frac{b-h \tan E}{h}\right)$	$K \cos  i  \cos E \left[ \rho_A a + \rho_B (b - h \tan E - h \tan i) \right] c$
$\tan^{-1}\left(\frac{b-h \tan E}{h}\right) \leq i \leq \tan^{-1}\left(\frac{a-h \tan E}{h}\right)$	$K \cos  i  \cos E (\rho_A a) c$
$\tan^{-1}\left(\frac{a-h \tan E}{h}\right) \leq i \leq \tan^{-1}\left(\frac{a+b-h \tan E}{h}\right)$	$K \cos  i  \cos E \left[ \rho_A a + \rho_B (h \tan i - a + h \tan E) \right] c$
$\tan^{-1}\left(\frac{a+b-h \tan E}{h}\right) \leq i \leq \tan^{-1}\left(\frac{a+2b-h \tan E}{h}\right)$	$K \cos  i  \cos E \left[ \rho_A a + \rho_B (a + 2b - h \tan E - h \tan i) \right] c$
$\tan^{-1}\left(\frac{a+2b-h \tan E}{h}\right) \leq i \leq \tan^{-1}\left(\frac{2a+b-h \tan E}{h}\right)$	$K \cos  i  \cos E (\rho_A a) c$
$\tan^{-1}\left(\frac{2a+b-h \tan E}{h}\right) \leq i \leq \tan^{-1}\left(\frac{2a+2b-h \tan E}{h}\right)$	$K \cos  i  \cos E \left[ \rho_A a + \rho_B (h \tan i - (2a + b - h \tan E)) \right] c$
$\tan^{-1}\left(\frac{2a+2b-h \tan E}{h}\right) \leq i \leq \tan^{-1}\left(\frac{2a+3b-h \tan E}{h}\right)$	$K \cos  i  \cos E \left[ \rho_A a + \rho_B ((2a + 3b - h \tan E) - h \tan i) \right] c$
$i = \frac{\pi}{2}$	0





Case B:  $\tan^{-1}\left(\frac{b}{h}\right) \leq E \leq \tan^{-1}\left(\frac{a}{h}\right)$

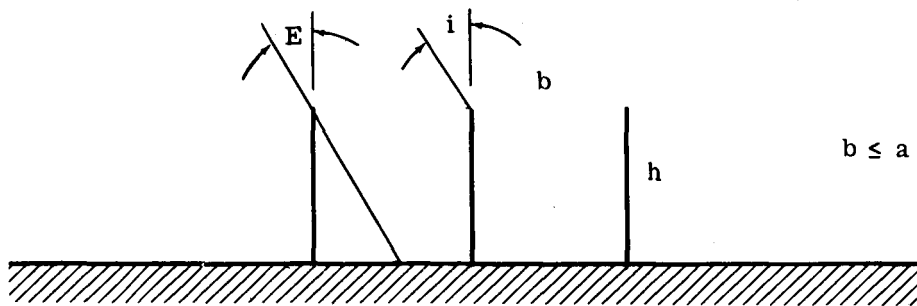
Boundary Condition on $i$ :	Brightness, $B$
$-E \leq i \leq -\tan^{-1}\left(\frac{h \tan E - b}{h}\right)$	$K \cos  i  \cos E \left[ \rho_A a + \rho_B (h \tan  i  - h \tan E + b) \right] c$
$-\tan^{-1}\left(\frac{h \tan E - b}{h}\right) \leq i \leq \tan^{-1}\left(\frac{a - h \tan E}{h}\right)$	$K \cos  i  \cos E (\rho_A a) c$
$\tan^{-1}\left(\frac{a - h \tan E}{h}\right) \leq i \leq \tan^{-1}\left(\frac{a - h \tan E + b}{h}\right)$	$K \cos  i  \cos E \left[ \rho_A a + \rho_B (h \tan i - (a - h \tan E)) \right] c$
$\tan^{-1}\left(\frac{a - h \tan E + b}{h}\right) \leq i \leq \tan^{-1}\left(\frac{a + 2b - h \tan E}{h}\right)$	$K \cos  i  \cos E \left[ \rho_A a + \rho_B (a + 2b - h \tan E - h \tan i) \right] c$
$\tan^{-1}\left(\frac{a + 2b - h \tan E}{h}\right) \leq i \leq \tan^{-1}\left(\frac{2a + b - h \tan E}{h}\right)$	$K \cos  i  \cos E (\rho_A a) c$
$\tan^{-1}\left(\frac{2a + b - h \tan E}{h}\right) \leq i \leq \tan^{-1}\left(\frac{2a + 2b - h \tan E}{h}\right)$	$K \cos  i  \cos E \left[ \rho_A a + \rho_B (h \tan i - (2a + b - h \tan E)) \right] c$
$\tan^{-1}\left(\frac{2a + 2b - h \tan E}{h}\right) \leq i \leq \tan^{-1}\left(\frac{2a + 3b - h \tan E}{h}\right)$	$K \cos  i  \cos E \left[ \rho_A a + \rho_B ((2a + 3b - h \tan E) - h \tan i) \right] c$
$i = \frac{\pi}{2}$	0



Case C:  $\tan^{-1}\left(\frac{a}{h}\right) \leq E \leq \tan^{-1}\left(\frac{a+b}{h}\right)$

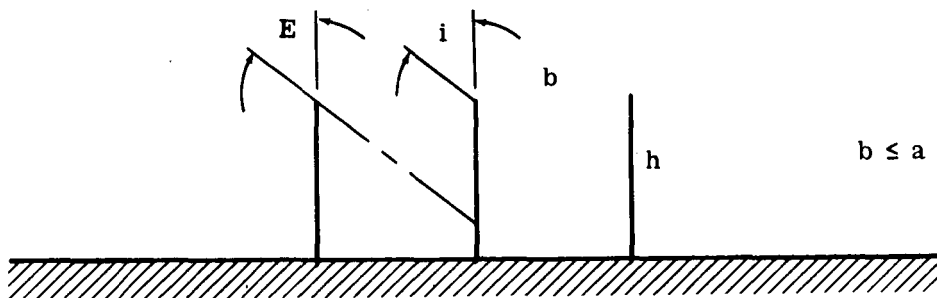
Boundary Condition on $i$ :	Brightness, $E$
$-E \leq i \leq -\tan^{-1}\left(\frac{h \tan E - b}{h}\right)$	$K \cos  i  \cos E \left[ \rho_A a + \rho_B (h \tan  i  - (h \tan E - b)) \right] c$
$-\tan^{-1}\left(\frac{h \tan E - b}{h}\right) \leq i \leq -\tan^{-1}\left(\frac{h \tan E - a}{h}\right)$	$K \cos  i  \cos E (\rho_A a) c$
$-\tan^{-1}\left(\frac{h \tan E - a}{h}\right) \leq i \leq \tan^{-1}(0)$	$K \cos  i  \cos E \left[ \rho_A a + \rho_B (h \tan E - a) - h \tan  i  \right] c$
$\tan^{-1}(0) \leq i \leq \tan^{-1}\left(\frac{a+b-h \tan E}{h}\right)$	$K \cos  i  \cos E \left[ \rho_A a + \rho_B (a + (h \tan E - a) + h \tan  i ) \right] c$
$\tan^{-1}\left(\frac{a+b-h \tan E}{h}\right) \leq i \leq \tan^{-1}\left(\frac{a+2b-h \tan E}{h}\right)$	$K \cos  i  \cos E \left[ \rho_A a + \rho_B (a + 2b - h \tan E - h \tan  i ) \right] c$
$\tan^{-1}\left(\frac{a+2b-h \tan E}{h}\right) \leq i \leq \tan^{-1}\left(\frac{2a+b-h \tan E}{h}\right)$	$K \cos  i  \cos E (\rho_A a) c$
$\tan^{-1}\left(\frac{2a+b-h \tan E}{h}\right) \leq i \leq \tan^{-1}\left(\frac{2a+2b-h \tan E}{h}\right)$	$K \cos  i  \cos E \left[ \rho_A a + \rho_B (h \tan  i  - (2a + b - h \tan E)) \right] c$
$\tan^{-1}\left(\frac{2a+2b-h \tan E}{h}\right) \leq i \leq \tan^{-1}\left(\frac{2a+3b-h \tan E}{h}\right)$	$K \cos  i  \cos E \left[ \rho_A a + \rho_B ((2a + 3b - h \tan E) - h \tan  i ) \right] c$
$i = \frac{\pi}{2}$	0

# VERTICAL STRIP MODEL



Case A:  $\tan^{-1}(0) \leq E \leq \tan^{-1}\left(\frac{b}{h}\right)$

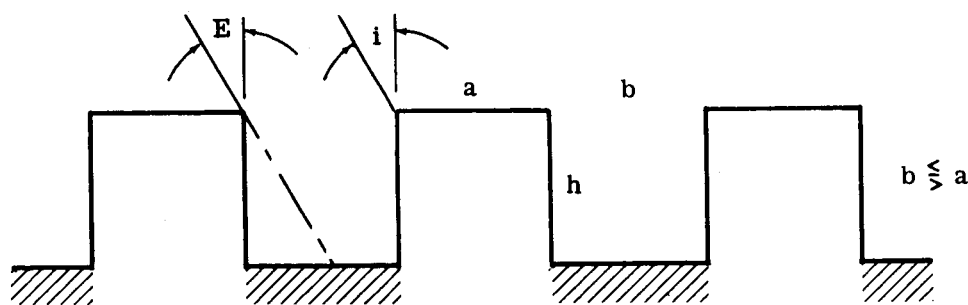
Boundary Condition on $i$ :	Brightness, $B$
$-E \leq i \leq \tan^{-1}(0)$	$K \left\{ \cos  i  \cos E \cdot \rho_B (b - h \tan E) + \rho_V \cos\left(\frac{\pi}{2} -  i \right) \cos\left(\frac{\pi}{2} - E\right) h \right\} c$
$\tan^{-1}(0) \leq i \leq \tan^{-1}\left(\frac{b - h \tan E}{h}\right)$	$K \cos  i  \cos E \cdot \rho_B [(b - h \tan E) - h \tan i] c$
$\tan^{-1}\left(\frac{b - h \tan E}{h}\right) \leq i$	0



Case B:  $\tan^{-1}\left(\frac{b}{h}\right) \leq E$

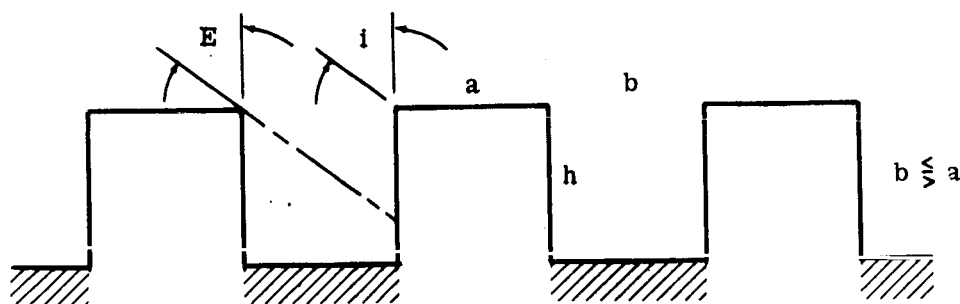
Boundary Condition on $i$ :	Brightness, $B$
$-E \leq i \leq \tan^{-1}(0)$	$K \left[ \cos\left(\frac{\pi}{2} -  i \right) \cos\left(\frac{\pi}{2} - E\right) \cdot \rho_V \left(\frac{b}{\tan E}\right) \right] c$
$\tan^{-1}(0) \leq i$	0

# FURROW MODEL



Case A:  $\tan^{-1}(0) \leq E \leq \tan^{-1}\left(\frac{b}{h}\right)$

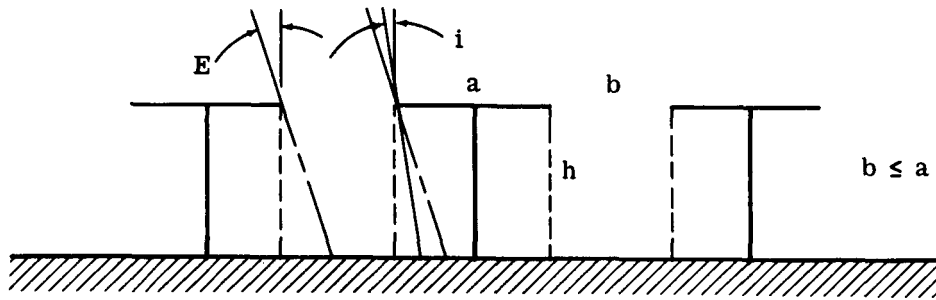
Boundary Condition on $i$ :	Brightness, $B$
$-E \leq i \leq \tan^{-1}(0)$	$K \left\{ \cos  i  \cos E \left[ \rho_A a + \rho_B (b - h \tan E) \right] + \rho_V \cos\left(\frac{\pi}{2} -  i \right) \cos\left(\frac{\pi}{2} - E\right) h \right\} c$
$\tan^{-1}(0) \leq i \leq \tan^{-1}\left(\frac{b - h \tan E}{h}\right)$	$K \cos  i  \cos E \left[ \rho_A a + \rho_B (b - h \tan E - h \tan i) \right] c$
$\tan^{-1}\left(\frac{b - h \tan E}{h}\right) \leq i \leq \tan^{-1}(\infty)$	$K \cos  i  \cos E (\rho_A a) c$



Case B:  $\tan^{-1}\left(\frac{b}{h}\right) \leq E$

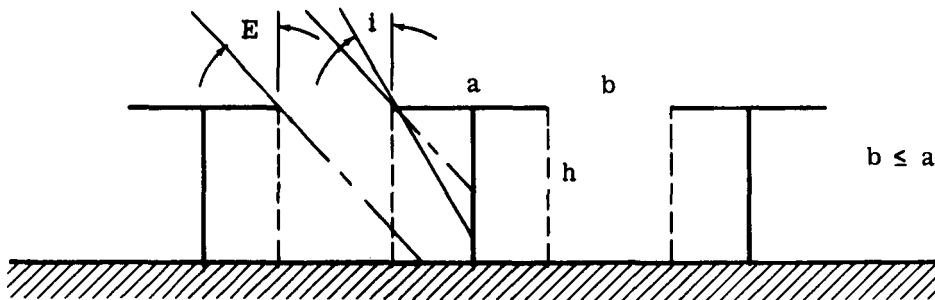
Boundary Condition on $i$ :	Brightness, $B$
$-E \leq i \leq \tan^{-1}(0)$	$K \left\{ \cos  i  \cos E (\rho_A a) + \rho_V \cos\left(\frac{\pi}{2} -  i \right) \cos\left(\frac{\pi}{2} - E\right) \left(\frac{b}{\tan E}\right) \right\} c$
$\tan^{-1}(0) \leq i \leq \tan^{-1}(\infty)$	$K \cos  i  \cos E (\rho_A a) c$

### T-MODEL



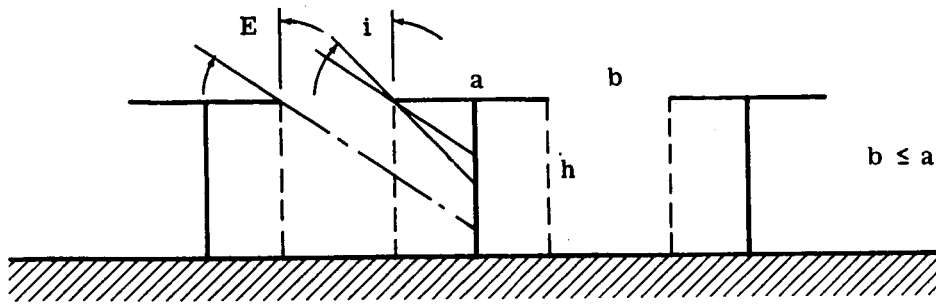
Case A:  $\tan^{-1}(0) \leq E \leq \tan^{-1}\left(\frac{a}{2h}\right)$

Boundary Condition on $i$ :	Brightness, $B$
$-E \leq i \leq \tan^{-1}\left(\frac{b-h \tan E}{h}\right)$	$K \cos  i  \cos E \left[ \rho_A a + \rho_B (b - h \tan E - h \tan i) \right] c$
$\tan^{-1}\left(\frac{b-h \tan E}{h}\right) \leq i \leq \tan^{-1}(a)$	$K \cos  i  \cos E (\rho_A a) c$



Case B:  $\tan^{-1}\left(\frac{a}{2h}\right) \leq E \leq \tan^{-1}\left(\frac{b + \frac{a}{2}}{h}\right)$

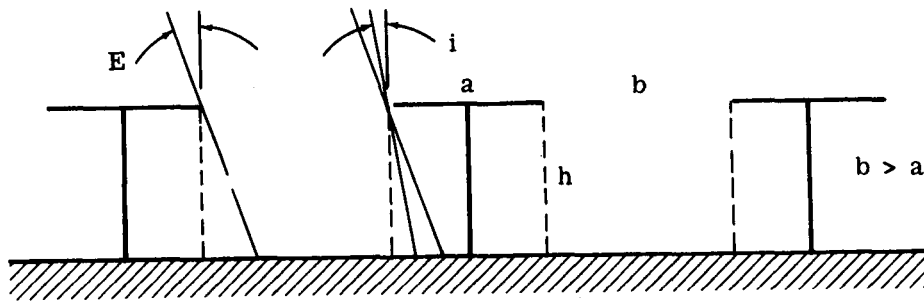
Boundary Condition on $i$ :	Brightness, $B$
$-E \leq i \leq -\tan^{-1}\left(\frac{a}{2h}\right)$	$K \left\{ \cos  i  \cos E \left[ \rho_A a + \rho_B \left( \frac{a}{2} + b - h \tan E \right) \right] + \rho_V \cos\left(\frac{\pi}{2} -  i \right) \cos\left(\frac{\pi}{2} - E\right) \left[ h - \frac{a}{2} \left( \frac{1}{\tan  i } \right) \right] \right\} c$
$-\tan^{-1}\left(\frac{a}{2h}\right) \leq i \leq -\tan^{-1}\left(\frac{h \tan E - b}{h}\right)$	$K \cos  i  \cos E \left[ \rho_A a + \rho_B (h \tan  i  - h \tan E + b) \right] c$
$-\tan^{-1}\left(\frac{h \tan E - b}{h}\right) \leq i \leq \tan^{-1}(a)$	$K \cos  i  \cos E (\rho_A a) c$



Case C:  $\tan^{-1}\left(\frac{b + \frac{a}{2}}{h}\right) \leq E \leq \tan^{-1}(\infty)$

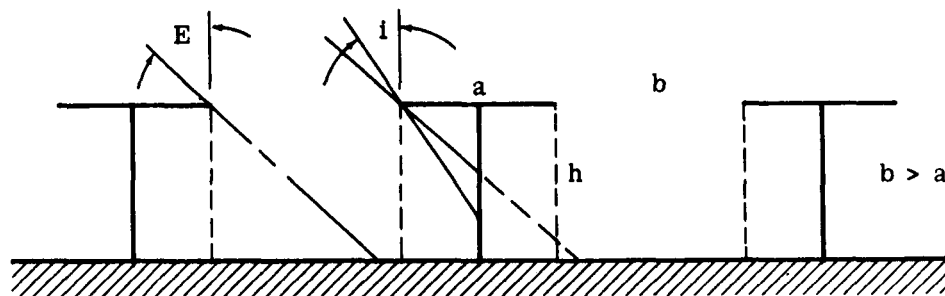
Boundary Condition on $i$ :	Brightness, $B$
$-E \leq i \leq -\tan^{-1}\left(\frac{\tan E}{2h + 1}\right)$	$K \left\{ \cos  i  \cos E(\rho_A a) + \rho_V \left[ \frac{1}{\tan E} \left( b + \frac{a}{2} \right) - \frac{a}{2} \tan\left(\frac{\pi}{2} -  i \right) \right] \cos\left(\frac{\pi}{2} - E\right) \cos\left(\frac{\pi}{2} -  i \right) \right\} c$
$\tan^{-1}\left(\frac{\tan E}{2h + 1}\right) \leq i \leq \tan^{-1}(\infty)$	$K \cos  i  \cos E(\rho_A a) c$

### T-MODEL



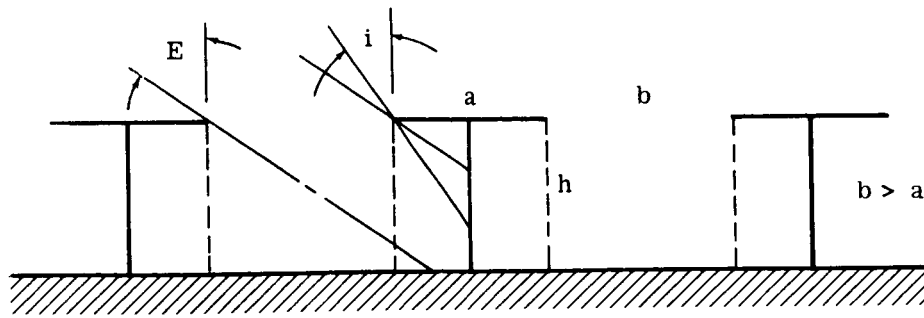
Case A:  $\tan^{-1}(0) \leq E \leq \tan^{-1}\left(\frac{a}{2h}\right)$

Boundary Condition on $i$ :	Brightness, $B$
$-E \leq i \leq \tan^{-1}\left(\frac{b-h \tan E}{h}\right)$	$K \cos  i  \cos E \left[ \rho_A a + \rho_B (b - h \tan E - h \tan i) \right] c$
$\tan^{-1}\left(\frac{b-h \tan E}{h}\right) \leq i \leq \tan^{-1}(0)$	$K \cos  i  \cos E (\rho_A a) c$



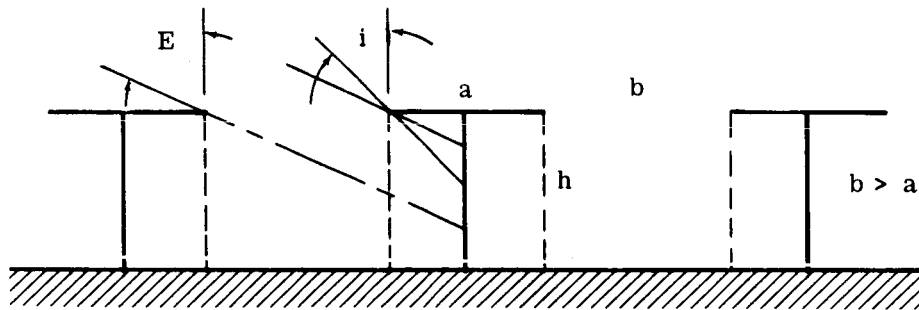
Case B:  $\tan^{-1}\left(\frac{a}{h}\right) \leq E \leq \tan^{-1}\left(\frac{b}{h}\right)$

Boundary Condition on $i$ :	Brightness, $B$
$-E \leq i \leq -\tan^{-1}\left(\frac{a}{2h}\right)$	$K \left\{ \cos  i  \cos E \left[ \rho_A a + \rho_B \left( \frac{a}{2} + b - h \tan E \right) \right] + \rho_V \cos\left(\frac{\pi}{2} -  i \right) \cos\left(\frac{\pi}{2} - E\right) \left[ h - \frac{a}{2} \frac{1}{\tan  i } \right] \right\} c$
$-\tan^{-1}\left(\frac{a}{2h}\right) \leq i \leq \tan^{-1}(0)$	$K \cos  i  \cos E \left[ \rho_A a + \rho_B (b - h \tan E + h \tan  i ) \right] c$
$\tan^{-1}(0) \leq i \leq \tan^{-1}\left(\frac{b-h \tan E}{h}\right)$	$K \cos  i  \cos E \left[ \rho_A a + \rho_B (b - h \tan E - h \tan i) \right] c$
$\tan^{-1}\left(\frac{b-h \tan E}{h}\right) \leq i \leq \tan^{-1}(0)$	$K \cos  i  \cos E (\rho_A a) c$



Case C:  $\text{Tan}^{-1}\left(\frac{b}{h}\right) \leq E \leq \text{Tan}^{-1}\left(\frac{b + \frac{a}{2}}{h}\right)$

Boundary Condition on $i$ :	Brightness, $B$
$-E \leq i \leq -\tan^{-1}\left(\frac{a}{2h}\right)$	$K \left\{ \cos  i  \cos E \left[ \rho_A a + \rho_B \left( \frac{a}{2} + b - h \tan E \right) \right] + \rho_V \cos\left(\frac{\pi}{2} -  i \right) \cos\left(\frac{\pi}{2} - E\right) \left[ h - \frac{a}{2} \frac{1}{\tan i } \right] \right\} c$
$-\tan^{-1}\left(\frac{a}{2h}\right) \leq i \leq -\tan^{-1}\left(\frac{h \tan E - b}{h}\right)$	$K \left\{ \cos  i  \cos E \left[ \rho_A a + \rho_B (h \tan  i  - h \tan E + b) \right] \right\} c$
$-\tan^{-1}\left(\frac{h \tan E - b}{h}\right) \leq i \leq \tan^{-1}(\infty)$	$K \cos  i  \cos E (\rho_A a) c$



Case D:  $\text{Tan}^{-1}\left(\frac{b + \frac{a}{2}}{h}\right) \leq E \leq \text{Tan}^{-1}(\infty)$

Boundary Condition on $i$ :	Brightness, $B$
$-E \leq i \leq -\tan^{-1}\left(\frac{\tan E}{2b + 1}\right)$	$K \left\{ \cos  i  \cos E \cdot (\rho_A a) + \rho_V \left[ \frac{1}{\tan E} \left( b + \frac{a}{2} \right) - \frac{a}{2} \tan\left(\frac{\pi}{2} -  i \right) \right] \cos\left(\frac{\pi}{2} - E\right) \cos\left(\frac{\pi}{2} -  i \right) \right\} c$
$-\tan^{-1}\left(\frac{\tan E}{2b + 1}\right) \leq i \leq \tan^{-1}(\infty)$	$K \cos  i  \cos E (\rho_A a) c$